DTIC FILE COPY

SECURITY CLASSIFICATION OF THIS PAGE (When Data Entered)

REPORT DOCUMENTATION PAGE

READ INSTRUCTIONS BEFORE COMPLETING FORM

1. REPORT NUMBER: AFIT/CI/NR 88-191

2. GOVT ACCESSION NO.

3. RECIPIENT'S CATALOG NUMBER

4. TITLE (and Subtitle): THE CHARACTERIZATION OF GaAs/AlGaAs HETEROSTRUCTURES BY VARIABLE ANGLE SPECTROSCOPIC ELLIPSOMETRY

5. TYPE OF REPORT & PERIOD COVERED: MS THESIS

6. PERFORMING ORG. REPORT NUMBER

7. AUTHOR(s): KENNETH G. MERKEL II

8. CONTRACT OR GRANT NUMBER(s)

9. PERFORMING ORGANIZATION NAME AND ADDRESS: AFIT STUDENT AT: UNIVERSITY OF NEBRASKA

10. PROGRAM ELEMENT, PROJECT, TASK AREA & WORK UNIT NUMBERS

11. CONTROLLING OFFICE NAME AND ADDRESS

12. REPORT DATE: 1988

13. NUMBER OF PAGES: 133

14. MONITORING AGENCY NAME & ADDRESS (if different from Controlling Office): AFIT/NR, Wright-Patterson AFB OH 45433-6583

15. SECURITY CLASS. (of this report): UNCLASSIFIED

15a. DECLASSIFICATION/DOWNGRADING SCHEDULE

16. DISTRIBUTION STATEMENT (of this Report): DISTRIBUTED UNLIMITED: APPROVED FOR PUBLIC RELEASE

DTIC ELECTE SEP 0 9 1988 S D E

17. DISTRIBUTION STATEMENT (of the abstract entered in Block 20, if different from Report): SAME AS REPORT

18. SUPPLEMENTARY NOTES: Approved for Public Release; IAW AFR 190-1
LYNN E. WOLAVER Lynn Wolaver 26 Aug 88
Dean for Research and Professional Development
Air Force Institute of Technology
Wright-Patterson AFB OH 45433-6583

19. KEY WORDS (Continue on reverse side if necessary and identify by block number)

20. ABSTRACT (Continue on reverse side if necessary and identify by block number): ATTACHED

88 9 6 206

AD-A198 776

DD FORM 1 JAN 73 1473 EDITION OF 1 NOV 65 IS OBSOLETE

UNCLASSIFIED

SECURITY CLASSIFICATION OF THIS PAGE (When Data Entered)

The Characterization of GaAs/AlGaAs Heterostructures by Variable Angle Spectroscopic Ellipsometry

Kenneth G. Merkel II, M.S.

University of Nebraska - Lincoln, 1988

Advisor: John A. Woollam

Variable angle of incidence spectroscopic ellipsometry (VASE) has been used as a means of determining layer thickness, alloy composition, and growth quality of GaAs/AlGaAs samples. The following separate studies were conducted: 1) wafer homogeneity determination, 2) superlattice characterization, and 3) interfacial roughness measurement. All samples were grown by molecular beam epitaxy (MBE) at other research facilities.

In the first study the layer thicknesses and alloy compositions of a sample were measured on a multilayered sample at three positions extending radially from the center of the sample. Thus a three-dimensional analysis of the sample was performed over a one inch area. The layer thicknesses of the AlGaAs, GaAs, and native oxide were found to vary by less than one percent. No evidence of an interfacial roughness layer was detected on top of the AlGaAs.

The second study involved GaAs/AlGaAs multilayered structures; each containing a superlattice "barrier". These samples were grown for later formation of modulation-doped field effect transistors (MODFETs). Sample modeling was performed by treating the superlattice as a bulk AlGaAs layer of unknown composition. Extremely good data fits were realized when five layer thicknesses and two alloy ratios were allowed to vary in a regression analysis. Room temperature excitonic effects associated with the e-hh(1), e-lh(1) and e-hh(2) transitions were observed in the VASE data.

In the third study an attempt was made to measure interfacial roughness at an inverted GaAs/AlGaAs interface. The study was found to be inconclusive for determining the existence of a roughness layer below a 50 A GaAs cap layer. It is unknown whether the inability to measure interfacial roughness of monolayer dimensions is a fundamental limitation of VASE or whether roughness is nonexistent.

DTIC COPY INSPECTED

Accession For
NTIS GRA&I ☒
DTIC TAB ☐
Unannounced ☐
Justification
By
Distribution/
Availability Codes
Dist | Avail and/or Special
A-1

The Characterization of GaAs/AlGaAs Heterostructures by Variable Angle Spectroscopic Ellipsometry

by

Kenneth G. Merkel II

A THESIS

Presented to the Faculty of
The Graduate College in the University of Nebraska
In Partial Fulfillment of the Requirements
For The Degree of Master of Science

Major: Electrical Engineering

Under the Supervision of Professor John A. Woollam

Lincoln, Nebraska

August, 1988

The Characterization of GaAs/AlGaAs Heterostructures by Variable Angle Spectroscopic Ellipsometry

Kenneth G. Merkel II, M.S.
University of Nebraska - Lincoln, 1988

Advisor: John A. Woollam

Variable angle of incidence spectroscopic ellipsometry (VASE) has been used as a means of determining layer thickness, alloy composition, and growth quality of GaAs/AlGaAs samples. The following separate studies were conducted: 1) wafer homogeneity determination, 2) superlattice characterization, and 3) interfacial roughness measurement. All samples were grown by molecular beam epitaxy (MBE) at other research facilities.

In the first study the layer thicknesses and alloy compositions of a sample were measured on a multilayered sample at three positions extending radially from the center of the sample. Thus a three-dimensional analysis of the sample was performed over a one inch area. The layer thicknesses of the AlGaAs, GaAs, and native oxide were found to vary by less than one percent. No evidence of an interfacial roughness layer was detected on top of the AlGaAs.

The second study involved GaAs/AlGaAs multilayered structures; each containing a superlattice "barrier". These samples were grown for later formation of modulation-doped field effect transistors (MODFETs). Sample modeling was performed by treating the superlattice as a bulk AlGaAs layer of unknown composition. Extremely good data fits were realized when five layer thicknesses and two alloy ratios were allowed to vary in a regression analysis. Room temperature excitonic effects associated with the e-hh(1), e-lh(1) and e-hh(2) transitions were observed in the VASE data.

In the third study an attempt was made to measure interfacial roughness at an inverted GaAs/AlGaAs interface. The study was found to be inconclusive for determining the existence of a roughness layer below a 50 A GaAs cap layer. It is unknown whether the inability to measure interfacial roughness of monolayer dimensions is a fundamental limitation of VASE or whether roughness is nonexistent.

Acknowledgements

When embarking on an endeavor such as this, one is filled with excitement and a little apprehension. I'd like to express my sincerest gratitude to those who have helped to erase the apprehension and sustain the excitement.

Dr. John A. Woollam has been a steadfast guide through this effort. He has instilled in me an efficient and independent research methodology. Also, he helped me gain practice in the professional responsibilities associated with being a member of the scientific community through publishing and presentation. Dr. Paul G. Snyder was an omnipresent mentor tirelessly answering my grab bag of questions and providing insight into my work. Dr. Samuel A. Alterovitz provided many of the resources for this project and shared his valuable time on visits to NASA Lewis Research Center. I especially admire Sam for his ability to resolve meaningful results from volumes of data. I'd like to extend my thanks to Dr. Frank G. Ullman and Dr. Mohammed Ismail for being on my advisory committee and for being professors of the highest caliber.

Many thanks to the following lab clan members (both past and present) who've been both fine comrades and teachers of their cultures: Dr. Jae E. Oh, Dr. Timir Datta, Dr. Stan Orzesko, Alan Massengale, Tom Tiwald, Kazem Memrazadeh, Tom Zillig, John Sullivan, Willie Notohamiprodjo, Bill McGahan, Bhola De, Duane Meyer, Ahmed

Akhter Ueddin, and Ted Barker. I feel each of you will be successful regardless of the path you take.

I thank Col John R. Vick of UNL Air Force ROTC DET 465 and Lt Col James H. Parsons of the Air Force Institute of Technology for the smooth and expedient assistance rendered on administrative matters pertaining to my assignment at the University of Nebraska.

To my father and mother, Kenneth and Kathleen: long haired bass players can become productive members of the community. Thanks.

Last, yet always first in mind, I thank my wife Deborah ("Bear") and my sons Kenny ("Lou"), Ryan ("Rippy the Quick"), and Teddy ("Growly"). I love you dearly.

Table of Contents

Page

Abstract .....

Acknowledgements i

Introduction 1

Chapter 1. Variable Angle Spectroscopic Ellipsometry 3

A. The Theory of Ellipsometric Measurement 4

B. The VASE Measurement System 14

C. The VASE Data Modeling Procedure 18

Chapter 2. The Physics and Technology of GaAs/AlGaAs Heterostructures 30

A. MODFET Technology 31

B. Molecular Beam Epitaxy Growth of Quantum Wells and Superlattices 41

C. Excitons in Quantum Wells and Superlattices ... 50

D. Quantum Well Opto-electronics 58

E. Direct Interband Transitions in Semiconductors 68

F. MODFET and Multiple Quantum Well Energy Bands 80

Chapter 3. VASE Studies of GaAs/AlGaAs Heterostructures 94

A. Preliminary Comments 95

B. Wafer Homogeneity Study 101

C. Characterization of GaAs/AlGaAs Superlattices .113

D. Interfacial Roughness Study 130

To our Lord, Jesus Christ

For the moment all discipline seems painful rather than pleasant; later it yields the peaceful fruit of righteousness to those who have been trained by it.

Hebrews 12:11

I. Introduction

Rapid progress has occurred in the development of GaAs/AlGaAs modulation-doped and multiple quantum well heterostructure devices. These types of structures have found applications in opto-electronics, digital electronics and microwave analog communications (1).

These advances have created a requirement for monitoring the accuracy and quality of III-V semiconductor growth processes. Variable angle of incidence spectroscopic ellipsometry (VASE) provides an accurate and nondestructive method of characterizing both simple and complex multilayered semiconductor structures (2). Particularly, VASE is applicable as a diagnostic tool for studying: the layer thicknesses and alloy compositions (3), wafer homogeneity (4), surface oxide growth (5), interfacial roughness (6), and electric fields (7) in heterostructures and superlattices.

Chapter 1 contains an overview of the VASE process including the theory, measuring system, and data analysis. Chapter 2 provides a background discussion of the physics and technology of GaAs/AlGaAs heterostructures in areas pertinent to this research effort. Chapter 3 encompasses the results of VASE studies performed on GaAs/AlGaAs samples.

A note to the readers: each section of this thesis is a self contained unit. References are provided at the end

of each of these sections. Figures, tables, equations and their variables, unless explicitly mentioned, pertain only to the section in which they are mentioned.

References

1) T.J. Drummond, W.T. Masselink and H. Morkoc, Proc. of the IEEE **74**, 773, (1986).

2) K.G. Merkel, P.G. Snyder, J.A. Woollam and S.A. Alterovitz, to be published in J. Appl. Phys., (1987).

3) P.G. Snyder, M.C. Rost, G.H. Bu-Abbud, J.A. Woollam and S.A. Alterovitz, J. Appl. Phys. **60**, 3293, (1986).

4) S.A. Alterovitz, P.G. Snyder, K.G. Merkel, J.A. Woollam, D.C. Radulescu and L.F. Eastman, to be published in J. Appl. Phys., (1987).

5) H. Burkhard, H.W. Dinges and E. Kuphal, J. Appl. Phys. **53**, 655, (1982).

6) M. Erman, J.B. Theeten, N. Vodjdani and Y. Demay, J. Vac. Sci. Tech. **B1**, 328, (1983).

7) P.G. Snyder, J.E. Oh, J.A. Woollam and R.E. Owens, Appl. Phys. Lett. **51**, 770, (1987).

Chapter 1.

Variable Angle Spectroscopic Ellipsometry

A. The Theory of Ellipsometric Measurement

The theoretical analysis of an ellipsometer system containing a polarizer, sample, and analyzer (PSA system) is fairly simple in concept. The VASE apparatus can be represented in a manner analogous to any physical system. A "transfer function" for the VASE is derivable in terms of the effect of each optical component on the input electric field. An elegant and utilitarian approach to any ellipsometric configuration is available through the Jones vector and Jones matrix formalism (1)

A representation of the amplitude and orientation of an electric field is provided by the Jones vector. The initial step in the Jones approach is to place the scalar components of the electric field in a vector. These scalar components can be expressed in terms cartesian coordinates by

$$\bar{E}(z,t) = \begin{bmatrix} \bar{E}_x \\ \bar{E}_y \end{bmatrix} = \begin{bmatrix} E_x \cos(\omega t - kz + \delta_x) \\ E_y \cos(\omega t - kz + \delta_y) \end{bmatrix} \quad (1)$$

This is an electric field propagating in the +z direction with component amplitudes E_x and E_y, angular frequency ω, wavevector k, and phases δ_x and δ_y. The temporal aspects of the wave can be suppressed since the field components for a monochromatic wave are known to oscillate in time at the same frequency.

$$\bar{E}(z) = e^{-kz} \begin{bmatrix} E_x e^{\delta_x} \\ E_y e^{\delta_y} \end{bmatrix} \quad (2)$$

By considering the field with respect to a single plane perpendicular to the direction of travel (i.e. a plane situated at z = 0), the spatial dependence may also be dropped

$$\bar{E} = \begin{bmatrix} E_x e^{\delta_x} \\ E_y e^{\delta_y} \end{bmatrix} \tag{3}$$

This is the Jones vector representation of the electric field.

The Jones matrix describes the overall effect of an optical system (or the system's components) on an incident wave. A schematic diagram of an optical system with a plane wave input for cartesian coordinates is shown in Fig. 1. The input wave E_i has the right handed coordinates x,y and z. The output wave has E_o coordinates x′, y′ and z′. The directions of travel are z and z′ for the incoming and outgoing wave respectively. S signifies the optical system (i.e. the sample in the PSA system). In the absence of nonlinearities and frequency altering effects, the output wave components in the (x′, y′, z′) reference frame can be designated in terms of the input wave components in the (x,y,z) frame in the following manner:

$$\begin{aligned} E_{ox}' &= T_{11} E_{ix} + T_{12} E_{iy} \\ E_{oy}' &= T_{21} E_{ix} + T_{22} E_{iy} \end{aligned} \tag{4}$$

These two equations are easily put into matrix form

$$\begin{bmatrix} E_{ox}' \\ E_{oy}' \end{bmatrix} = \begin{bmatrix} T_{11} & T_{12} \\ T_{12} & T_{22} \end{bmatrix} \begin{bmatrix} E_{ix} \\ E_{iy} \end{bmatrix} \tag{5}$$

Note that equation (5) gives the Jones vector for the out-

put wave with respect to the Jones vector of the input wave. The transition matrix between the input and output Jones vectors is the Jones matrix. Each of the T_{ij} matrix components are in general complex. Since the wavefronts can be viewed from reference points at the immediate input and output of the system, $z = 0$ and $z' = 0$. The Jones matrix thus presents information about the effect of a particular optical system on the azimuthal orientation relationship between the input and output reference axes. Any phase modification of the electric field components caused by the system are contained in the Jones matrix.

Another matrix of primary importance in optical systems is the rotation matrix. This matrix allows a coordinate rotation of the Jones vector's reference axes. Figure 2. presents the graphical aspects of this rotation. Shown here is the rotation of an electric field vector with reference axes x,y into axes labelled x',y'. The angle of rotation is γ. Using the Jones vector it is apparent that the rotation can be described in the following manner:

$$\begin{bmatrix} E_{x'} \\ E_{y'} \end{bmatrix} = \begin{bmatrix} \cos\gamma & \sin\gamma \\ -\sin\gamma & \cos\gamma \end{bmatrix} \begin{bmatrix} E_x \\ E_y \end{bmatrix} \qquad (6)$$

where the matrix performing the rotation operation on the Jones vector is the rotation matrix. A counter-rotation from x',y' to x,y is also available by merely changing the sign of γ.

Armed with the Jones formalism, the theory concerning

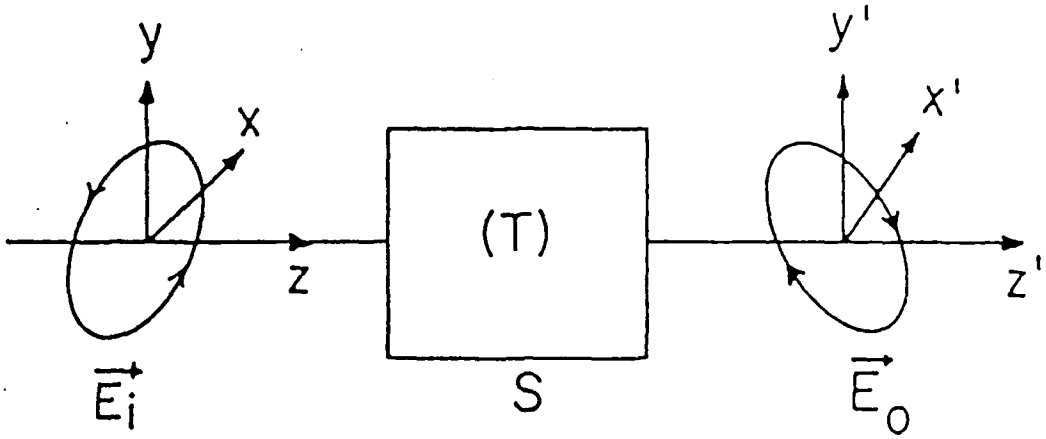

Figure 1. Schematic of an optical system showing the Jones vector reference axes (from Ref. 1).

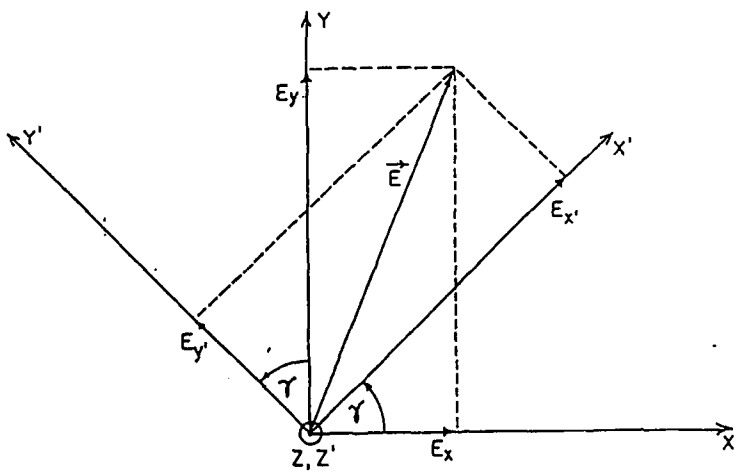

Figure 2. Diagram of coordinate transformation from axes x, y to x′,y′ (from Ref. 1).

the measurement of the polarization ellipse is straightforward (2). The PSA system and its reference axes are illustrated in Fig. 3. The x and y axes are taken as respectively the horizontal and vertical axes viewed with the beam traveling toward the observer. The electric field at the PMT input, E_D, can be expressed as the product of the following matrices operating on the electric field exiting the polarizer, E_{PO},

$$\bar{E}_D = \bar{T}_A \bar{R}(A) \bar{S} \bar{R}(-P) \bar{E}_{PO} \qquad (7)$$

The R() matrices represent the coordinate rotations referenced to the polarizer (P) and analyzer (A) angles.

The polarizer allows passage of light linearly polarized in the x′ direction. Therefore the effect of the polarizer section is given by the following counter-rotation:

$$\bar{R}(-P) \bar{E}_{PO} = \begin{bmatrix} \cos P & -\sin P \\ \sin P & \cos P \end{bmatrix} \begin{bmatrix} 1 \\ 0 \end{bmatrix} \qquad (8)$$

The sample is described by a Jones matrix having the complex reflection coefficients r_p and r_s as matrix elements. These reflection coefficients contain the ratio of the reflected to incident electric field and are given by

$$r_p = \frac{E_{pr}}{E_{pi}} = \frac{E_{xr}}{E_{xi}} \qquad (9a) \quad \text{and} \quad r_s = \frac{E_{sr}}{E_{si}} = \frac{E_{yr}}{E_{yi}} \qquad (9b)$$

Here the subscripts p and s (from the German "senkrecht") refer to the field components oriented parallel and perpendicular to the plane of incidence of the sample. The

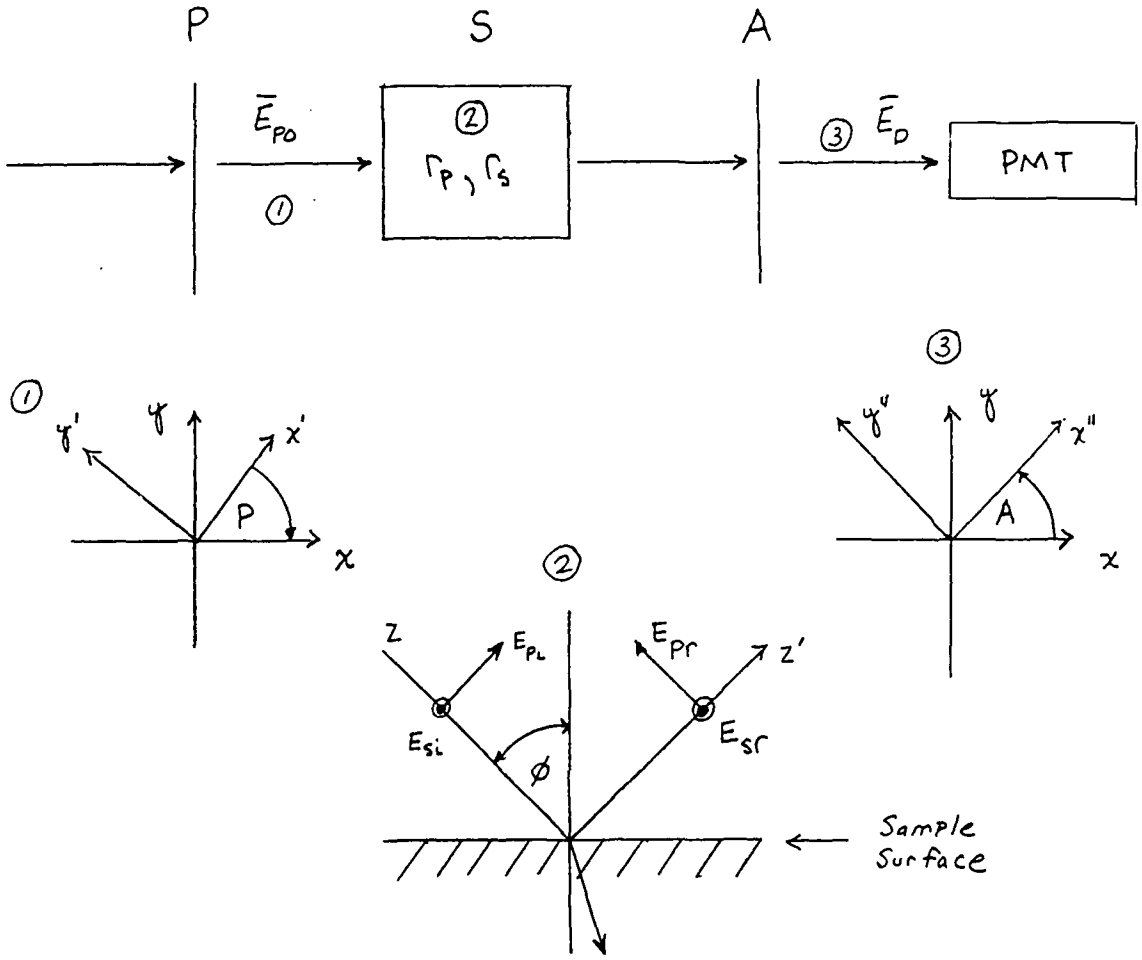

Figure 3. The PSA system showing the reference axes for each optical component.

subscripts r and i stand for reflected and incident. The sample alignment procedure prior to measurement orients the plane of incidence so that the p and s axes coincide with the x and y reference axes. The transfer matrix of the sample is thus given by

$$\bar{S} = \begin{bmatrix} r_p & 0 \\ 0 & r_s \end{bmatrix} \tag{10}$$

The analyzer will permit the transmission of the reflected electric field components oriented only in the x'' direction. Thus a rotation from the x,y to x'' axes is needed:

$$\bar{T}_A \bar{R}(A) = \begin{bmatrix} 1 & 0 \\ 0 & 0 \end{bmatrix} \begin{bmatrix} \cos A & \sin A \\ -\sin A & \cos A \end{bmatrix} \tag{11}$$

The PSA system transfer function is obtained by combining equations 8, 10 and 11:

$$\bar{E}_D = \begin{bmatrix} 1 & 0 \\ 0 & 0 \end{bmatrix} \begin{bmatrix} \cos A & \sin A \\ -\sin A & \cos A \end{bmatrix} \begin{bmatrix} r_p & 0 \\ 0 & r_s \end{bmatrix} \begin{bmatrix} \cos P & -\sin P \\ \sin P & \cos P \end{bmatrix} \begin{bmatrix} 1 \\ 0 \end{bmatrix}$$

$$= \begin{bmatrix} r_p \cos P \cos A + r_s \sin P \sin A \\ 0 \end{bmatrix} \tag{12}$$

The intensity at the PMT input is represented by the following proportionality:

$$I_D \propto |\bar{E}_D| |\bar{E}_D^*| \tag{13}$$

A proportionality is used since the characteristic impedance is omitted. The expression for intensity is taken out of matrix form at this point since the value I_D seen at the PMT input depends only upon the x'' orientation of the

rotating analyzer fast axis. The intensity at the detector is easily determined by inserting E_D and E_D^* from equation 12 into equation 13 and performing the mathematical operations:

$$I_D \propto \left[r_p \cos P \cos A + r_s \sin P \sin A\right] \cdot \left[r_p^* \cos P \cos A + r_s^* \sin P \sin A\right]$$

$$= |r_p|^2 \cos^2 P \cos^2 A + |r_s|^2 \sin^2 P \sin^2 A + (r_p r_s^* + r_p^* r_s) \sin P \cos P \sin A \cos A$$

$$= |r_p|^2 \cos^2 P (1 + \cos 2A) + |r_s|^2 \sin^2 P (1 - \cos 2A) + 2\,\mathrm{Re}\,(r_p r_s^*) \sin P \cos P \sin 2A$$

$$= |r_p|^2 \cos^2 P + |r_s|^2 \sin^2 P + \left[|r_p|^2 \cos^2 P - |r_s|^2 \sin^2 P\right] \cos 2A + 2\,\mathrm{Re}\,(r_p r_s^*) \sin P \cos P \sin 2A$$

I_D can be normalized so that its has an average value of 1, thus yielding

$$I_D \propto 1 + \frac{|r_p/r_s|^2 - \tan^2 P}{|r_p/r_s|^2 + \tan^2 P} \cos 2A + \frac{2\,\mathrm{Re}\,(r_p/r_s) \tan P}{|r_p/r_s|^2 + \tan^2 P} \sin 2A \qquad (14)$$

This expression can be further simplified using the relationship between the ellipsometric parameters ψ and Δ and the complex reflection coefficients of equation 9a and 9b:

$$\frac{r_p}{r_s} = \mathrm{Tan}\,\psi\, e^{i\Delta} \tag{15}$$

I_D then becomes

$$I_D \propto 1 + \frac{\mathrm{Tan}^2\psi - \mathrm{Tan}^2 P}{\mathrm{Tan}^2\psi + \mathrm{Tan}^2 P}\,\mathrm{Cos}\,2A + \frac{2\,\mathrm{Tan}\,\psi\,\mathrm{Cos}\,\Delta\,\mathrm{Tan}\,P}{\mathrm{Tan}^2\psi + \mathrm{Tan}^2 P}\,\mathrm{Sin}\,2A \tag{16}$$

which is reducible to

$$I_D \propto 1 + \alpha\,\mathrm{Cos}\,2A + \beta\,\mathrm{Sin}\,2A \tag{17}$$

I_D (which is normalized in this case) is a sum of sinusoidal terms riding on a DC level. This intensity is the quantity measured as explained in the section on the PSA system. The coefficients α and β are the normalized Fourier coefficients of the intensity. The values of α and β are determined after data acquisition by a Fourier analysis of I_D contained in a computer program.

To summarize, VASE measurement thory is based on the following process:

1) Measure the light intensity coming from the sample.
2) Determine the Fourier coefficients α and β.
3) Invert the Fourier coefficients to find Tanψ and CosΔ (ψ and Δ).
4) Determine the reflection coefficients r_p and r_s from ψ and Δ.
5) The dielectric properties , optical constants, alloy composition, and layer thicknesses are calculated using the reflection coefficients and the angle of incidence.

References

1) R.M.A. Azzam and N.M. Bashara, Ellipsometry and Polarized Light, North-Holland Publishing, (1987).

2) P.G. Snyder, unpublished material presented at the workshop: "Fundamentals and Applications of Ellipsometry", University of Nebraska-Lincoln, 15-19 June, (1987).

B. Description of VASE System

Shown in Fig. 1 is a schematic diagram of the rotating analyzer VASE used for the experimental phase of this research effort. The system is based upon a design by Aspnes and Studna (1). However, the system at the University of Nebraska has been modified to include variable angle of incidence capability. The system is basically composed of the following sections: light beam generation, ellipsometer, and data acquisition electronics.

The beam generation section contains the lamp, monochromator, and collimator optics. The lamp is a 75 W Xenon short arc type with a spectral emission in the 2,000 to 20,000 A range. The arc lamp output is passed to a Kratos GM252 monochromator which provides a narrow band of wavelengths from 2500 to 8500 A with a line width of approximately 20 A. The beam divergence at the monochromator output is controlled by an off-axis parabolic reflector and the input collimator on the polarizer.

The ellipsometer is a Gaertner model L119 with the capability of varying the angle of incidence, ϕ, from 20° to almost 90° with an accuracy of $+/- 0.01^\circ$. The monochromator beam enters the polarizer and exits at a known, linear polarization. The beam strikes the sample becoming elliptically polarized and is reflected to the rotating analyzer. The rotating analyzer sweeps the ellip-

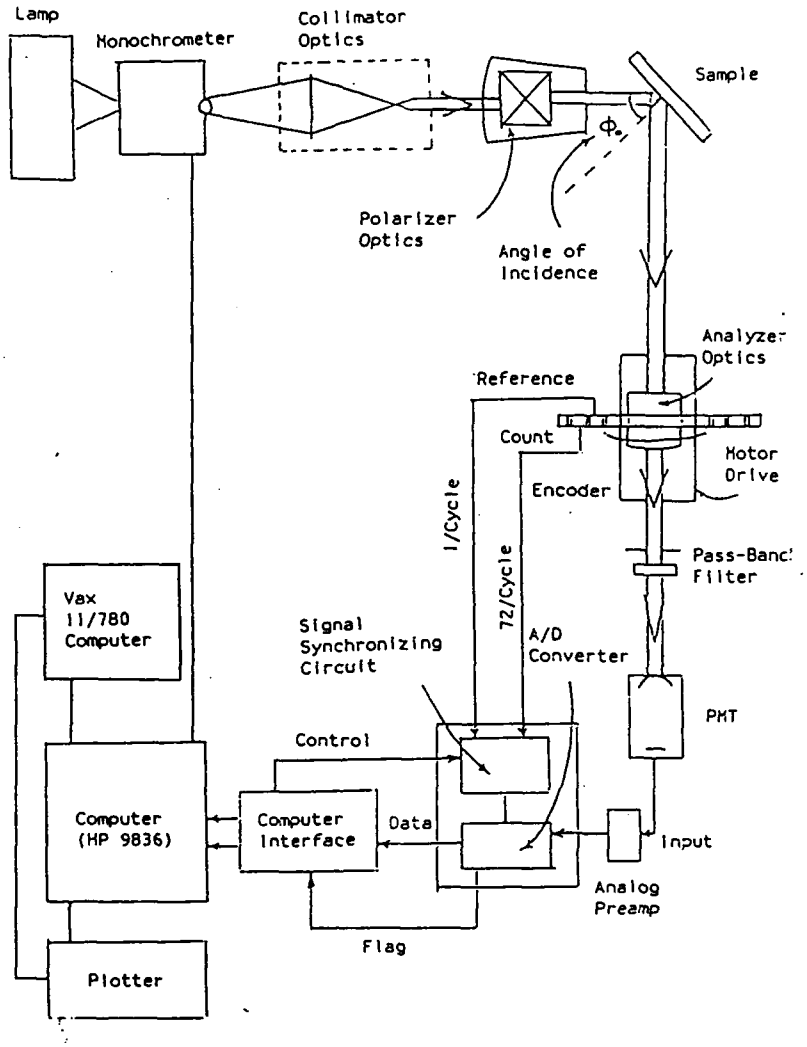

Figure 1. Schematic diagram of the rotating analyzer VASE system.

tical beam at 3600 rpm. Thus a signal which is amplitude modulated by an amount determined by the eccentricity of the polarization ellipse is passed to the photomultiplier tube (PMT).

The data acquisition section converts the analog PMT signal voltage to a digital response which is passed to a computer for analysis. The output of the PMT is a sinusoidal voltage impressed on a DC level. This PMT output is amplified and sent to the A/D converter. The maximum and minimum excursions of the sinusoid above DC represent respectively the long and short axis of the polarization ellipse. A reference pulse is initiated at a calibrated setting of the analyzer. The first count pulse is initiated simultaneously with the reference pulse. The signal is then sampled 72 times per revolution of the analyzer. The sampling period is variable between 24 and 300 cycles per reading. Longer sampling periods allow increased averaging of the A/D converter output. This averaging suppresses noise effects in spectral regions where the signal to noise ratio is low. The sampled and averaged signal is sent in digital form to the computer where a complex analysis yields the ellipsometric parameters, dielectric (optical) constants as a function of wavelength.

References

1) D.E. Aspnes and A.A. Studna, Appl. Optics **14**, 220, (1975).

C. The VASE Modeling Procedure

The experimental data taken from VASE measurements is modeled using the Multiple Angle and Wavelength for Effective Media Approximation (MAWEMA) program written by Martin C. Rost at the University of Nebraska. The overall purpose of the program is to fit calculated values of ψ and Δ to the experimental values of the two ellipsometric parameters as a function of wavelength. MAWEMA is also capable of generating ψ and Δ values given a layered structure with fixed layer thicknesses and compositions.

The data fitting is done by first specifying the appropriate variable(s) (i.e. layer thickness, alloy composition, etc.) in the model file. Using initial estimates of those variables, ψ and Δ values are generated using the Fresnel reflection coefficients for a multilayered structure. The calculated ψ and Δ values are then compared with the experimental ψ and Δ values and the mean square error (MSE) between the calculated and experimental values is determined. The standard MSE is given by

$$MSE = \frac{1}{m} \sum_{i=1}^{m} \left[(\psi_{ci} - \psi_{ei})^2 + (\Delta_{ci} - \Delta_{ei})^2 \right]^{1/2} \quad (1)$$

where the subscripts c and i stand for calculated and experimental respectively, and i is an index that ranges over all the m measured values of ψ and Δ. The MSE may also be determined with respect to: 1) ψ only, 2) Δ only, 3) Tanψ and CosΔ, 4) Tanψ only, and 5) Cos Δ only. After MSE determination, the constituent variables are per-

turbed and the process is repeated. Each perturbation is directed toward producing the smallest MSE possible between the calculated and experimental values of the ellipsometric parameters.

Physically, the computations are carried out using three files: 1) the data input file, labeled FILE.INN, 2) the model file, labeled FILE.MOD, and 3) the data output file, labeled FILE.OUT. An example of a portion of an INN file obtained from a GaAs/AlGaAs structure is shown in Fig 1. This file is produced from measured data that is transferred via modem from the VASE laboratory to the VAX computer system. The input file is designated as either EXPERIMENTAL or GENERATED on the first line. Only the results of an experimental input file will be considered here. Some generated results are provided in the VASE studies section of this thesis (M.C. Rost's manual provides a number of excellent examples). The first column contains the wavelengths of the measured spectrum (measured at 40 A intervals in this case). The second column contains the angle of incidence with the third and fourth columns manifesting ψ and Δ respectively. The MAWEMA program can analyze input data sets with single or multiple angles of incidence.

The MOD files are set up with the format shown in Fig. 2a. An example model file for a GaAs/AlGaAs multilayered sample is illustrated in Fig. 2b.

The statistical theory behind the MAWEMA program is too involved and voluminous to describe here. Therefore, the explanation of the MOD structure file will be detailed only with respect to those modeling quantities that are alluded to in the latter portions of this thesis. The explanation for the designations in the MOD file format of Fig. 2a. is as follows:

1. <u>EMA Type</u> If a 0 is placed in this position the effective medium approximation that is used is Maxwell-Garnett; a 1 signifies Bruggeman EMA. The Maxwell-Garnett and Bruggeman EMA methods are used to characterize the microstructure of film layers that may consist of different constituents (i.e a roughness layer that is a mixture of 50% GaAs and 50% AlGaAs). The Maxwell- Garnett method solves for dielectric properties by modeling a layer as a host material containing isolated "islands" of other dielectric materials. The Bruggeman method assumes a random mixture of a number of dielectric materials. The Bruggeman microstructure is thus a series of interconnected sections of differing dielectric materials. Neither of these EMAs is typically used in the solution of the layer thicknesses and alloy composition of MBE grown samples since the layer interfaces are assumed abrupt and the materials in the layers are well known. In the example of Fig 2b. a Bruggeman EMA is designated but is not required in the model.

```
EXPERIMENTAL
3000.    73.500    17.9962    107.9154
3040.    73.500    17.8743    106.9008
3080.    73.500    17.8225    106.0918
3120.    73.500    17.8169    105.5311
3160.    73.500    17.8221    105.1301
3200.    73.500    17.8405    104.9931
3240.    73.500    17.8966    104.9825
3280.    73.500    17.9652    105.0927
3320.    73.500    18.0430    105.3621
3360.    73.500    18.1314    105.7877
3400.    73.500    18.2306    106.2427
3440.    73.500    18.3461    106.9843
                   *
                   *
                   *
                   *
```

Figure 1. Example of an INN file used in MAWEMA.

```
(EMA TYPE)  (MSE TYPE)  (ISEN)  (ICOV)  (IPNT)  (ITMAX)
(MSEVAR)  (EPS1)  (EPS2)
(FILM NUMBER)  (DATA FILE NAME)
(FRACTION) (IFRAC) (THICKNESS)  (ITHICK) (IDEP) (IOSC)
n k  n k  n k  n k  n k  n k  n k  n k  n k  n k
n k  n k  n k  n k  n k  n k  n k  n k  n k  n k
(FRACTION) (IFRAC) (THICKNESS)  (ITHICK) (IDEP) (IOSC)
n k  n k  n k  n k  n k  n k  n k  n k  n k  n k
n k  n k  n k  n k  n k  n k  n k  n k  n k  n k
(FRACTION) (IFRAC) (THICKNESS)  (ITHICK) (IDEP) (IOSC)
n k  n k  n k  n k  n k  n k  n k  n k  n k  n k
n k  n k  n k  n k  n k  n k  n k  n k  n k  n k
                         *
                         *
                         *
```

Figure 2a. The format of a MOD file used in MAWEMA.

```
   1  0  2  1 20  99
   1.  1E-4  1E-4
1 GAAS.DAT
  1.  1                        1   0
  1 1  1 1  1 1  1 1  1 1  1 1  1 1  1 1  1 1  1 1  1 1
  1 1  1 1  1 1  1 1  1 1  1 1  1 1  1 1  1 1  1 1  1 1
1 ALGAAS5.DAT
  0.7  1       800.  0         2   0
  1 1  1 1  1 1  1 1  1 1  1 1  1 1  1 1  1 1  1 1  1 1
  1 1  1 1  1 1  1 1  1 1  1 1  1 1  1 1  1 1  1 1  1 1
1 ALGAAS4.DAT
  0. 1                         3   0
  1 1  1 1  1 1  1 1  1 1  1 1  1 1  1 1  1 1  1 1  1 1
  1 1  1 1  1 1  1 1  1 1  1 1  1 1  1 1  1 1  1 1  1 1
1 ALGAA3.DAT
  0. 1                         4   0
  1 1  1 1  1 1  1 1  1 1  1 1  1 1  1 1  1 1  1 1  1 1
  1 1  1 1  1 1  1 1  1 1  1 1  1 1  1 1  1 1  1 1  1 1
1 ALGAAS2.DAT
  0. 1                         5   0
  1 1  1 1  1 1  1 1  1 1  1 1  1 1  1 1  1 1  1 1  1 1
  1 1  1 1  1 1  1 1  1 1  1 1  1 1  1 1  1 1  1 1  1 1
1 ALGAAS1.DAT
  0. 1                         6   0
  1 1  1 1  1 1  1 1  1 1  1 1  1 1  1 1  1 1  1 1  1 1
  1 1  1 1  1 1  1 1  1 1  1 1  1 1  1 1  1 1  1 1  1 1
1 GAAS.DAT
  0. 1                         1   0
2 GAAS.DAT
  1. 1         500. 0          1   0
3 GAASOX.DAT
  1. 1         20.  0          7   0
  1 1  1 1  1 1  1 1  1 1  1 1  1 1  1 1  1 1  1 1  1 1
  1 1  1 1  1 1  1 1  1 1  1 1  1 1  1 1  1 1  1 1  1 1
```

Figure 2b. An example of the MOD file for a GaAs/AlGaAs structure.

2. MSE TYPE This entry is an integer between 0 and 5 which determines which ellipsometric parameter(s) will be minimized in the analysis as explained previously. In the example the MSE is being calculated with respect to both ψ and Δ.

3. ISEN is an integer entry between 0 and 3 that specifies whether to print the sensitivities matrix and/or the 90% confidence limits for each variable. The 90% confidence limits are based on Gaussian statistics and yield a measure of the uncertainty of the calculated data with respect to the experimental data. Since a variable value is calculated for each ψ-Δ pair taken at a single wavelength, the measured semiconductor system is overdetermined. The final calculated values of layer thickness and composition are the average values of the variable obtained from each wavelength. The 90% confidence limits are the variable values at the boundaries of 90% of the area underneath a Gaussian bell curve centered at the average value of that variable. In the example, only the 90% confidence limits will be placed in the output file.

4. ICOV is an integer entry (0 for "no", and 1 for "yes") specifying whether or not to print the covariance matrix. From the covariance matrix the correlation matrix is created. Correlation is the degree to which two variables are interdependent. An accurate determination of correlation is difficult since two variables may have a low correla-

tion but both may be highly correlated to a third variable. High correlation exists when one variable is changed in the model and the calculated values for that variable and another variable change considerably. Therefore cahnges in the ellipsometric data cannot be directly attributable to one variable only.

5. IPNT is an integer specifying the number of passes through the minimization routine for which the intermediate results are to be printed. If the MOD file of Fig. 2b. is used the results of every 20th iteration will be passed to the output file.

6. ITMAX is an integer which shows the number of iterations the minimization routine will perform before terminating if a solution hasn't been found. This prevents MAWEMA from trying to minimize the MSE indefinitely. Therefore, 99 or less iterations will be performed in the example.

7. MSEVAR is a real value which indicates by what percent a variable is to be changed in order to determine the change in MSE from one iteration to the next. The variables in the example are changed by 1% after each iteration.

8. EPS1 is a real number which specifies at what relative value of MSE from one iteration to the next the program will terminate. MAWEMA stops when the difference in MSE between subsequent iterations is less than this value. The

minimization will stop in the example when the MSE changes by less than 10^{-4}.

9. EPS2 is a real number stating the amount by which a variable may change from one iteration to the next before the model fitting process is ceased. A change in a model variable of less than 10^{-4} in the example will cause MAWEMA to terminate.

10. FILM NUMBER is an integer value which labels the film layers. The lowest numbered film, 0, is the bottom layer in the sample. In the example there are four films. The bottom film is a GaAs substrate followed by an AlGaAs layer, a GaAs layer, and a surface layer of GaAs native oxide.

11. DATA FILE NAME calls a computer data file which contains either the components of the complex permittivity (ϵ_1, ϵ_2) or the optical constants (n, k) over the wavelength range of interest for that particular layer. MAWEMA uses the optical constants in calculating the Fresnel reflection coefficients. In the example, the optical constants for the following materials are being used: GaAs (GAAS.DAT), $Al_{0.5}Ga_{0.5}As$ (ALGAAS5.DAT), $Al_{0.4}Ga_{0.6}As$ (ALGAAS4.DAT), $Al_{0.3}Ga_{0.7}As$ (ALGAAS3.DAT), $Al_{0.2}Ga_{0.8}As$ (ALGAAS2.DAT), $Al_{0.1}Ga_{0.9}As$ (ALGAAS1.DAT). The optical constants in the .DAT files have been obtained from published data (1,2,3) (some measured using ellipsometry). The AlGaAs materials with different composition assigned

to layer 1 are used in a subroutine that provides interpolated values of n and k taken from the .DAT files. This allows the composition value to be varied between x = 0 and x = 1.

12. FRACTION states what decimal percentage of that layer is the constituent in the data file. This percentage is used in the Maxwell-Garnett and Bruggeman EMAs. The 0.3 in the example means that layer 1 is AlGaAs with x = 0.3.

13. IFRAC is an integer stating whether the FRACTION is variable (0), fixed (1), or dependent upon the variable value (2). The AlGaAs composition in layer 1 is then variable.

14. THICKNESS (real variable) is the thickness of a particular layer in angstroms. In the GaAs/AlGaAs .MOD file shown, the bottom layer is GaAs substrate with a thickness that is optically infinite, therefore no layer thickness is provided. The AlGaAs layer is 800 A thick, the GaAs layer 500 A and the oxide layer is 20 A.

15. ITHICK is an integer indicating whether the layer thickness is variable (0) or fixed (1). All layer thicknesses in the example are variable except the substrate.

16. IDEP is the inter-film dependence integer. Each constituent is assigned a dependence number indicating whether the film has the same material in it as another film. The interdependent films in the example .MOD file are the GaAs films, meaning that the same optical con-

stants are used for each of the GaAs layers.

17. IOSC is an integer designating whether the optical constants from a .DAT file or an oscillator data file is to be used. An oscillator data file is used if the optical constants are expressable as Lorentzian oscillators. Each oscillator has a resonant frequency (wavelength). Oscillators can be used if peaks are observed in the experimental, optical constant data. Single or multiple oscillators can then be used to fit the data by placing an oscillator at the wavelength of the peak(s). No oscillators are used in the example.

18. n k These are the number of n-k data sets to be solved for using MAWEMA. The integer 0 means that they are variable and that n and k are to be determined using the experimental data. The integer 1 is used for fixed values. The number of n-k sets must correspond to the number of ψ and Δ experimental data sets. In this case the sample was measured at 20 different wavelengths and the fixed optical constants at each of those wavelengths must be called up from the .DAT files. Notice that the n-k sets do not need to be repeated for films that are interdependent since the optical constants for that film have already been used.

It should be stressed that the statistical parameters determined by the MAWEMA program (i.e., MSE, 90% confidence limits, and correlation) are not singularly indicative of the correctness of the data fitting procedure.

This is due to the fact that the results are dependent upon the initial model used. When modeling MBE grown GaAs samples, the values of layer thickness and composition provided by the growers are considered to be at least "ballpark" figures. The statistical values are implemented mainly for the comparison of different minimization runs. A good modeling procedure is to use different starting values of layer thickness and composition and compare the results of each analysis. If the layer thicknesses and compositions are the same, then an accurate analysis is assured.

The output file (.OUT) contains the following:

1) The experimental and calculated values of ψ and Δ at the wavelengths measured.

2) The experimental and calculated dielectric constants of each layer. The dielectric constants are related to the ellipsometric parameters by

$$\epsilon = \epsilon_1 + i\epsilon_2 = \sin^2\phi \left[1 + \left(\frac{1 - \tan\psi e^{i\Delta}}{1 + \tan\psi e^{i\Delta}} \right) \tan^2\phi \right] \tag{2}$$

The dielectric constants can be expressed in terms of the optical constants by

$$\epsilon_1 = n^2 - k^2 \qquad \epsilon_2 = 2nk \tag{3}$$

The index of refraction of an absorbing material is a com-

plex quantity given by

$$N = n + ik \tag{4}$$

This value, N, is used in the Fresnel coefficients and provides the phase difference between the reflection coefficients and hence elliptical polarization of the reflected beam.

3) Minimization statistics, i.e., the MSE, 90% confidence limits and the correlation matrix.

REFERENCES

1) M. Erman, J.P. Andre, and J. LeBris, J. Appl. Phys. **59**, 2019, (1986)

2) H. Burkhard, H.W. Dinges, and E. Kuphal, J. Appl. Phys **53**, 655, (1983).

3) D.E. Aspnes, S.M. Kelso, R.A. Logan, and R.H. Bhat, J. Appl. Phys. **60**, 754, (1986).

Chapter 2.

The Physics and Technology of GaAs/AlGaAs Heterostructures

A. MODFET Technology

The advent of the layered semiconductor superlattice, first proposed by Esaki and Tsu in the late 1960s, led to the development of the first modulation-doped field effect transistor (MODFET) by Dingle, Stormer and Gossard at Bell Laboratories in 1978. Since then, improvements in device speed, power consumption and operating frequencies have occurred through the further development of MODFET technology.

MODFETs are formed by growing alternate layers of doped AlGaAs on undoped GaAs (hence the term "modulation-doped"). An energy band diagram for the MODFET is shown in Fig. 1. Since the GaAs has a smaller band gap energy than the $Al_xGa_{1-x}As$, a band discontinuity (dependent on the AlGaAs mole fraction x) exists at their juncture and quantized electron and hole levels occur in the GaAs layer. The donor doping level in the AlGaAs is at a higher energy than the conduction band energy of the GaAs. Consequently, the electrons in the AlGaAs diffuse into the GaAs layer until charge equlibrium occurs. The carrier diffusion produces a large electric field (~ 100 kV/cm) which causes band bending. The band bending results in the formation of a quasi-triangular potential well. The quantization takes place in the dimension perpendicular to the heterostructure, resulting in unrestrained electron motion parallel to the interface

(1). The electron system is thus two dimensional and is referred to as a two-dimensional electron gas (2DEG). The separation of ionized impurities in the AlGaAs from the conduction electrons in the GaAs creates increased carrier mobility due to the reduction of ionized impurity scattering.

A typical MODFET device is illustrated in Fig. 2 (3). This device is employed in a normally-off configuration where the gate depletion region extends into the two-dimensional electron gas connecting the source and drain, cutting off conduction. In the normally off condition, the gate and source are kept at the same voltage. Once the gate voltage is 0.6 to 0.8 V higher than the source, the depletion region is moved up into the undoped AlGaAs layer and conduction ensues. The isolation region serves to separate MODFET devices on the same integrated circuit. The n^+ GaAs cap layer prevents oxidation of the AlGaAs layer and allows low resistance ohmic contacts for the drain and source (2). The ohmic metal is usually n AuGe/Ni/Au alloy. A Schottky contact is formed when the gate metal is placed on top of the AlGaAs layer. Typically, a thick, undoped GaAs buffer layer (~ 1 um) is placed between the MODFET and the substrate to provide a smooth surface on which to grow the MODFET. The substrate is composed of GaAs which is Cr-doped. This provides a semi-insulating layer which prevents stray conduc-

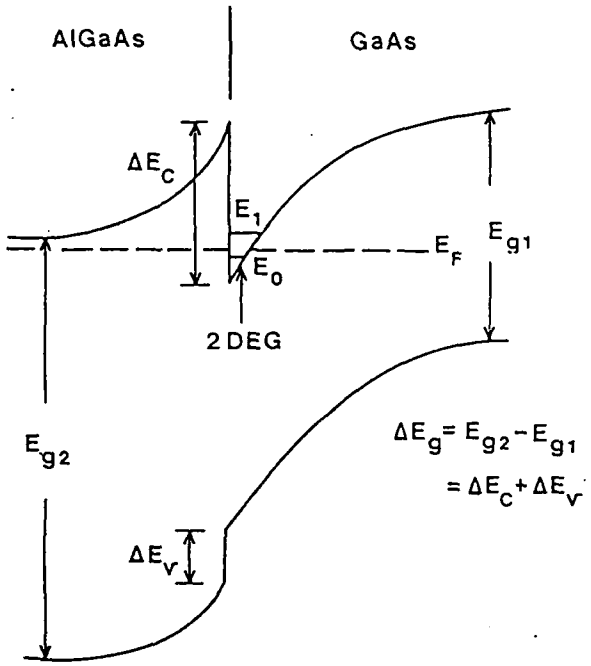

Figure 1. MODFET energy band structure showing band offset ΔE_C and ΔE_V, and quantized energy levels E_0 and E_1 in the quasi-triangular potential well. (From Ref. 2)

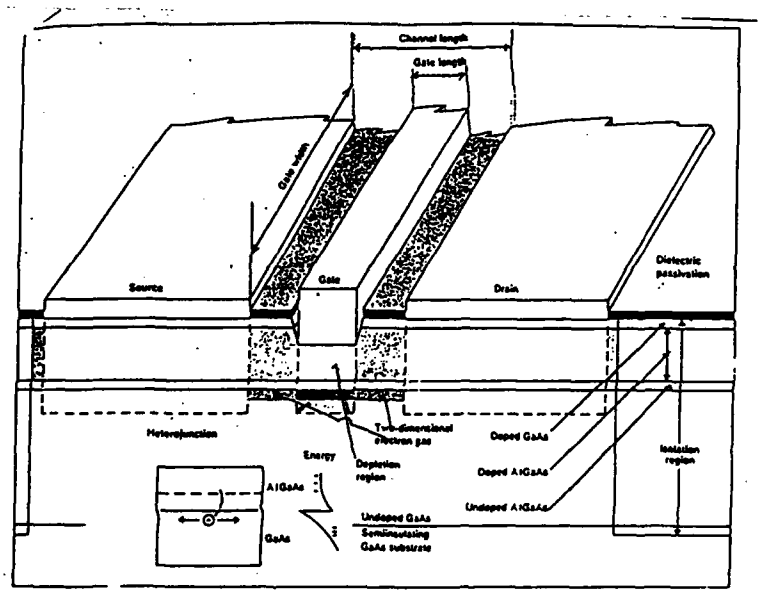

Figure 2. Schematic diagram of MODFET construction for IC application. (From Ref. 3)

tion and decreases parasitic capacitance.

From a device standpoint, the main advantage of the MODFET is the positioning of a large electron density ($\sim 10^{19}$ cm^{-3}) in a thin layer (~80 A) very close to the gate (~300 A). These factors permit large currents (~500 mA/mm) to be switched at very high speeds ($\sim 10^{-10}$ s @ 300 K) allowing exceptionally fast capacitor charging times with reduced power consumption (~1 mW @ 300 K) (4).

To enhance the device properties of the MODFET, undoped AlGaAs spacer layers and selective doping are used. The spacer layer is placed between the doped AlGaAs and undoped GaAs layers. The spacer layer (shown schematically in Fig. 3) provides increased isolation between the ionized donors in the doped AlGaAs and the 2DEG. This quality further reduces ionized impurity scattering and enhances the band structure by increasing the conduction band offset. An planar layer of single atom Si ($\sim 10^{12}$ cm^{-2}) - called "delta" doping - can be placed in the undoped spacer layer close to the GaAs well. The close proximity of the delta doped layer to the well produces an additional supply of conduction electrons, thus increasing the 2DEG concentration. Improvements in 2DEG concentration of 30% with almost the same mobility have been realized using delta doping (5).

MODFET structures where the GaAs layer is grown on top of the AlGaAs have received much attention in recent

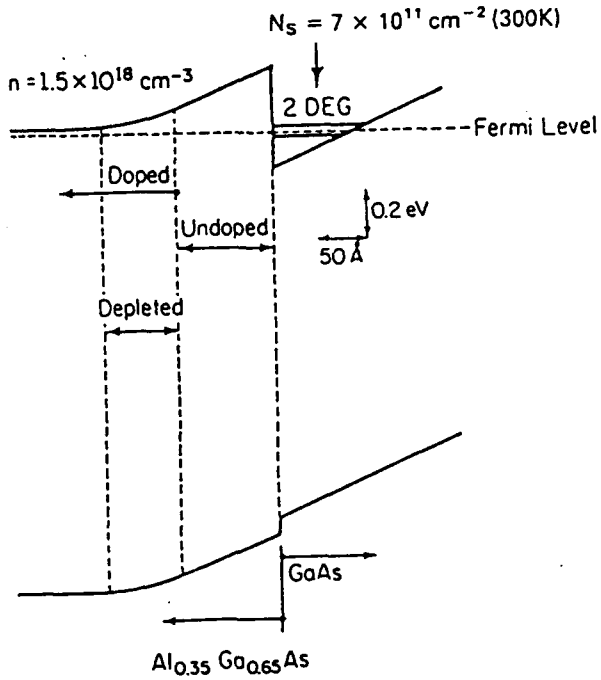

Figure 3. MODFET energy band diagram showing the undoped AlGaAs spacer layer and depletion region. (From Ref. 6)

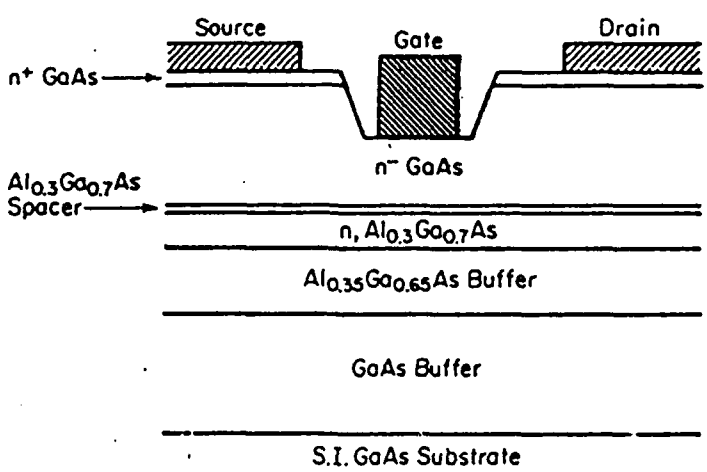

Figure 4. Schematic of an "inverted" MODFET (from Ref. 4).

years. A typical "inverted" configuration is provided in Fig. 4. It is composed of an undoped AlGaAs buffer layer, a doped AlGaAs layer, an undoped AlGaAs spacer layer and a GaAs cap layer. The GaAs layers at the source and drain are doped n^+ in order to make ohmic contacts at these points.

One problem with this technology is that inverted structures have exhibited degraded mobility characteristics. A number of growth techniques have been employed to counter this undesirable quality and are discussed later.

An inverted MODFET using a wide bandgap superlattice is shown in Fig. 5. The 25 period undoped superlattice on top of the GaAs buffer layer prevents the transfer of electrons into the buffer layer. The 10 period superlattice contains a 15 A donor doped (10^{18} cm^{-3}) GaAs layer sandwiched between undoped 5 A GaAs layers. The dopants reside at shallow donor levels in the GaAs portion of the superlattice and provide higher electron sheet densities for the 2DEG. Thus this superlattice takes the place of the doped AlGaAs layer found in the conventional MODFET. The 5 A undoped GaAs layers in this superlattice are used to prevent Si incorporation in the AlAs. The four period undoped superlattice provides a spacer region which further reduces ionized impurity scattering between donors in the doped superlattice and the 2DEG.

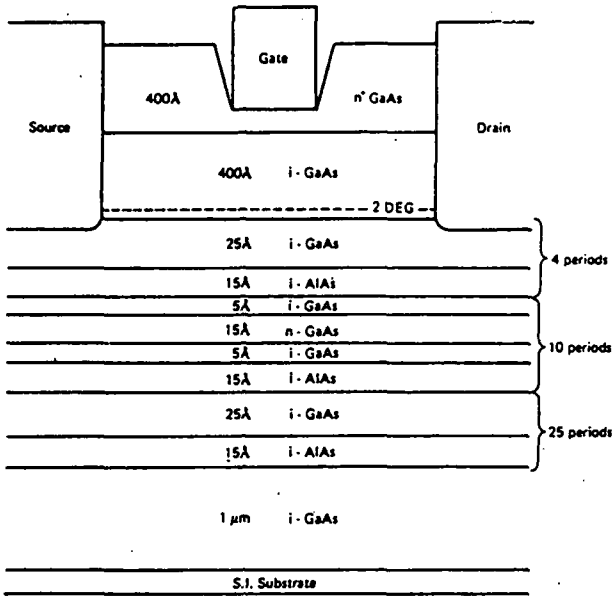

Figure 5. Cross sectional view of an inverted MODFET with GaAs/AlAs superlattices (from Ref. 4).

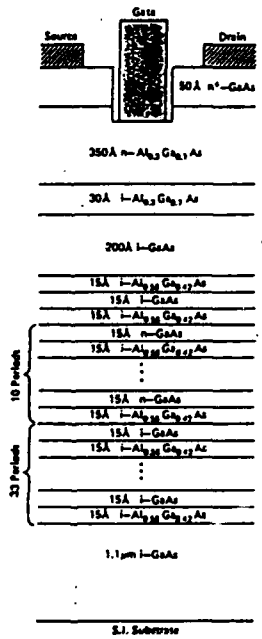

Figure 6. A double-heterointerface MODFET grown on a three superlattice structure (from Ref. 4).

A third type of MODFET employs quantum wells and uses both the inverted and a normal interface. A thin GaAs layer (~ 300 A) is sandwiched between two doped AlGaAs layers forming a quantum well. The 2DEG concentration is increased since electrons are available from both barrier layers at each interface, thereby increasing the current carrying capability (4). The gate to 2DEG distance is kept small since the GaAs layer is thin. An example of a double-heterointerface (quantum well) MODFET is given in Fig. 6. The structure has a 1.1 um GaAs buffer layer with a 33 period undoped GaAs superlattice, a 10 period n-doped GaAs superlattice, and a one and a half period superlattice used as a spacer layer. The 10 period superlattice is used as a carrrier supplying layer for the quantum well similar to that in Fig. 5. The 33 period superlattice is used as barrier layer to prevent electron transfer into the buffer layer.

MODFET integrated circuits for high speed computer applications are under development at numerous laboratories. One example is an integrated frequency divider circuit built with 0.5 um gate length MODFETs (7). Performance at 5.5 GHz at 300 K has been demonstrated with logic delays of 22 ps/gate and power dissipation of 2.9 mW/gate and a fanout of two. The speed of this device is roughly three times faster than that of conventional GaAs MESFET technology. Of critical importance is the layer thickness

of the n-AlGaAs layer below the gate. This thickness determines threshold voltage and transconductance. Wafer homogeneity is thus crucial and must be carefully monitored. VASE has been implemented to fufill the task of determining the thickness uniformity in MBE growth (8).

As another example, a 1-kbit static RAM has been developed using MODFET LSI technology (9). This IC is fully operational, employing 7,244 MODFETs on a chip with dimensions 3.0 mm X 2.9 mm and 100 chips per wafer. Deviations in access time were +/- 4% which is much smaller than that of GaAs MESFET SRAMs. Uniformity in gate threshold voltage was excellent (with variations less than +/- 0.05 V) due to the high layer thickness uniformity (+/- 1%) obtained during MBE growth and a self-terminating selective dry etching-process.

References

1) A.C. Gossard, in Molecular Beam Epitaxy and Heterostructures, Edited by: L.L. Chang and K. Ploog, Martinus-Nijhoff, (1985).

2) P.H. Ladbrooke, in Gallium Arsenide for Devices and Integrated Circuits, Edited by: H. Thomas, et. al., Peter Peregrinus Ltd., London, (1986).

3) H. Morkoc and P.M. Solomon, IEEE Spectrum, 28, February (1984).

4) T.J. Drummond, W.T. Masselink and H. Morkoc, Proc. of the IEEE **74**, 773, (1986).

5) T. Ishiwaka, et. al., J. Appl. Phys. **61**, 1937, (1987).

6) H. Morkoc, in The Physics and Technology of Molecular Beam Epitaxy, Edited by: E.H.C. Parker, Plenum Press, (1985).

7) M. Abe, T. Mimura, K. Nishiuchi, A. Shibatomi and M. Kobayashi, IEEE GaAs IC Symposium, 158, (1983).

8) S.A. Alterovitz, P.G. Snyder, K.G. Merkel, J.A. Woollam, D.C. Radulescu and L.F. Eastman, to be published in J. Appl. Phys., (1987).

9) N. Kobayashi, et. al., IEEE Trans. Elect. Dev. **ED-33**, 548, (1986).

B. Molecular Beam Epitaxial Growth of Quantum Wells and Superlattices

Molecular beam epitaxy (MBE) is a method for growing very thin semiconductor layers of high quality and uniformity. Due to the lower growth temperatures used in the MBE process (~ 625 °C), more abrupt layer interfaces can be grown when compared with the vapor phase epitaxy (VPE) (~ 700 °C) and liquid phase epitaxy (LPE) (~ 800 °C) methods (1). Metal organic chemical vapor deposition (MOCVD) is a technology with growth temperatures and defect densities comparable to MBE. MOCVD has a higher wafer throughput and lower basic system cost. Considerable research and development effort is going into the improvement of MOCVD. However, the high degree of growth control obtainable with the MBE shutters allows the MBE system to produce the thinnest layers and most abrupt dopant transitions (2) at the present time. The above mentioned advantages, combined with the capability of monitoring the wafer surface during growth, make MBE an ideal instrument for realizing the structural properties required for quantum wells and superlattices.

The MBE process is one of species evaporation under ultra-high vacuum (UHV), involving the reaction of thermal atomic (or molecular) beams with a heated substrate. The growth rate is generally low - around 1 mm/hr (i.e. approximately one monolayer per second). This rate allows

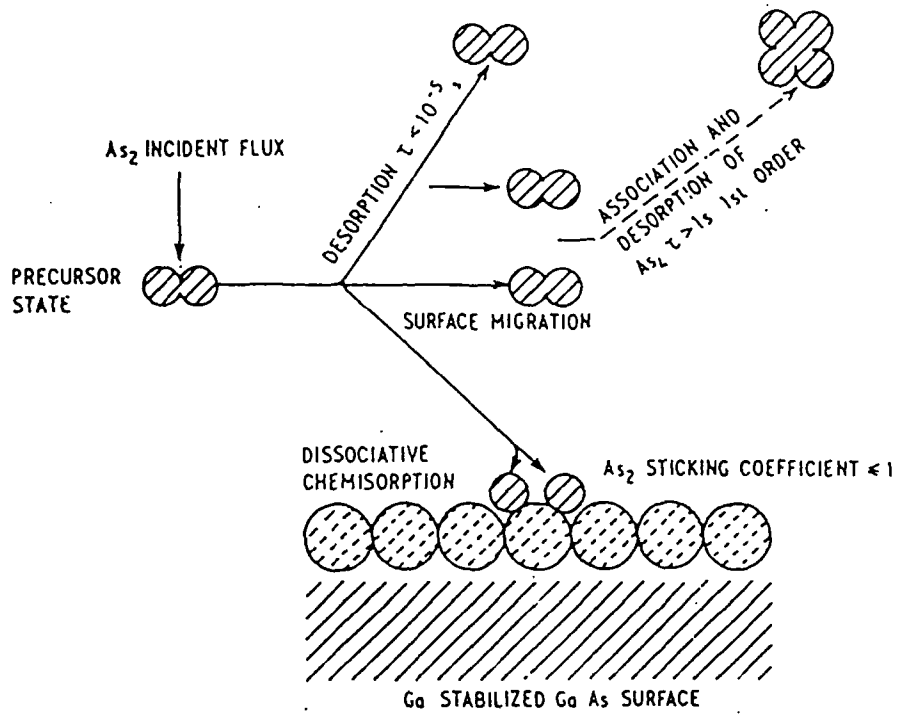

Figure 1. Chemical process for MBE grown GaAs (from Ref. 1).

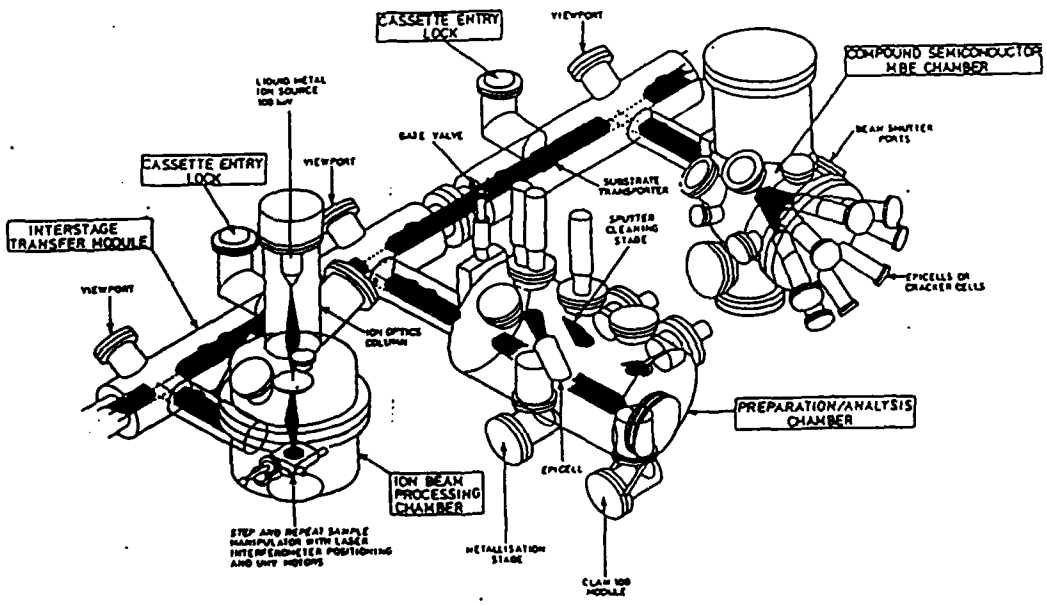

Figure 2. MBE growth system layout (from Ref. 1).

cient of the As_2 is unity. Theoretically, each Ga atom site will have an As_2 dimer attached to it and complete coverage of the Ga monolayer by an As monolayer will take place. If the As_2 coverage is not complete, a Ga rich surface is produced along with an increased defect density producing deep impurity levels.

A typical MBE system is shown in Fig. 2. The wafer is placed in the MBE machine through the cassette entry lock. From there, it is transported to the preparation/analysis chamber where: 1) surface analysis using Auger electron spectroscopy (AES) or X-ray photoelectron spectroscopy (XPS) is performed, 2) the sample is preheated in order to outgas it, and 3) metallic contacts are deposited. The sample is then sent to the MBE chamber where the molecular beams are generated from Knudsen effusion cells and the fluxes are measured by a mass spectrometer. Several Knudsen cells may be incorporated into the growth chamber in order to dope the wafer or provide multicomponent alloys and compounds.

The growth process can be monitored by surface studies using reflection high energy electron diffraction (RHEED). The RHEED system measures surface quality by directing an electron beam on the sample at a glancing angle. The reflected beam produces diffraction patterns on a fluorescent screen. The relative diffraction intensities indicate monolayer growth with the maximum intensity

occurring for each successive monolayer. Due to the lack of total coverage of successively grown layers, MBE surfaces become less smooth as growth continues. The contributions to the diffraction pattern from these partially grown layers (unsmooth layers produce diffraction minima) causes the RHEED intensities to die out after approximately 100 monolayers. This limitation renders the RHEED process an incomplete method for monitoring layer growth, and provides an ideal application for VASE which can be applied in situ or after growth.

Of particular interest in MBE growth is impurity incorporation during the growth process. When the binary (GaAs) layer is grown on top of the ternary (AlGaAs), the interface has been observed to contain more impurities and roughness than with the ternary grown on binary (6,7,8). This effect is prevalent in superlattices which contain multiple interfaces and "inverted" MODFETS. Decreased mobility is observed (compared to the normal interface) due to the presence of acceptor levels in the GaAs produced by growth-related carbon impurities (7). The free electrons recombine with the acceptor level holes, thus reducing the number of electrons available for conduction.

Roughness at the interface has been attributed to: 1) noncrystallinity associated with slight lattice mismatch, 2) differences in migration length (the distance an atomic or molecular species travels along the surface before in-

corporation) between Ga and Al, and 3) residual oxygen incorporation. The lattice mismatch between GaAs and AlGaAs (~ 0.1 %) can lead to tensile strain perpendicular to the interface causing roughness (9). Roughness on the order of multiple monolayers is possible due to the larger migration length of Ga (150 A) than Al (35 A) from the AlGaAs surface during growth. The surface migration rate for Ga atoms is longer than that of the Al atoms due to the Ga-As bonds being weaker than the Al-As bonds. Consequently, the inverted interface will be rougher than the normal interface where only GaAs atoms are present (10). The high reactivity of oxygen with Al is also a possible cause of impurity related roughness. Surface strain on the growing AlGaAs layer induces oxygen precipitation. Subsequently, oxygen burial takes place in the first few monolayers of the GaAs with the O atoms being substitutionally incorporated at As sites (8). Also, oxygen incorporation contributes to deep levels within the GaAs, causing undesirable recombination.

Several growth techniques have been implemented to counter the problems associated with inverted interfaces. Residual impurities (such as O and C) float on the AlGaAs growth surface and prevent lateral propagation of the source species thus causing nonuniform surface growth and roughness. The growth of a superlattice below the GaAs quantum well has reportedly yielded considerably smoother

GaAs-AlGaAs interfaces (6,9). This improvement is attributed to lattice-strain induced diffusion of carbon and oxygen impurities into the AlGaAs layers of the superlattice during cooling to room temperature. A second technique involves the interruption of the growth after the deposition of the AlGaAs layer. This reduces the roughness to only a single monolayer at the AlGaAs surface and reduces residual impurity diffusion in the first few GaAs monolayers (10).

Improvements in MBE methods have permitted the growth of "strained" layer superlattices. These structures are characterized by materials with lattice mismatches in the 0.1% to 1% range which greatly enhances the number of materials that can be grown epitaxially on a given substrate (11). For example, InAlAs/InGaAs MODFETs (lattice mismatch approximately 2%) grown by MBE have exhibited room temperature mobilities 50% higher than similar AlGaAs/GaAs systems (12). Lattice mismatch between the layers is totally accomodated by strain in the layers instead of at the interfaces where strain causes dislocations (13). The electronic properties of lattice mismatched layers are different from those of bulk materials due to strain effects on the band structure. (9,11).

References

1) W.G. Herrenden-Harker and R. H. Williams, in Gallium Arsenide for Devices and Integrated Circuits, Edited by: H. Thomas, et. al., Peter Peregrinus Ltd., London, UK, (1986).

2) J.D. Grange and D.K. Wickenden, in The Physics and Technology of Molecular Beam Epitaxy, edited by E.H.C. Parker, Plenum Press, New York, N.Y., (1985).

3) G.J. Davies and D. Williams, in The Physics and Technology of Molecular Beam Epitaxy, edited by E.H.C. Parker, Plenum Press, New York, N.Y., (1985).

4) C.T. Foxon, J. Vac. Sci. Technol. B **1**, 293, (1983).

5) B.A. Joyce, in Molecular Beam Epitaxy and Heterostructures, edited by L.L. Chang and K. Ploog, Martinus Nijhoff Publishers, (1985).

6) P.M. Petroff, R.C. Miller, A.C. Gossard and W. Wiegmann, Appl. Phys. Lett. **44**, 217, (1984).

7) R.C. Miller, W.T. Tsang and O. Munteanu, Appl. Phys. Lett. **41**, 374, (1982).

8) T. Achtnich, G. Burri, M.A. Py and M. Ilegems, Appl. Phys. Lett. **50**, 1730, (1987).

9) T.J. Drummond, J. Klem, D. Arnold, R. Fischer, R.E. Thorne, W.G. Lyons and H. Morkoc, Appl. Phys. Lett. **42**, 615, (1983).

10) D.C. Radulescu, G.W. Wicks, W.J. Schaff, A.R. Calawa and L.F. Eastman, J. Appl. Phys. **61**, 2301, (1987).

11) J.Y. Marzin, in Heterojunctions and Semiconductor Superlattices, Edited by: G. Allan, et. al., Springer-Verlag, (1986).

12) J. Singh, IEEE Electron Dev. Lett. **EDL-7**, 436, (1986).

13) K.Ploog, in The Physics and Technology of Molecular Beam Epitaxy, edited by E.H.C. Parker, Plenum Press, New York, N.Y., (1985).

C. Excitons in Quantum Wells and Superlattices

Photon absorption in a semiconductor can create a bound electron-hole (e-h) pair called an exciton. The e-h pair is bound by the Coulombic interaction between the two particles and can transport energy within the crystal without transporting charge (1). Spectroscopically, these excitations are exhibited in bulk materials at energies equal to the band gap of the semiconductor minus the binding energy of the exciton.

Excitons are normally classified into two types: Frenkel or Mott-Wannier. Excitons belonging to the Frenkel class are tightly bound e-h pairs localized near a host atom. They appear as an excited state of a single atom which may move from site to site on the lattice through nearest neighbor coupling. Frenkel excitons are prevalent in relatively ionic materials and hence have large binding energies (typically 1 eV). Mott-Wannier excitons, on the other hand, are weakly bound and are present in covalently bonded materials. The Mott-Wannier exciton is thus found predominantly in semiconductors. The Mott-Wannier exciton has an e-h separation distance which is large compared with the crystal lattice constant, producing relatively small binding energies (typically from 3 to 40 meV) (1,2).

Excitonic transitions in quantum wells and superlattices are easily discernible in optical spectra.

Since electrons and holes can only occupy quantized energy levels within a quantum well, the excitons in quantum wells are quantized. The quantized recombination transitions in optical spectra produce a sharper structure when compared to transitions from the valence band to the conduction band continuum in a bulk semiconductor (3). Consequently, excitons can produce changes in optical spectra that are larger than those for equal densities of free e-h pairs (i.e., the exciton resonance peaks are displaced from the continuum) (4).

Excitonic effects are enhanced in thin layer semiconductors due to increased carrier confinement. The exciton binding energy is larger in a quantum well than in the bulk. A decreased physical separation between the electron and hole, as a result of carrier confinement, causes an increase in the Coulombic potential and hence a larger binding energy. For example, E_{ex} = 4.2 meV in bulk GaAs and E_{ex} = 9.1 meV in a single, 50 A width, GaAs quantum well with an Al barrier composition x = 0.3 (5). The binding energy of an exciton (either in a bulk material or a quantum well system) is described by

$$E_{ex} = \frac{e^4 \mu}{\epsilon^2 h^2} (n - 1/2)^{-2} \qquad (1)$$

where μ is the effective mass of the exciton and n is the quantum state.

Of particular interest are electro-optical effects produced by excitons when an electric field is applied to

a quantum well or superlattice (6). The presence of the electric field promotes a high degree of optical nonlinearity in these structures due to the spectral shifting of the absorption edge as explained below. In addition, excitonic transitions in quantum wells take place at room temperature as opposed to bulk materials where they occur only at very low temperatures. This difference between bulk and quantum well excitons occurs because quantized energy levels in the quantum wells provide much sharper excitonic transition energies than bulk material even at room temperature. In the bulk regime, as the temperature is increased, electrons are thermalized in greater numbers and occupy a larger number of states in the conduction band thus producing a quasi-continuum of exciton energies near the band gap energy. Therefore, bulk excitonic transitions are thermally broadened at room temperature and do not possess the sharp absorption edges necessary for opto-electronic applications. This combination of nonlinearity and ambient temperature operation permits the application of these structures as electro-optical switches and modulators.

When an electric field is applied perpendicular to the layers, a small broadening and shifting of the exciton peaks to lower energies is observed - commonly referred to as the quantum Stark effect (6,7,8). This can be seen in Fig. 1 where the peaks in the absorption spectrum of the

quantum well are seen to move to lower energies with the application of electric field strengths of 16 kV/cm in (b) and 50 kV/cm in (c). The shift to lower energies is caused by binding energy decreases due to the decrease in Coulomb attraction between the e-h pair as they move to opposite sides of the well. In Fig 1 (c), the excitonic peaks are much less resolvable than in 1 (a). This broadening of the peak intensities occurs because the increase in field strength promotes tunneling due to the shifting of the carrier concentration and a decrease in the barrier width. This process is shown in the energy band diagram above the figure. Therefore, the Stark effect produces nonlinear absorption characteristics since a change in the electric field does not yield the same absorption spectrum as the no field condition. This property is an advantage in that the absorption edge can be moved into a region where the sample is transparent in the absence of a field thus making it possible to control (modulate or switch) the transmitivity of a quantum well device.

The spectral shift is also a function of well width (8). In quantum wells of width greater than 50 A the Stark shift is prevalent in photoluminescence (PL) spectra. However, for wells less than 50 A wide, the exciton absorption peaks broaden and shift to higher energies when an electric field is applied. For wells less than 50 A the Stark effect is less prevalent because the electron to

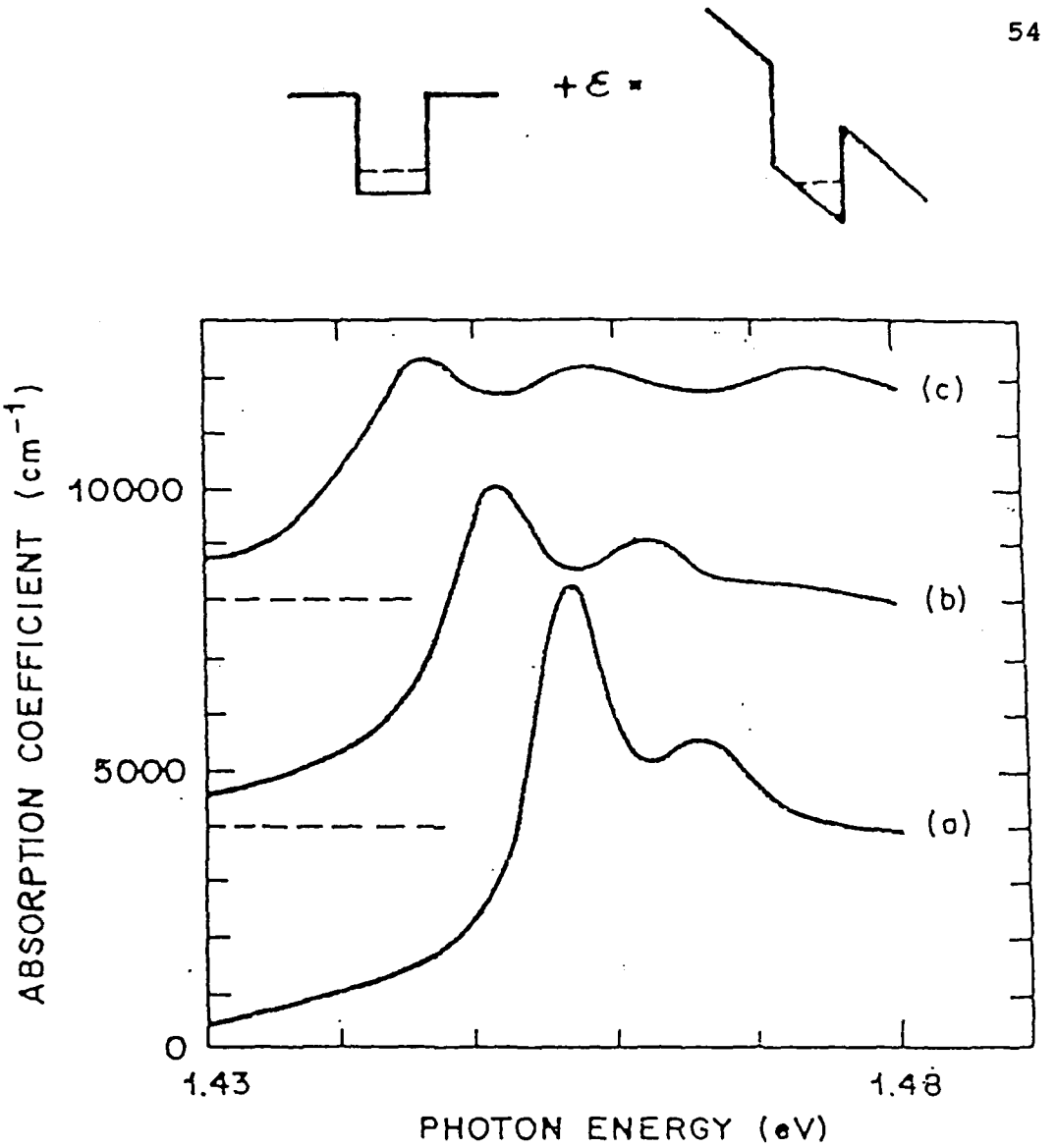

Figure 1. Absorption spectrum for a multiple quantum well structure with applied fields: (a) no field, (b) 16 kv/cm and (c) 50 kV/cm (from Ref. 6).

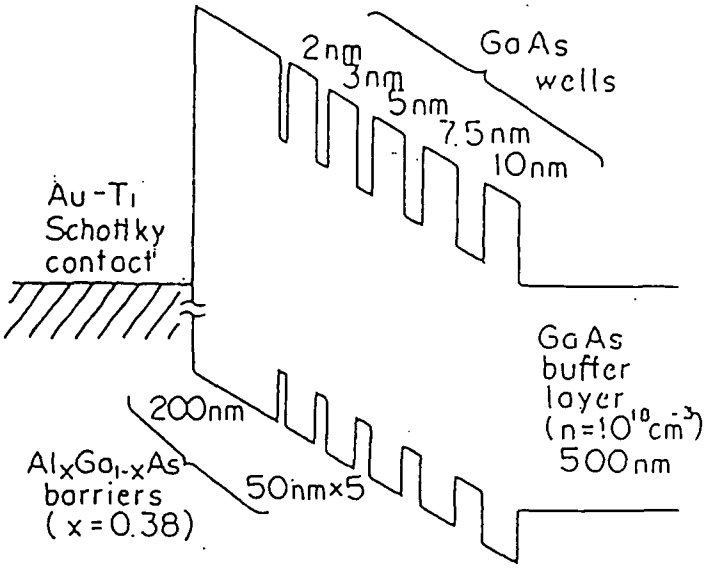

Figure 2a. Schematic energy diagram of MQW (from Ref. 8).

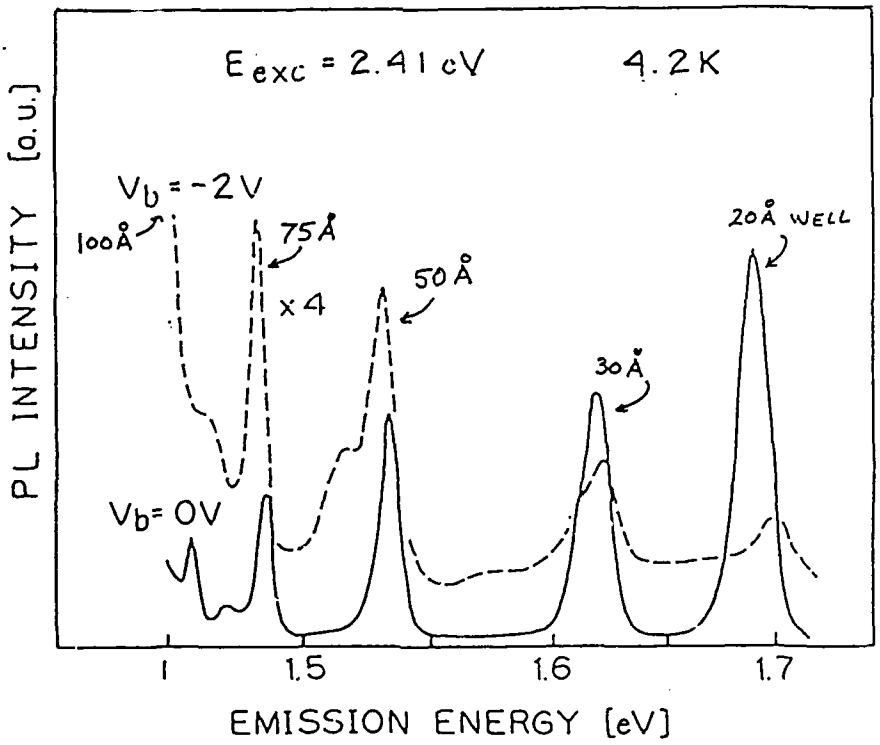

Figure 2b. PL spectrum of MQW with 0 and -2 V applied (Ref. 8).

hole distance doesn't increase appreciably with bias. Therefore, the binding energy doesn't noticeably decrease with an applied bias. The shift to higher energies of the PL peaks of the thin wells is suggested as being caused by an anti-Stokes electron-phonon interaction. These electrons thus have a higher recombination energy. The anti-Stokes effect occurs for the thicker wells; however the Stark effect is stronger for these wells. These two effects are shown in the PL spectra of Fig. 2b for a multiple quantum well structure (Fig 2a) containing five quantum wells of varying width under a -2.0 V reverse bias.

References

1) C. Kittel, Introduction to Solid State Physics, John Wiley and Sons, Inc., 6th Edition, (1986).

2) K. Cho, Excitons, Editor: K. Cho, Springer-Verlag, (1979).

3) M. Altarelli, Heterojunctions and Semiconductor Superlattices, Edited by: G. Allan, et. al., Spriger-Verlag, (1986).

4) D.S. Chemla and D.A.B. Miller, J. Opt. Soc. Am. B. **2**, 1155, (1985).

5) R.L. Greene and K.K. Bajaj, Solid State Commun. **45**, 831, (1983).

6) D.S. Chemla, Proc. of Basic Properties of Optical Materials, Edited by: A. Feldman, NBS Publication 697, 202, (1985).

7) M. Erman, P. Frijlink, J.B. Theeten, C. Ailbert and S. Gaillard, Inst. Phys. Conf. Ser. No. 74, 327, (1985).

8) M. Naganuma, T. Ishibashi and Y. Horikoshi, J. Appl. Phys. **62**, 644, (1987).

9) T.H. Wood, C.A. Burrus, D.A.B. Miller, D.S. Chemla, T.C.Damen, A.C. Gossard and W. Wiegemann, to be published.

D. Quantum Well Optoelectronics

There exist a number of applications for III-V heterostructures in the area of optoelectronics including: electro-optic modulators (2), superlattice avalanche photodiodes (3), quantum-well envelope state transition devices (QWEST) (8), and multiple quantum-well optical interference filters (4). Two of the most promising technologies are presented here, these are the: heterostructure quantum well laser, and self electrooptical effect device.

1. The Heterostructure Quantum Well Laser

The optical and carrier confinement available from a heterostructure quantum well provides an ideal system for a semiconductor laser. The physical construction of a such a device is shown in Fig. 1. The device is composed of two heterojunctions forming an undoped GaAs quantum well bounded at either interface by n or p-doped AlGaAs. When a forward bias is applied, electrons and holes are injected into the well from the n and p AlGaAs repectively. Population inversion is achieved in the junction due to the excess number of electrons in the quantized conduction levels and the absence of electrons in the valence levels. This process is shown in Fig. 2. In the junction region electrons can recombine with holes by falling to lower energy levels and emitting photons. The recombination radiation may interact with valence band

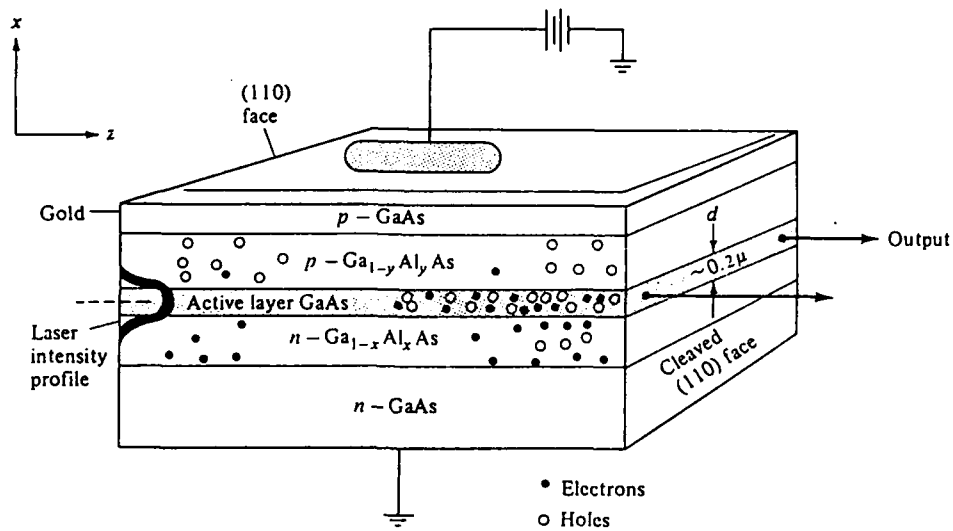

Figure 1. A double heterostructure GaAs/AlGaAs laser (from Ref. 1).

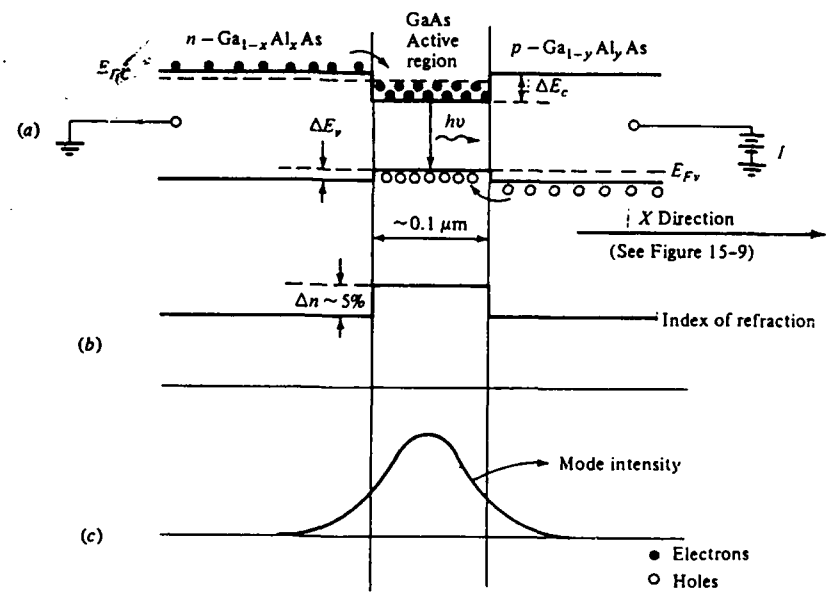

Figure 2. a) The energy bands of a forward biased GaAs/AlGaAs laser, b) the index of refraction profile and c) the intensity profile (from Ref. 1).

electrons and be absorbed or interact with conduction band electrons and create more photons by stimulated emission. The laser cavity is provided by the cleaved (110) faces forming the mirror surfaces of a Fabry-Perot etalon. The index of refraction and intensity profiles are also illustrated in Fig. 2.

A major advantage is associated with the quantum well energy quantization: recombination can proceed between electrons at a fixed energy level with holes at a fixed energy level. This feature is shown in Fig. 3 where the energy as a function of the density of states for electrons and holes in a quantum well structure are superposed on that of a bulk sample. Shown are four transitions involving the step-like density of states that are sources of possible laser emission lines. In a bulk material, the carriers are distributed in a continuum of energy levels. Thus narrow linewidths are not as realizable with a bulk semiconductor since recombination cannot occur at fixed energies (5).

Of critical importance in the design of QW lasers is the well width. For $d < 100$ A, the well width approaches the electron scattering path length, l_p. Under this condition, electrons are not scattered sufficiently to thermalize in a large density from the conduction band edge in the AlGaAs to the quantized states in the GaAs (5,6). In this case, the electrons may pass from the

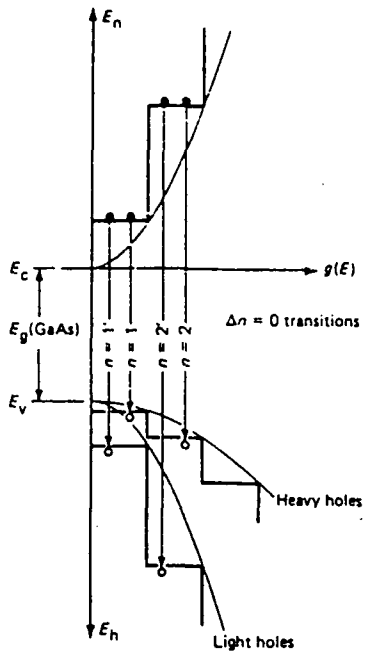

Figure 3. Density of states diagram for an AlGaAs/GaAs quantum well (from Ref. 6).

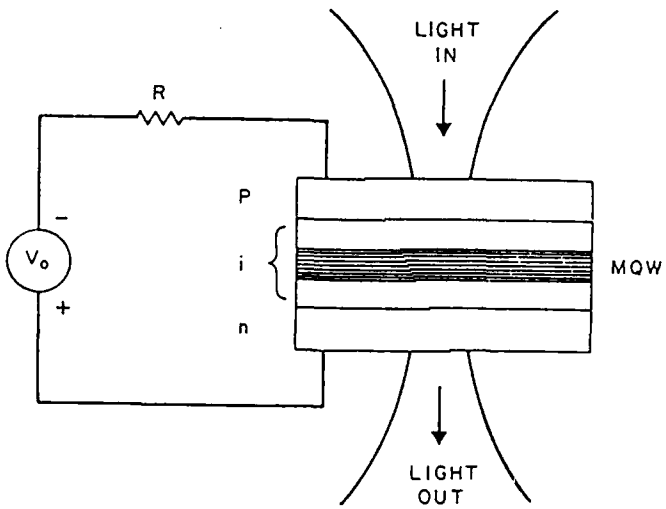

Figure 4. Schematic of the quantum well SEED (from Ref. 11).

n-type AlGaAs layer directly to the p-type AlGaAs layer. The electrons then recombine with the holes in the AlGaAs at energies higher than the GaAs transition energies and with lower efficiency. By growing multiple quantum well structures with thin barrier layers, this limitation can be overcome (6,7). Quantum coupling (tunneling) is then present between neighboring wells which makes the overall active region much larger than l_p. It is less probable that an electron or hole will recombine in the AlGaAs barrier region . Therefore, if an electron isn't scattered at one quantum well, it only has to cross a thin barrier layer before being scattered at the next well. Using this technique, excess carriers are effectively collected in the quantum states of the GaAs wells and thermalized

2. Self Electro-optical Effect Device (SEED)

The quest for optical computers capable of parallel processing, switching and exceptionally fast operation is receiving much attention (8,9). This concept couples together the areas of holography, fiber optics, Fourier optics and semiconductor lasers, and envisions the utilization of the superior characteristics of photon computing (either in lieu of, or in addition to computing using electrons).

To achieve bistable operation a system must have two stable output states for the same input over some range of input values. Two methods of obtaining optical

bistability are: nonlinear optical interference filters and nonlinear positive feedback etalons. The Self Electro-optical Effect Device (SEED) is an optically bistable switching device which employs the nonlinearity of a MQW modulator and photodetector. The operation of the SEED is illustrated in Fig. 4. (11). It is composed of a p-i-n diode containing a MQW, a series resistor (R) and a voltage supply (V_0). To provide switching capability, the incident light wavelength is chosen to be near the exciton resonance for zero voltage across the diode (call this wavelength λ_1). With low optical power, almost all of the supply voltage is across the diode because there is little photocurrent. This voltage provides an electric field which is perpendicular to the interfaces of the MQW. This field shifts the exciton absorption resonance to higher wavelengths (the Stark effect) and the optical absorption becomes relatively low. Increasing the intensity increases the photocurrent, decreasing the voltage across the diode. The reduced diode voltage moves the exciton resonance back toward λ_1 increasing the absorption. This action further increases the photocurrent which leads to regenerative feedback - the cycle of increasing absorption producing more photocurrent leading to decreased voltage - and switching.

This process can be further explained by viewing the theoretical implications of optical bistability with re-

spect to absorption (10). The output power, P_r, of a medium with absorption, A, and system losses (i.e. reflection and scattering), ρ, can be expressed by

$$P_r = \rho(1-A)P = TP \tag{1}$$

where T is the transmission of the medium and P is the input light power. Also, we can identify an excitation parameter, N, by N = AP which indicates the total amount of power absorbed. In this case, the absorption will be nonlinearly related to the excitation. Equation (1) is readily plotted against N for various values of P as shown by the straight lines in Fig. 5a. Included in Fig. 5a is a measured plot of T vs. N for a GaAs/AlGaAs MQW structure showing the nonlinear relationship between transmission and excitation. The intersections labelled A through D represent solutions for particular input power values. Lines A and D intersect once, lines B and C twice, indicating one and two solutions respectively. The transmission properties can be used to determine the transmitted power as a function of input power, shown in Fig. 5b. The system is clearly bistable since the points B and C have two different output states for the same input power.

A SEED has been designed and tested at room temperature using a MQW consisting of 50 layers of 95 A GaAs wells and 98 A undoped AlGaAs (11). The device exhibited extremely low switching energies per unit area (~4 fJ/um^2 incident optical and ~14 fJ/um^2 electrical). The switch-

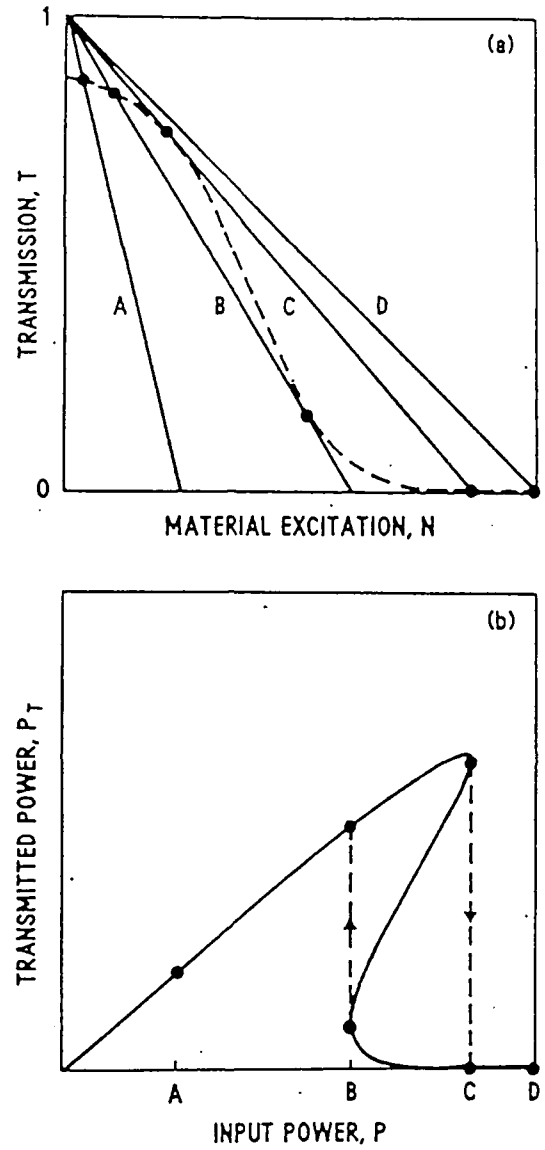

Figure 5. a) Graphical solution of bistability for a GaAs/AlGaAs MQW. b) Transmitted power vs. input power for an optically bistable device (from Ref. 10).

ing power was inversely proportional to the resistance and switching time was proportional to R. The power-delay product was approximately 1.5 nJ for each value of resistance.

References

1) A. Yariv, Optical Electronics, CBS College Publishing, New York, NY, (1985).

2) D.R.P. Guy, N. Apsley, L.L. Taylor, and S.J. Bass, SPIE Vol. **792**, "Quantum Well and Superlattice Physics", 189, (1987).

3) W.T. Tsang, in The Physics and Technology of Molecular Beam Epitaxy, edited by E.H.C. Parker, Plenum Press, (1985).

4) P.L. Gourley, R.M. Biefeld, T.J. Drummond, and T.E. Zipperian, SPIE Vol. **792**, "Quantum Well and Superlattice Physics", 178, (1987).

5) N. Holonyak, Soviet Phys. of Semicond. **19**, 943, (1985).

6) N. Holonyak, R.M. Kolbas, R.D. Dupuis and P.D. Dapkus, IEEE J. Quant. Elect. **QE-16**, 170, (1980).

7) G.S. Jackson, N. Holonyak, D.C. Hall, J.E. Epler, R.D. Burnham and T.L. Paoli, J. Appl. Phys. **62**, 381, (1987).

8) T.E. Bell, IEEE Spectrum, 34, August (1986).

9) H.M. Gibbs, et. al., Appl. Phys. Lett. **41**, 221,

(1982).

10) D.A.B. Miller, A.C. Gossard and W. Wiegmann, Opt. Lett. **9**, 162, (1984).

11) D.A.B. Miller, D.S. Chemla, T.C. Damen, A.C. Gossard, W. Wiegmann, T.H. Wood and C.A. Burrus, Appl. Phys. Lett. **45**, 13, (1984).

E. Direct Interband Transitions in Semiconductors

The behavior of optical spectra, measured by ellipsometry, is governed by absorption processes. In this section, interband transitions for direct gap semiconductors are considered by deriving the expressions for interband transition rate, joint density of states, and critical points. These concepts are then applied to the GaAs optical spectrum.

The relations for interband transition effects are derived from first order perturbation theory (1,2,3). The perturbation approach is used since an incident light beam produces an electric field in the semiconductor. The majority of this section is taken from Wooten (1).

The electric vector potential (A) of the applied light wave can be expressed as

$$\bar{A} = \frac{1}{2} A \bar{a}_0 \left\{ \exp\left[i(\bar{q}\cdot\bar{r} - \omega t)\right] + \exp\left[-i(\bar{q}\cdot\bar{r} - \omega t)\right] \right\} \qquad (1)$$

where a_0 is the unit polarization vector and q is the wave vector. The Hamiltonian of a semiconductor system under radiation is modified to include a perturbation term

$$H = H_0 + H'(\bar{r}, t) \qquad (2)$$

Here H_0 and $H'(r,t)$ are the unperturbed and perturbed components respectively. H can then be expressed as the sum of four terms. These terms represent the kinetic energy, the potential energy of the ith electron due to the ionic cores, the Coulombic interaction of the electrons, and the interaction energy of the ionic cores, respectively.

$$H = \frac{1}{2m} \sum_{i=1}^{N} \left[\bar{p}_i - \frac{e}{c} \bar{A}(\bar{r}_i, t) \right]^2 + \sum_{i=1}^{N} V_i(\bar{r}_i)$$

$$+ \frac{1}{2} \sum_{\substack{i,j \\ i \neq j}} \frac{e^2}{|\bar{r}_i - \bar{r}_j|} + I \tag{3}$$

where the index, i, is summed over the N electrons per unit volume (the second term in the brackets is from the relationship between energy and momentum: p = E/c). The kinetic energy portion is obtained by taking the sum of the momentum contribution of each electron in the unperturbed system ($\bar{p}_i$) and the modification of its momentum caused by the applied vector potential ($\bar{A}$).

The only perturbation component in equation 3 is contained in the kinetic energy term since the other terms involve only the residual electron-ion, electron-electron, and ion-ion interactions in the absence of an externally applied field. An expression for H'(r,t) can be realized by looking at the kinetic energy term of H. When the squaring operation is performed on this term, the $\bar{p}_i$ term is associated with H_0. The term containing $|\bar{A}|_2$ is dropped since we're only concerned with the linear response of the system to weak electric potential fields. Thus the perturbed and unperturbed portions of the Hamiltonian are determined as

$$H'(\bar{r}_i, t) = \frac{-e}{2mc} \sum_{i=1}^{N} \left[\bar{p}_i \cdot \bar{A}(\bar{r}_i, t) + \bar{A}(\bar{r}_i, t) \cdot \bar{p}_i \right] \tag{4a}$$

$$H_o = \frac{1}{2m}\sum_i \bar{P}_i^2 + \sum_i V_i(\bar{r}_i) + \frac{1}{2}\sum_{i,j}\frac{e^2}{|\bar{r}_i - \bar{r}_j|} + I \tag{4b}$$

The commutator, $[\bar{p},\bar{A}]$ is given by

$$\bar{P}\cdot\bar{A} - \bar{A}\cdot\bar{P} = -i\hbar\,\bar{\nabla}\cdot\bar{A} = 0 \tag{5}$$

since the vector potential polarization is transverse to the direction of travel. Therefore, the perturbed Hamiltonian can be written

$$H'(\bar{r},t) = \frac{-ie\hbar}{mc}\bar{A}\cdot\bar{\nabla} \tag{6}$$

Substituting equation (1) into equation (6) yields

$$H'(\bar{r},t) = \frac{-ie\hbar}{2mc}A\left[e^{i(\bar{q}\cdot\bar{r})} + e^{-i(\bar{q}\cdot\bar{r})}\right]e^{-\omega t}\,(\bar{a}_o\cdot\bar{\nabla}) \tag{7}$$

where the first and second terms are the expressions for the incident and reflected waves respectively.

We can write equations for electron energies in the conduction and valence bands using the energy vs wavelength diagram in Fig. 1. Here the zero of energy is taken at the bottom of the conduction band. For energies in the conduction band,

$$\mathcal{E}_c(\bar{k}'') = \hbar^2(k'')^2/2me \tag{8}$$

and for the valence band,

$$\mathcal{E}_v(\bar{k}') = -\mathcal{E}_g - \frac{\hbar^2(k')^2}{2m_h} \tag{9}$$

wher m_e and m_h are the effective masses for electrons and holes respectively.

In considering transitions from a state i in the valence band to a state j in the conduction band, the states are described by Bloch functions. The Bloch functions are

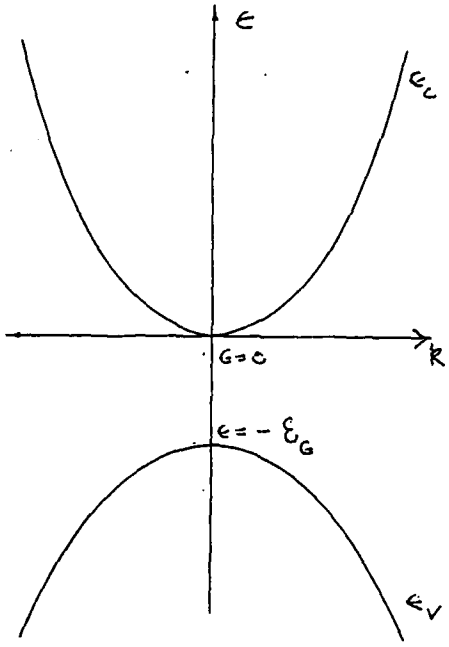

Figure 1. Energy band diagram for interband transitions (from Ref. 1).

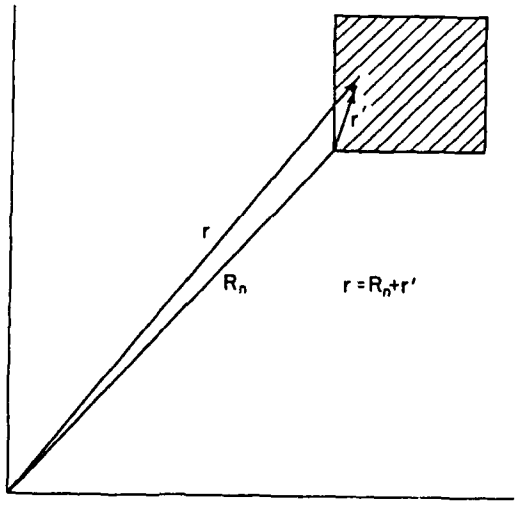

Figure 2. Position vectors for crystal lattice and unit cells (from Ref. 1).

solutions to the unperturbed Schrodinger equation, and encompass the periodicity of the lattice (4). They are written

$$\psi_i = \Omega^{-1/2} e^{i\bar{k}'\cdot\bar{r}} u_v(\bar{r},\bar{k}')$$

$$\psi_j = \Omega^{-1/2} e^{i\bar{k}''\cdot\bar{r}} u_c(\bar{r},\bar{k}'') \tag{10}$$

In order to obtain the transition rate, the perturbation elements of the optical matrix are determined. This is done by looking at the expectation value of the perturbation elements with respect to the Bloch states. Since we're only interested in absorption, the second term in equation (7) is omitted which produces the following for the perturbation elements:

$$H'_{ji}(\bar{r}) = \int \psi_j^* \left[H'(\bar{r})\right] \psi_i \, d\bar{r}$$

$$= \int \psi_j^* \left[-\frac{ie\hbar A}{2mc}(e^{i\bar{q}\cdot\bar{r}})\,\bar{a}_o\cdot\bar{\nabla}\right]\psi_i \, d\bar{r} \tag{11}$$

The periodicity of the functions u_v and u_c allows equation (11) to be expressed as the sum of integrals over the unit cells. This provides the following:

$$e^{[i(\bar{k}'+\bar{q}-\bar{k}'')\cdot\bar{r}]} = e^{i[(\bar{k}'+\bar{q}-\bar{k}'')\cdot(\bar{R}_n+\bar{r}')]} \tag{12}$$

This relationship is shown in Fig. 2 where the position vector, $\bar{r}$, is expressed as the vector sum of $\bar{R}_n$ (distance to the nth unit cell) and $\bar{r}'$(distance from the unit cell origin to a point in the unit cell). The perturbation matrix element then becomes

$$H'_{ji} = \sum_n e^{[i(\bar{k}'+\bar{q}-\bar{k}'')\cdot\bar{R}_n]} \int_{cell} f(\bar{r}', \bar{k}', \bar{k}'', \bar{q})\, d\bar{r} \tag{13}$$

The exponential argument in equation (13) varies rapidly and periodically. The H'_{ji} matrix elements will be very small unless (5)

$$\bar{k}' - \bar{k}'' + \bar{q} = 0 \tag{14}$$

which also serves as a statement of momentum conservation. Also, the wavelength of the incident light is much larger than the lattice vector length. Therefore, $\bar{q} \approx 0$, and

$$\bar{k}' = \bar{k}'' \tag{15}$$

This is the condition for direct interband transitions. Indirect optical transitions, where the electron changes momentum during the optical transition, are also possible. The change in momentum involves phonon assistance in the form of either phonon absorption or phonon emission. The significance of equation 15 is that direct optical transitions are far more likely to occur than indirect. By summing over all the unit cells, we can obtain the number of unit cells in the crystal, N_c:

$$\sum_n e^{[i(\bar{k}'+\bar{q}-\bar{k}'')\cdot\bar{R}_n]} = N_c \tag{16}$$

Taking V as the volume of a unit cell and Ω from equation (10) as the crystal volume, $N_c = \Omega/V$. H'_{ji} then becomes

$$H'_{ji} = \frac{-ie\hbar A}{2mcV} \int_{cell} u_c^*(\bar{k}')\left[\bar{a}_0\cdot\bar{\nabla} u_v(\bar{k}') + i\bar{a}_0\cdot\bar{k}' u_v(\bar{k}')\right] d\bar{r} \tag{17}$$

Here the second term in the integral is zero since Bloch functions are orthonormal (i.e. an electron cannot be in

the conduction and valence bands simultaneously).

Using the matrix elements of the momentum operator,

$$\bar{P}_{ji} = \frac{-i\hbar}{V} \int_{cell} u_c^* \bar{\nabla} u_v \, d\bar{r} \tag{18}$$

and placing this expression in the rewritten form of equation (17), the perturbation matrix elements for direct interband transitions become

$$H'_{ji} = \frac{-ie\hbar A}{2mcV} \int_{cell} u_c^* \bar{a}_0 \cdot \bar{\nabla} u_v \, d\bar{r} = \frac{eA}{2mc} \bar{a}_0 \cdot \bar{P}_{ji} \tag{19}$$

The transition rate for an electron from state ψ_i to ψ_j is (1)

$$W_{ji} = \frac{2\pi}{\hbar} |H'_{ji}|^2 \delta(\varepsilon_{ji} - \hbar\omega) = \left(\frac{\pi e^2 A^2}{2m^2c^2\hbar}\right) |\bar{a}_0 \cdot \bar{P}_{ji}|^2 \delta(\varepsilon_{ji} - \hbar\omega) \tag{20}$$

To determine the transition rate from the total number of conduction and valence band states, we must integrate equation (20) over all k-space

$$W_{cv} = \frac{\pi^2 e^2 A^2}{2m^2c^2\hbar} \int d\bar{k} \, |\bar{a}_0 \cdot \bar{P}_{ji}|^2 \delta(\varepsilon_{ji} - \hbar\omega) \tag{21}$$

We can apply the following general property of the δ function to equation (21):

$$\delta[g(x)] = \sum_n |g'(x_n)|^{-1} \delta(x - x_n) \tag{22}$$

This application produces:

$$\delta[\varepsilon_{ji}(\bar{k}) - \hbar\omega] = \sum_n [\delta(\bar{k} - \bar{k}_n) / |\nabla_k \varepsilon_{ji} \tag{23}$$

Substituting this relationship into equation (21) gives another form for the transition rate

$$W_{cv} = \frac{\pi^2 e^2 A^2}{2m^2c^2\hbar} \int d\bar{k} \sum_n \frac{|\bar{a}_0 \cdot \bar{P}_{ji}|^2 \delta(\bar{k} - \bar{k}_n)}{|\bar{\nabla}_k \varepsilon_{ji}(\bar{k})|} \tag{24}$$

where k_n represents all the k values satisfying $\varepsilon_{ji}(\bar{k}_n) = \hbar\omega$. These k values represent a surface in

k-space. We can alternately integrate over this surface with respect to a surface element dS:

$$W_{cv} = \frac{\pi^2 e^2 A^2}{2m^2c^2\hbar} \int |\bar{a}_0 \cdot \bar{P}_{ji}|^2 \frac{dS}{|\bar{\nabla}_k \mathcal{E}_{ji}(\bar{k})|} \tag{25}$$

An expression for the density of states, $\rho(\mathcal{E})$, can be derived using the following arguments. Consider two constant energy surfaces in k-space, one with energy $\mathcal{E}$ and the other with energy $\mathcal{E} + d\mathcal{E}$ as illustrated in Fig. 3. If a cylindrical volume element of surface area dS and height $k_\perp$ ($k_\perp$ is the perpendicular distance in k-space between the two surfaces) is used,

$$\rho(\mathcal{E}) = \int_{\bar{k}(\mathcal{E})}^{\bar{k}(\mathcal{E}+d\mathcal{E})} \rho(\bar{k})\, d\bar{k} = \int \rho(\bar{k})\, dS\, dk_\perp \tag{26}$$

since the density of states in k-space is $(4\pi^3)^{-1}$ per unit volume of crystal including spin. Also,

$$d\mathcal{E} = \bar{\nabla}_k \mathcal{E} \cdot dk = |\bar{\nabla}_k \mathcal{E}|\, dk_\perp \tag{27}$$

Therefore, the density of states may be written

$$\rho(\mathcal{E}) = \frac{1}{4\pi^3} \int \frac{dS}{|\bar{\nabla}_k \mathcal{E}|} \tag{28}$$

This expression can be substituted into equation (25) to obtain the joint density of states

$$\rho(\mathcal{E}_{ji}) = \frac{1}{4\pi^3} \int \frac{dS}{|\bar{\nabla}_k \mathcal{E}_{ji}|_{\mathcal{E}_{ji} = \hbar\omega}} \tag{29}$$

Here E_{ji} is the energy difference between two electron energy bands.

The points in k-space where $|\bar{\nabla}_k \mathcal{E}_{ji}| \to 0$ are known as critical points or van Hove singularities. Optical spectra will usually have structure at energies corresponding

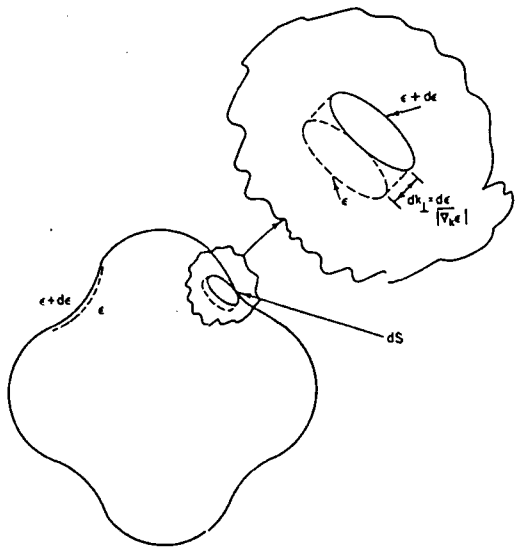

Figure 3. Constant energy surfaces in k-space with corresponding differential area element dS (from Ref.1).

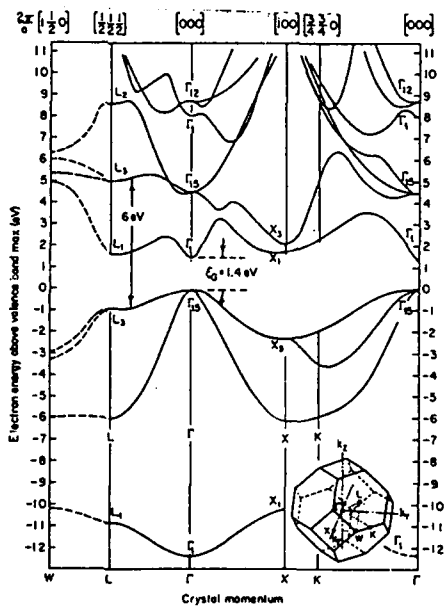

Figure 4. Energy band diagram for GaAs showing symmetry points and energy differences (from Ref. 1).

to these points. It is evident from equations (24) and (29) that the transition rate and hence the joint density of states are highest: 1) where the $\mathcal{E}_j$ and the $\mathcal{E}_i$ bands have the same slope, 2) when both $\mathcal{E}_i$ and $\mathcal{E}_j$ have a local maxima at the same point in the Brillouin zone, 3) when $\mathcal{E}_i$ and $\mathcal{E}_j$ have a simultaneous local minima, and 4) when a local maxima and minima occur at the same point in different bands. The structure may not necessarily be sharp due to background from other allowed transitions in the Brillouin zone with the same energy.

The energy band structure for GaAs is shown in Fig. 4. It is readily apparent that there are a number of possible transitions at optical energies. Also, moving from the direct gap position at the Γ point towards the L or X points there are regions where the valence and conduction bands are essentially parallel. Both the fundamental bandgap point, and these quasi-parallel band regions contribute to the optical spectrum.

Fig. 5 provides a more detailed view of the GaAs energy bands by labelling a number of critical points associated with prominent transition regions. These points can be detected with modulation spectroscopy. One such technique, electroreflectance, produces a first-order derivative of either the energy or the ϵ_2 portion of the dielectric function. The differentiation deletes the constant background spectrum and provides sharp features

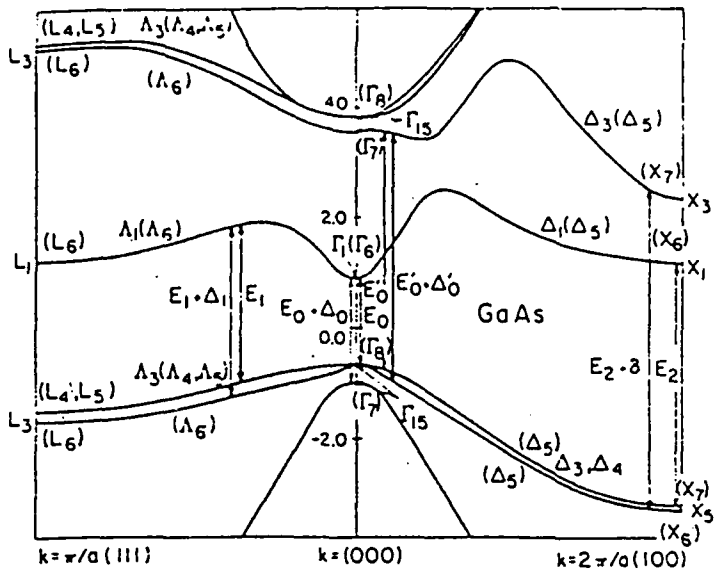

Figure 5. Energy band diagram for GaAs in the bandgap region showing critical points (from Ref. 6).

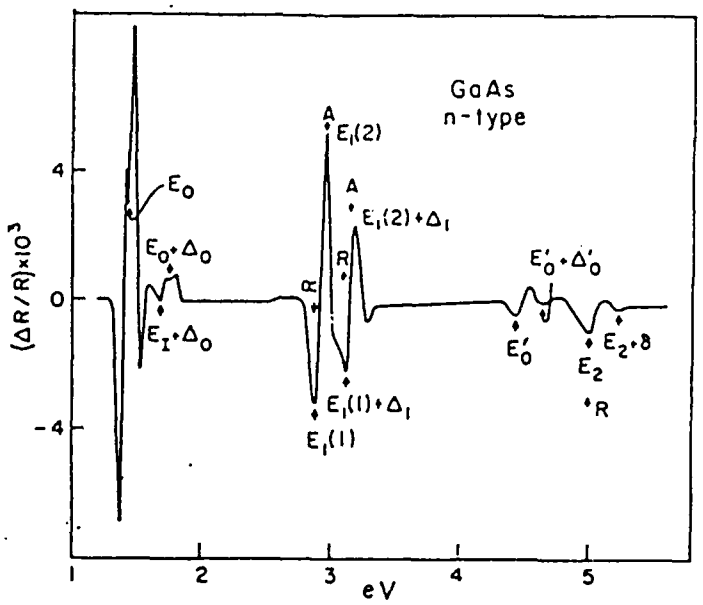

Figure 6. Electroreflectance spectrum for n-type GaAs (from Ref. 6).

corresponding to the critical points. An electroreflectance spectrum for n-type GaAs (10^{17} cm^{-3}) is illustrated in Fig. 6. Transitions occurring in the Γ point region are indicated by the E_0, $E_0 + \Delta_0$, E'_0 and $E'_0 + \Delta_0$ critical points. Symmetry points moving towards the L region from the zone center are denoted $E_1()$ and $E_1() + \Delta_1$. Critical transitions near the X point are labelled E_2 and $E_2 + \delta$.

References

1) F. Wooten, Optical Properties of Solids, Academic Press, New York, (1972).

2) K. Seeger, Semiconductor Physics, Springer-Verlag, (1985).

3) M. Cardona and E.J. Johnson, Semiconductors and Semimetals Vol. 3, Edited by: R.K. Willardson and A.C. Beer, Academic Press, New York, (1967).

4) J.S. Blakemore, Solid State Physics, Cambridge University Press, UK, (1985).

5) R.A. Smith, Semiconductors, Cambridge University Press, UK, (1978).

6) M. Cardona, K.L. Shaklee and F.H. Pollak, Phys. Rev. 154, 696, (1967).

F. MODFET and Multiple Quantum Well Energy Bands

The energy band bending and subband energy levels for both MODFETs and multiple quantum wells can be derived from quantum mechanical and classical considerations. The solutions to the physical picture presented by these two cases are complex. Therefore, approximations are made in each case. These approximations maintain the integrity of the physics involved and yield a quantitative solution to the problem. It should be noted that section 1. deals only with the energy vs. distance relationships (E vs. x) and that section 2. involves the dispersion relation of energy vs. momentum (E vs. k) to determine the allowed energy levels in the quantum wells.

1. MODFET Energy Bands (E vs. x)

Several types of theoretical models have been used to incorporate the quantum effects of the two dimensional electron gas into device modeling. Yoshida discusses four types of numerical models which have been developed to describe the electron distribution with respect to position (and hence the energy states) at the MODFET heterointerface (9):

1) Classical model in which the subband energy levels are neglected and Boltzmann statistics are used.
2) Classical model in which the subband energy levels are neglected and Fermi statistics are used.

3) Self-consistent quantum mechanical model including many body exchange and correlation effects with the local density- function approximation.

4) Quantum mechanical model using the triangular well approximation.

The most accurate method involves the self-consistent solution of Schrodinger's equation and Poisson's equation (method 3). All four methods produce results which differ by less than 10% for electron sheet concentrations of less than 1.5 X 10^{12} cm^{-2} (9). In this section, the spatial relationship for MODFET energy bands are determined using method 4. This method provides both the overall band bending and subband energies at the MODFET heterointerface as a function of position. The approach shown here is taken mainly from Landau and Lifshitz (4).

The band bending at an AlGaAs/GaAs interface is determined through Poisson's equation which relates the potential V(x) to the space charge density p(x) in the following manner:

$$\frac{d^2V(x)}{dx^2} = \frac{-P(x)}{\epsilon_1} \tag{1.1}$$

where ϵ_1 is the permittivity of GaAs. If it assumed that: 1) charge neutrality exists, 2) the doping concentrations are much greater than the intrinsic carrier concentrations 3) the bulk materials have zero charge density, and 4) the dopant density is uniform, then p(x) can be expressed (1)

$$P(x) = -q(N_{D1} - N_{A1}) - q\sum_{i=0}^{\infty} n_i \psi^2(x) \tag{1.2}$$

where the first term is due to the bulk GaAs and the second term reflects the charge density in the i quantized levels (ψ is the wave function and n is the charge density in the quantized region). Typically, the N_{A1} quantity is negligible (10^{14} cm^{-3}) in comparison with N_{D1} (10^{18} cm^{-3}). When only considering the bulk GaAs term, equation 1.1 has as it's solution (2)

$$V(x) = -q \frac{(N_{D1} - N_{A1})}{\epsilon_1} (x_1 - x)^2 \qquad (1.3)$$

where X_1 is the extent of the charge carrier density in the GaAs. Equation (1.3) certifies that the band bending in the bulk GaAs is parabolic.

Poisson's equation must be solved simultaneously with the Schrodinger equation in order to determine the energy subband structure of the system

$$\left[\frac{-\hbar^2}{2m} \frac{d^2}{dx^2} + V(x) \right] \psi(x) = E \psi(x) \qquad (1.4)$$

Figure 1 illustrates the potential energy scheme used for the MODFET. Here the quasi-triangular potential well approximation is used. This approach assumes that the electric field is constant in the region of the interface. The quantization takes place in a small region near the interface. Thus the AlGaAs potential barrier at x=0 is considered to be infinite with no wave function penetration into the region x < 0. V(x) is thus written (3,4)

$$V(x) = \begin{cases} \infty & ; x < 0 \\ q \frac{N_{D1}}{\epsilon_1} x = qFx & ; x > 0 \end{cases} \qquad (1.5)$$

where F is the electric field strength. If this approach

is not used, then an iterative, numerical method needs to be used to calculate the subbands. The associated boundary conditions for equation 1.5 are

$$1)\ \psi(x) \rightarrow 0\ ;\ x \rightarrow \infty$$

$$2)\ \psi(0) = 0 \tag{1.6}$$

In order to simplify the Schrodinger equation, a change of variable can be made

$$\frac{2mqF}{\hbar^2} x - \frac{2m}{\hbar^2} E = C\xi \tag{1.7}$$

where c is an arbitrary constant. Equation 4 can be re-written in the following manner

$$\left[\frac{d^2}{d\xi^2} - c^3\left(\frac{\hbar^2}{2mqF}\right)^2 \xi\right] = \psi(\xi) = 0 \tag{1.8}$$

Now (1.7) can be expressed as only a function of ξ

$$\left(\frac{d^2}{d\xi^2} - \xi\right)\psi(\xi) = 0 \quad \text{with} \quad C = \left(\frac{2mqF}{\hbar^2}\right)^{2/3} \tag{1.9}$$

ξ can also be written (this notation will be used later)

$$\xi = \left(\frac{2mqF}{\hbar^2}\right)^{1/3}\left(x - \frac{E}{qF}\right) = \frac{1}{a}\left(x - \frac{E}{qF}\right) \tag{1.10}$$

Equation (1.9) belongs to a group of differential equations solvable by LaPlace's method. This method applies to any linear equation of the form

$$\sum_{m=0}^{n} (a_m + b_m x)\ \frac{d^m y}{dx^m} = 0 \tag{1.11}$$

The general solution for (1.9) is expressed as

$$\psi(\xi) = K \int_c Z(t)\, e^{\xi t}\, dt \tag{1.12}$$

where K is a normalization constant. C is a complex integral with the path of integration taken so that the integral is finite and non-zero. Z(t) is given by

$$Z(t) = \frac{1}{Q}\, e^{\int (P/Q)\, dt} \tag{1.13}$$

and P(t) and Q(t) are

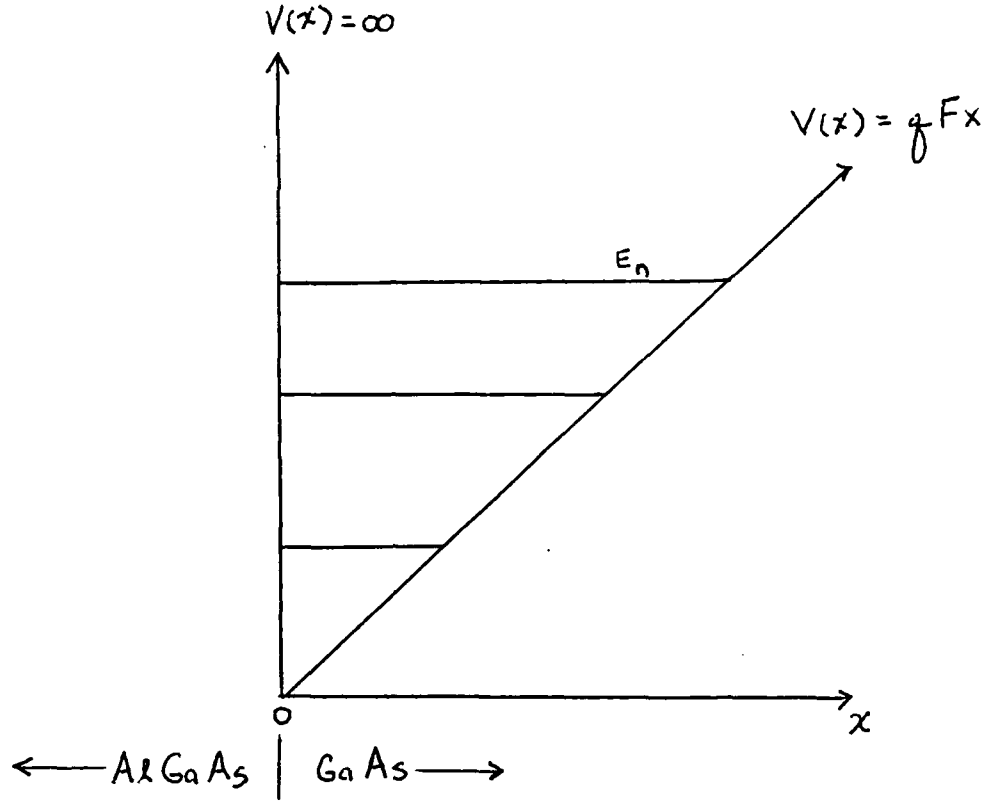

Figure 1. Potential energy diagram for the MODFET using the triangular potential well approximation.

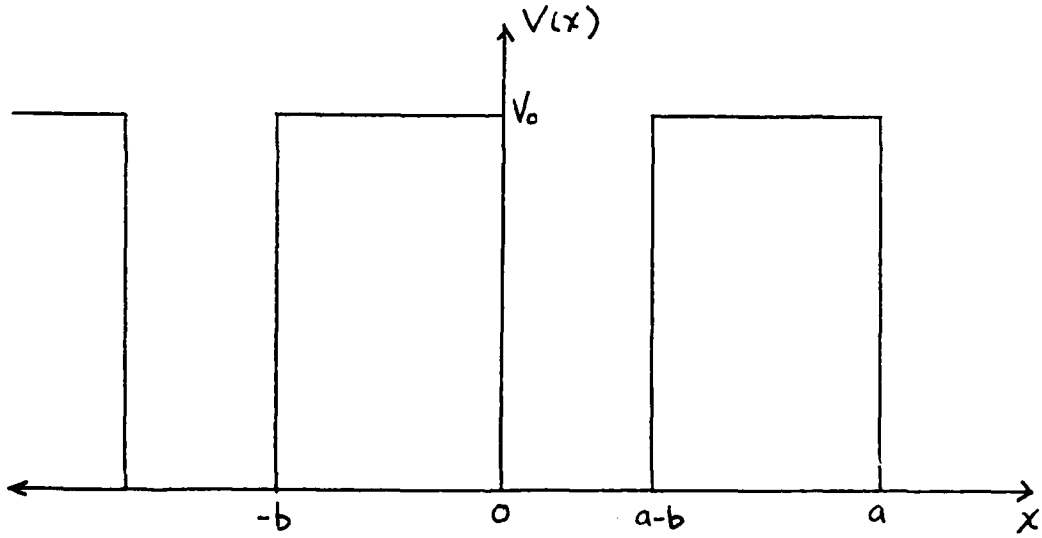

Figure 2. Potential energy diagram for the Kronig-Penney model.

$$P(t) = \sum_{m=0}^{n} a_m t^m \quad \text{and} \quad Q(t) = \sum_{m=0}^{n} b_m t^m \tag{1.14}$$

The coefficients of (1.11) are readily determined from (1.9). This yields $a_0 = a_1 = b_1 = b_2 = 0$, $a_2 = 1$ and $b_0 = -1$ which provides Q(t) and P(t)

$$Q_m(t) = Q_0(t) = b_0 t^0 = b_0 = -1$$

$$P_m(t) = P_2(t) = a_2 t^2 = t^2 \tag{1.15}$$

Now (1.12) is expressed

$$\psi(\xi) = -\int_C K e^{i(\xi t - t^3/3)}\, du \tag{1.16}$$

For the integral (and consequently ψ) to be bounded, the path of integration must be chosen so that the integrand is closed at both ends. By placing C along the imaginary axis (t = iu) the integrand is finite for all ξ. The wave equation thus becomes

$$\psi(\xi) = -K \int_{-\infty}^{\infty} i\, e^{i(u\xi + u^3/3)}\, du \tag{1.17}$$

which can be written as

$$\psi(\xi) = K\Phi(\xi) = \frac{-2i}{\sqrt{\pi}} \int_0^{\infty} \cos(\xi u + u^3/3)\, du \tag{1.18}$$

since the integral containing the sine term is zero (integral of an even function that is integrated symmetrically about the origin). $\Phi(\xi)$ in (1.18) with $K = -2i/(\pi)^{1/2}$ is an integral representation of an Airy function (the Airy function is further discussed in reference 10).

Substituting the second boundary condition in (1.6) into (1.18) yields

$$\xi\Big|_{x=0} = \left(\frac{2mqF}{\hbar^2}\right)^{1/3}\left(\frac{-E}{qF}\right) = \left(\frac{-2m}{\hbar^2 q^2 F^2}\right)^{1/3} E \tag{1.19}$$

from which

$$K\Phi\left(\left(\frac{-2m}{\hbar^2 q^2 F^2}\right)^{1/3} E\right) = 0 \tag{1.20}$$

ξ is now given a function energy. The zeros of the Airy function will satisfy the condition of (1.20). Therefore, E has a discrete spectrum. The roots of the Airy function are denoted: $0 < \alpha_1 < \alpha_2 < \ldots < \alpha_n$ (n = 1, 2, 3 ...). The quantized energies can thus be related to the roots of the Airy function by

$$\left(\frac{2m}{\hbar^2 q^2 F^2}\right)^{1/3} E_n = \alpha_n \tag{1.21}$$

or

$$E_n = \left(\frac{q^2 \hbar^2 F^2}{2m}\right) \alpha_n \tag{1.22}$$

The wave function can now be presented as a function of the roots and X

$$\Psi_n(x) = K\Phi(\xi_n) = K\Phi\left(\frac{x}{a} - \alpha_n\right) \text{ where } a = \left(\frac{\hbar^2}{2mqF}\right)^{1/3} \tag{1.23}$$

According to Ref (3), the Airy function can be approximated by

$$\Phi(\xi) \cong \frac{1}{|\xi|^{1/4}} \sin\left[\frac{2}{3}(\xi)^{3/2} + \frac{\pi}{4}\right] \tag{1.24}$$

This expression is zero when the sine's argument is $(n + 1)\pi$. Setting the argument in (1.24) equal to $(n + 1)\pi$ gives

$$\alpha_n = \left[\frac{3}{2}\left(n + \frac{3}{4}\right)\pi\right]^{2/3} \tag{1.25}$$

The discrete energy levels are now known:

$$E_n = \frac{q}{2}\left(\frac{q^2 \hbar^2 \pi^2}{m} F^2\right)\left(n + \frac{3}{4}\right)^{2/3} \tag{1.26}$$

Viewing this relationship, it appears that the spacing between energy levels would be most affected by the doping concentration N_{D1} since all other parameters are constant. Also, the higher the value of n, the closer spaced the

subband energy levels become due to the exponent in equation 1.26 being 2/3 ordered.

2. Multiple Quantum Well and Superlattice Energy Bands (E vs. k)

There are at least three main approaches for the determination of MQW and superlattice energy band levels. These models produce solutions based upon the solution of Schrodinger's equation for the MQW. The superlattice can then be viewed as a MQW with a relatively thin potential energy barrier. The three approaches are:

1) The Envelope Function Approximation (EFA)
2) The Tight Binding Approximation (TBA)
3) The Kronig-Penney Model

A complete presentation of these methods would be quite voluminous. General comparisons between the different approaches are made in this section. The Kronig-Penney Model is derived here because more complex models are not necessary to illustrate the properties of MQW structures.

In the EFA the wave function of a superlattice or a MQW is expressed as a linear combination of Brillouin zone-center bulk states with a slowly varying envelope modification along the superlattice axis (perpendicular to the heterointerface) (5,7). The EFA has been found to be in overall agreement with experiments (6). In these experiments, comparisons between theoretical and measured

The coefficients of the wavefunction are determined by diagonalizing the matrix elements of the Hamiltonian matrix until the eigenvalues correspond to the state originally assumed.

The TBA has been found to be in good agreement with the Kronig-Penney model for the heavy hole valence band states near the zone center (5). Here the valence band heavy hole states are nearly parabolic (a condition associated with the Kronig-Penney model). Calculations involving both the TBA and the Kronig-Penney model disagree by less than a millielectron-volt for heavy hole energies from the valence band maximum to -0.26 eV below that point. The agreement between the two methods fails for light hole and conduction band states due to band non-parabolicity and the fact that the Kronig-Penney model fails to account for band mixing (as does the EFA).

The Kronig-Penney model will now be discussed. The potential energy band vs. position for the MQW is shown in Fig. 2. The barrier potential is V_0 and the barrier and well thicknesses are b and a - b respectively. Here the band bending is not shown since it considered to be only a small part of the total band structure. In the physical sense, the AlGaAs and GaAs layers are thin enough that the band bending is small over the distance concerned. This is unlike the MODFET case where the GaAs is unbounded on one side.

In this case energies with $E < V_0$ are considered in order to determine energy quantization within the well. The approach is to solve the Schrodinger equation separately in the $V(x) = 0$ and the $V(x) = V_0$ regions and apply the boundary conditions for continuity. The Schrodinger equation and its associated solution for each region are given by (8)

$\underline{V = 0}$ $$\psi_0''(x) = \frac{2m}{\hbar^2} E\psi_0(x) = 0 \tag{2.1}$$

$$\psi_0(x) = Ae^{i\beta x} + Be^{-i\beta x} \quad ; \quad \beta = \frac{(2mE)^{1/2}}{\hbar^2} \tag{2.2}$$

$\underline{V = V_0}$ $$\psi_V''(x) - \frac{2m}{\hbar^2}(V_0 - E)\psi_V(x) = 0 \tag{2.3}$$

$$\psi_V(x) = Ce^{\alpha x} + De^{-\alpha x} \quad ; \quad \alpha = \frac{[2m(V_0 - E)]^{1/2}}{\hbar^2} \tag{2.4}$$

The first two boundary conditions are established with respect to the Schrodinger equation

$$1)\ \psi_0(0) = \psi_V(0) \qquad \text{and } 2)\ \left.\frac{d\psi_0}{dx}\right|_{x=0} = \left.\frac{d\psi_V}{dx}\right|_{x=0} \tag{2.5}$$

The other two boundary conditions are based upon the periodicity of the potential.

$$3)\ \psi_V(-b) = e^{-ika}\psi_0(a-b) \qquad \text{and } 4)\ \left.\frac{d\psi_V}{dx}\right|_{x=-b} = e^{-ika}\left.\frac{d\psi_0}{dx}\right|_{x=a-b} \tag{2.6}$$

Applying the four boundary conditions

$$1)\ A + B = C + D \tag{2.7}$$

$$2)\ i\beta(A - B) = \alpha(C - D) \tag{2.8}$$

$$3)\ Ce^{-\alpha b} + De^{\alpha b} = e^{-ika}\left[Ae^{i\beta(a-b)} + Be^{-i\beta(a-b)}\right] \tag{2.9}$$

$$4)\ C\alpha e^{-\alpha b} - D\alpha e^{\alpha b} = e^{-ika}\, i\beta\left[Ae^{i\beta(a-b)} - Be^{-i\beta(a-b)}\right] \tag{2.10}$$

These four simultaneous equations can be solved by setting the determinants of the coefficients of A, B, C and D to zero. This produces the following transcendental equation

$$\cos ka = \frac{\alpha^2 - \beta^2}{2\alpha\beta}\sinh(\alpha\beta)\sin\beta(a-b) + \cosh(\alpha b)\cos[\beta(a-b)] \tag{2.11}$$

Since k is a real constant, the right hand side of the above equation must lie between 1 and -1. The allowed energy values are those which cause the right hand side to be within this range.

The above relationship can be mathematically simplified and more easily represented by applying further approximations to the Kronig-Penney model. This model imposes the restriction

$$P = \left(\frac{ma}{\hbar^2}\right) b V_0 \equiv \text{constant} \tag{2.12}$$

If a delta function approximation is used, the barrier width, $b \rightarrow 0$ and barrier height, $V_0 \rightarrow \infty$, and the range of quantized energy levels are easily found. Applying these simplifying conditions, $(V_0 - E) \rightarrow V_0$, $\sinh\alpha b \rightarrow \alpha b$ and $\cosh\alpha b \rightarrow 1$. In this case, (2.11) is written

$$\cos ka = \frac{P}{\beta a} \sin(\beta a) + \cos(\beta a) \tag{2.13}$$

A plot of the right hand side of (2.13) as a function of βa is shown in Fig. 3. It is readily seen that with increasing P the energy gaps between the allowed energy ranges become smaller. Thus the quantized energy levels become more discrete. This is qualitatively the case in the superlattice and multiple quantum well. For a particular AlGaAs composition the value of V_0 in (2.12) will remain constant, therefore P can be increased by maintaining the well width constant and varying the barrier width. Thus, small values of P are representative of the superlattice case (with the associated "spreading" of the

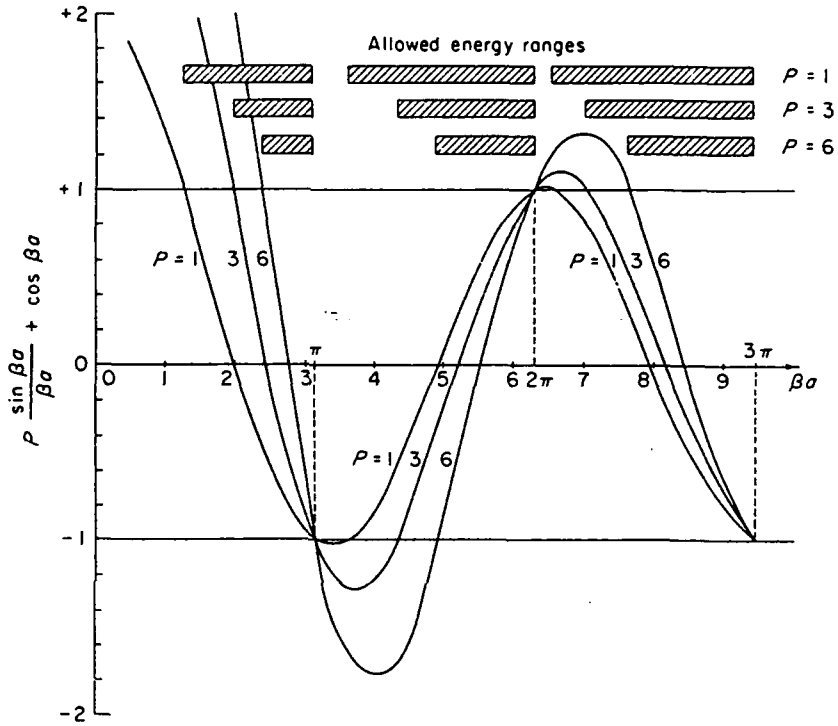

Figure 3. Allowed energy ranges for a multiple quantum well using the Kronig-Penney model with a varying P parameter (from Ref. 5).

discrete energy bands) and larger values of P are indicative of the multiple quantum well.

References

1) T.J. Drummond, W.T. Masselink and H. Morkoc, Proc. of the IEEE **74**, 773, (1986).

2) G.W. Neudeck, Modular Series on Solid State Devices Vol. II, Addison-Wesley Publishing Co., (1983).

3) Problems in Quantum Mechanics, Edited by: D. ter Haar, Pion Ltd., London, UK, (1975).

4) L.D. Landau and L.M. Lifshitz, Quantum Mechanics (Non-relativistic Theory), Pergamon, Oxford, UK, (1965).

5) J.N. Schulman and Y. Chang, Phys. Rev. B **31**, 2056, (1985).

6) M. Altarelli, in Heterojunction and Semiconductor Superlattices, edited by G. Allan, et. al., Springer-Verlag, (1986).

7) G. Bastard, in Molecular Beam Epitaxy and Heterostructures, edited by L.L. Chang and K. Ploog, Martinus Nijhoff Publishers, (1985).

8) R.H. Bube, Electrons in Solids, Academic Press, New York, (1981).

9) Hiroshida, IEEE Trans. Elect. Dev. **ED-33**, 154, (1986).

10) Liboff, R.L., Introductory Quantum Mechanics, Addison-Wesley Publishing Co., 1980.

Chapter 3.

VASE Studies of GaAs/AlGaAs Heterostructures

A. Preliminary Comments

Esssential to this are an explanations concerning: 1) how the angle of incidence is selected, and 2) the availability of samples for analysis. The explanation of ϕ selection is presented now to prevent repetition since this procedure is done prior to each study. Also, it is important to consider the process of sample procurement and how this affects the research effort.

Selecting the Angle of Incidence

The sensitivity of ellipsometric measurements is a strong function of ϕ, with maximum sensitivity occurring at the wavelength-dependent, principal (pseudo-Brewster) angle (1,2). At the principal angle, suppression of either the p or the s component of the wave reflected from the sample occurs. VASE allows measurement at several angles close to the principal angle, as opposed to spectroscopic ellipsometry (SE), in which measurements are made at a fixed, single value of ϕ.

The principal angle can be estimated prior to measurement by modeling the assumed structure for the sample and generating three-dimensional plots of ψ or Δ vs. wavelength and ϕ. The 3-D plots for ψ and Δ for the structure used in the interfacial roughness study are shown in Figs. 1 and 2 respectively. Two particularly inaccurate measurement regions occur at ψ near 0° and Δ near 180°. Reproducibility of measurements in these regions have

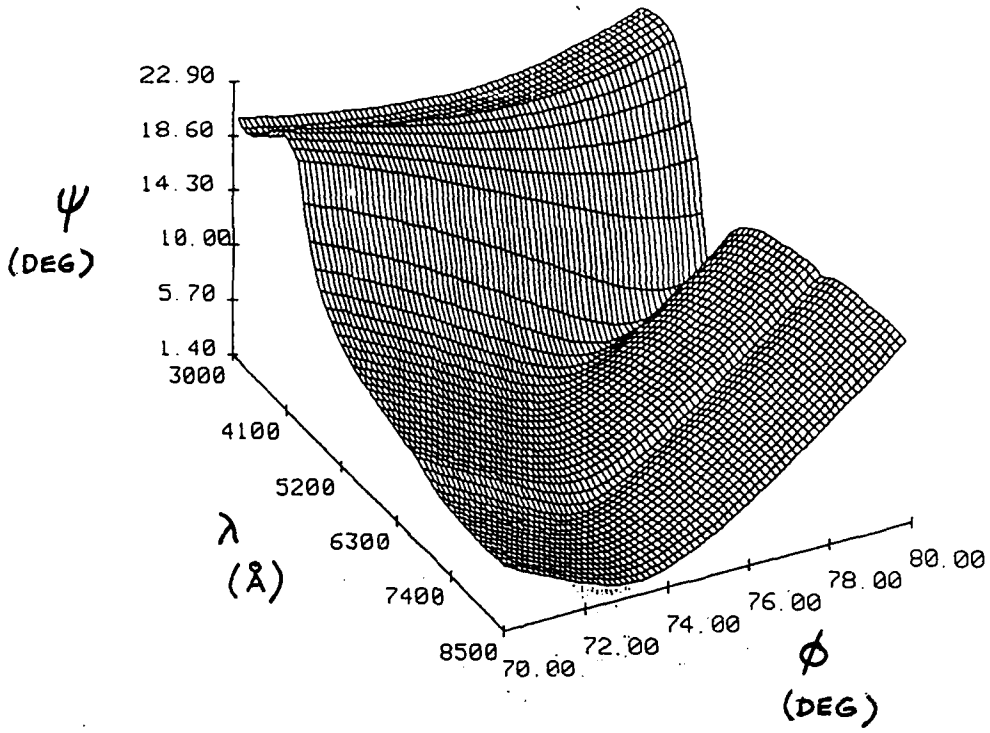

Figure 1. 3-D plot of ψ for the GaAs/AlGaAs structure shown.

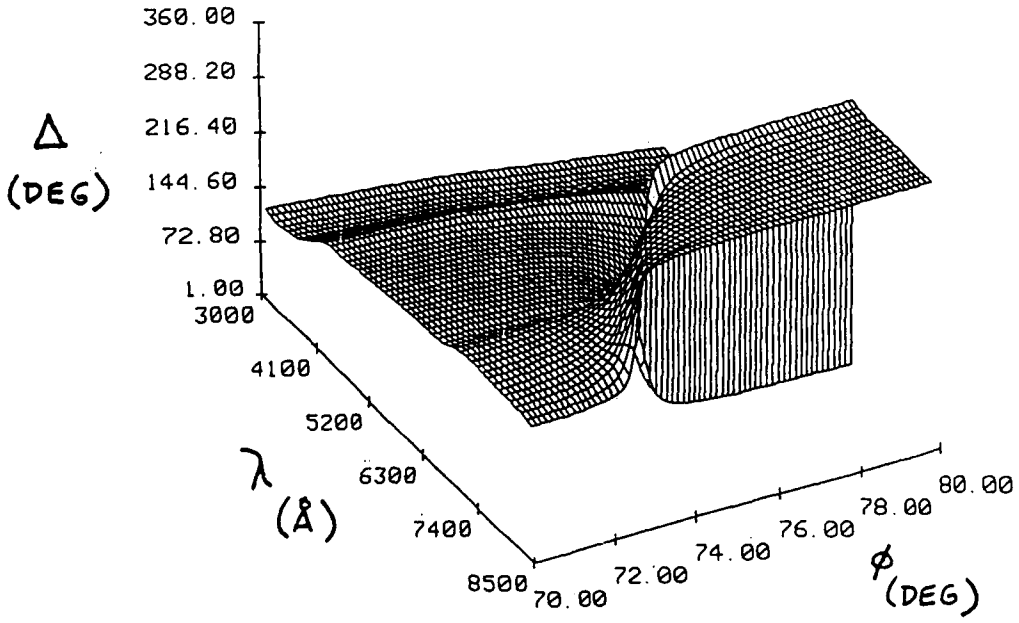

Figure 2. 3-D plot of Δ for the same structure.

been poor with Δ varying by as much as 5 . The ψ plot in this case reveals that there is a region of the spectrum from 6300 A to 8500 A where ψ is close to 0°. Therefore, measurements where ϕ is less than 73° would not be advisable. In the Δ plot a handedness change in the polarization ellipse is seen for $\phi > 76^\circ$. This handedness change causes difficulties in the data fitting procedure and hence values of $\phi > 76^\circ$ should possibly be avoided.

The effect on the ψ and Δ spectrum of changes in layer thickness and composition is revealed through 3-D sensitivity plots. These plots contain the difference (in ψ or Δ) between a sample containing reference parameters and a sample with perturbed parameters. A sensitivity plot of $\delta\psi$ is shown in Fig 3. In this case the roughness content of the GaAs layer in the sample shown has been changed from 10 A to 20 A. The sensitivity of ψ to this change is determined by subtracting the 20 A ψ spectrum from the 10 A ψ spectrum. From the figure it is evident that ψ would be sensitive to a 10 A increase in the GaAs layer roughness at $\phi = 75^\circ$. Thus for this sample $\phi = 75^\circ$ appears to be an appropriate measurement angle when considering roughness sensitivity, handedness change, and accuracy.

Obtaining Samples

The VASE method is a valuable diagnostic tool for semiconductor growth processes. Currently the RHEED (re-

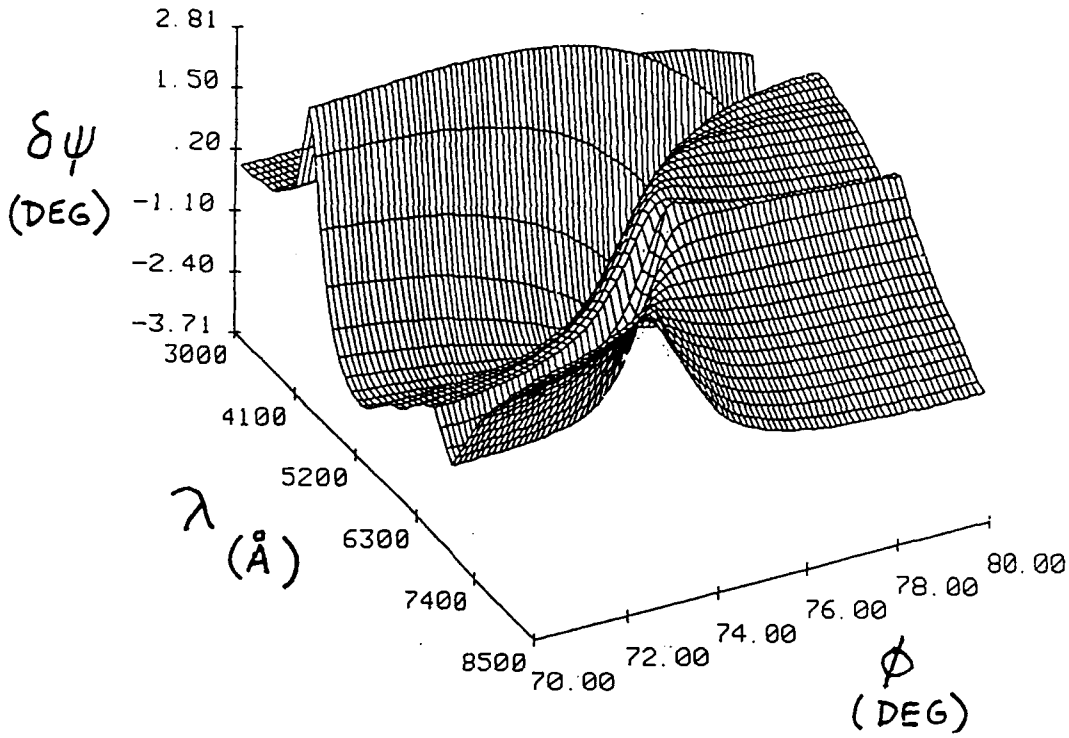

25 Å GaAs Ox	
40 Å GaAs	
10 Å GaAs/AlGaAs	
300 Å $Al_{0.3}Ga_{0.7}As$	
Buffer + Substrate	

−

25 Å GaAs Ox
30 Å GaAs
20 Å GaAs/AlGaAs
300 Å $Al_{0.3}Ga_{0.7}As$
Buffer + Substrate

Figure 3. A 3-D plot showing the sensitivity of ψ to a change in roughness layer thickness.

flection high energy electron diffraction) process is the most popular in-situ growth monitoring technique for MBE grown materials. VASE is a possible replacement for RHEED because VASE can provide additional information such as optical constants and alloy composition as well as detect monolayer growth. Increasing interest in VASE measurements is manifesting itself in inquiries from growth facilities at Perkin-Elmer Corp., Honeywell Corp., University of Illinois, Varian Corp., and the Avionics Laboratory at Wright-Patterson AFB to name a few.

Much of the demand for VASE resulted from professional publication and offers of collaborational studies by the UNL laboratory. All of the samples used in this effort were obtained from Dr. S. A. Alterovitz at NASA Lewis Research Center who procured them under NASA a grant from D.C. Radulescu and L.F. Eastman at Cornell University.

References

1. R.M.A. Azzam and N.M. Bashara, Ellipsometry and Polarized Light, North-Holland Publishing, New York, N.Y., (1977).

2. P.G. Snyder, M.C. Rost, G.H. Bu-Abbud, J.A. Woollam and S.A. Alterovitz, J. Appl. Physics **60** (9), 3293 (1986).

3. D.C. Radulescu, G.W. Wicks, W.J. Schaff, A.R. Calawa, and L.F. Eastman, J. Appl. Phys. **62**, 954, (1987).

B. Wafer Homogeneity Study

INTRODUCTION

Crucial to the development of heterostructure ICs and opto-electronic devices is the ability to grow GaAs/AlGaAs layers of high quality and uniformity. Layer thickness variations across a wafer will have a profound effect on threshold voltage in MODFET IC devices. The abruptness of interfacial regions determines the suitability of the wafer for the production of semiconductor lasers. Therefore a requirement exists for the determination of layer homogeneity and interfacial properties. In this study VASE is used to address these important considerations.

A layered sample (originally grown at Cornell University, labeled #1723) produced for the later development of MODFET devices was studied. The epitaxial layers were grown by MBE on a liquid encapsulated Czochralski (LEC) semi-insulating substrate. The high quality of the material used in this structure is demonstrated by the 77K electron mobility of 1.7×10^5 cm^2/V sec with a 2DEG sheet carrier density of 3×10^{11} cm^{-2}. The sample used for this study had 2.5 by 1.0 cm length and width dimensions.

The structure is illustrated in Fig. 1. A 1 um undoped GaAs buffer layer was grown on top of the substrate followed by a 200 A undoped $Al_{0.3}Ga_{0.7}As$ spacer layer (part of thickness t_1). The planar junction of these

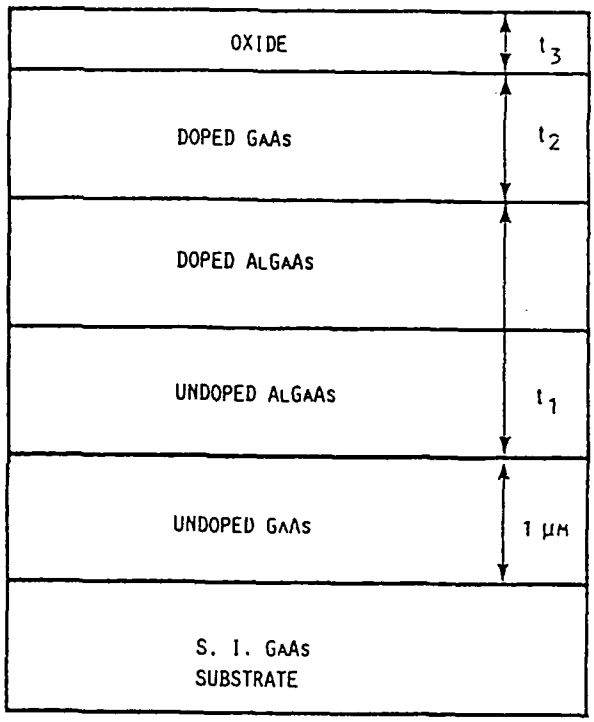

FIGURE 1.

Figure 1. VASE model for GaAs/AlGaAs sample #1723.

two layers forms a MODFET heterointerface. Next, a 300 A n^+ doped layer of $Al_{0.3}Ga_{0.7}As$ was deposited in order to provide carrier electrons to the heterojunction. A 300 A n^+ GaAs cap was the last layer grown.

EXPERIMENTAL

In order to obtain good sensitivity in the ellipsometric measurements, p-wave suppression was used. Thus measurements were taken at the principal angle where Δ is 90° over most of the spectrum. A He-Ne laser (6328 A) was used for alignment and setting the angle of incidence to obatin $\Delta = 90^\circ$. This sample was measured at two angles (75.5° and 76.5°) near the principal angle. The thickness of the buffer layer was not measured since it is farther from the surface than the penetration depth of the light. Also, the 200 A AlGaAs spacer layer and the 300 A doped AlGaAs layer were modeled as a single, 500 A layer of AlGaAs since the inversion analysis isn't sensitive to doping parameters. Analysis of other samples by this research group has yielded information about layer doping through the Franz-Keldysh effect (1,2).

The sample was aligned with the long axis perpendicular to the plane of incidence. The beam spot on the sample is ellipsoidal with approximately a 1 mm short axis and a 4 mm long axis. Measurements were made at three positions on the sample. Spot 1 is near the point that was originally the center of the 2-inch wafer, spot 2

is in the center of the sample and spot 3 was located near the rounded edge of the wafer. No chemical treatment or rinsing of the sample (in order to remove surface oxides and hydrocarbons) was performed prior to measurement.

The spectroscopic measurements were taken in the 3500 to 8000 A wavelength range in 50 A steps. The near infrared points were much noisier than the others, as both the Xe lamp light output and the multialkali photomultiplier efficiency are lower in this range. In addition the values of Δ above 7400 A are rather low ($< 30^{\circ}$). This means that ϕ is not close to the principal angle in this wavelength range. Therefore, the Δ data in this range are not very sensitive to the model parameters of interest.

RESULTS

The experimental results of the ellipsometric parameters ψ and Δ at the three spots are given in Figs. 2a and 2b respectively. The main feature of Fig. 2 is that the results for spots 1 and 2 are identical over the whole wavelength range, and that the difference of spot 3 spectrum is small. This exhibits the high degree of homogeneity across this sample.

A least squares analysis was tried, using both ψ and Δ over the entire 3500 to 8000 A range, to obtain the thicknesses and x. However, the program did not converge to a meaningful result with respect to MSE or model

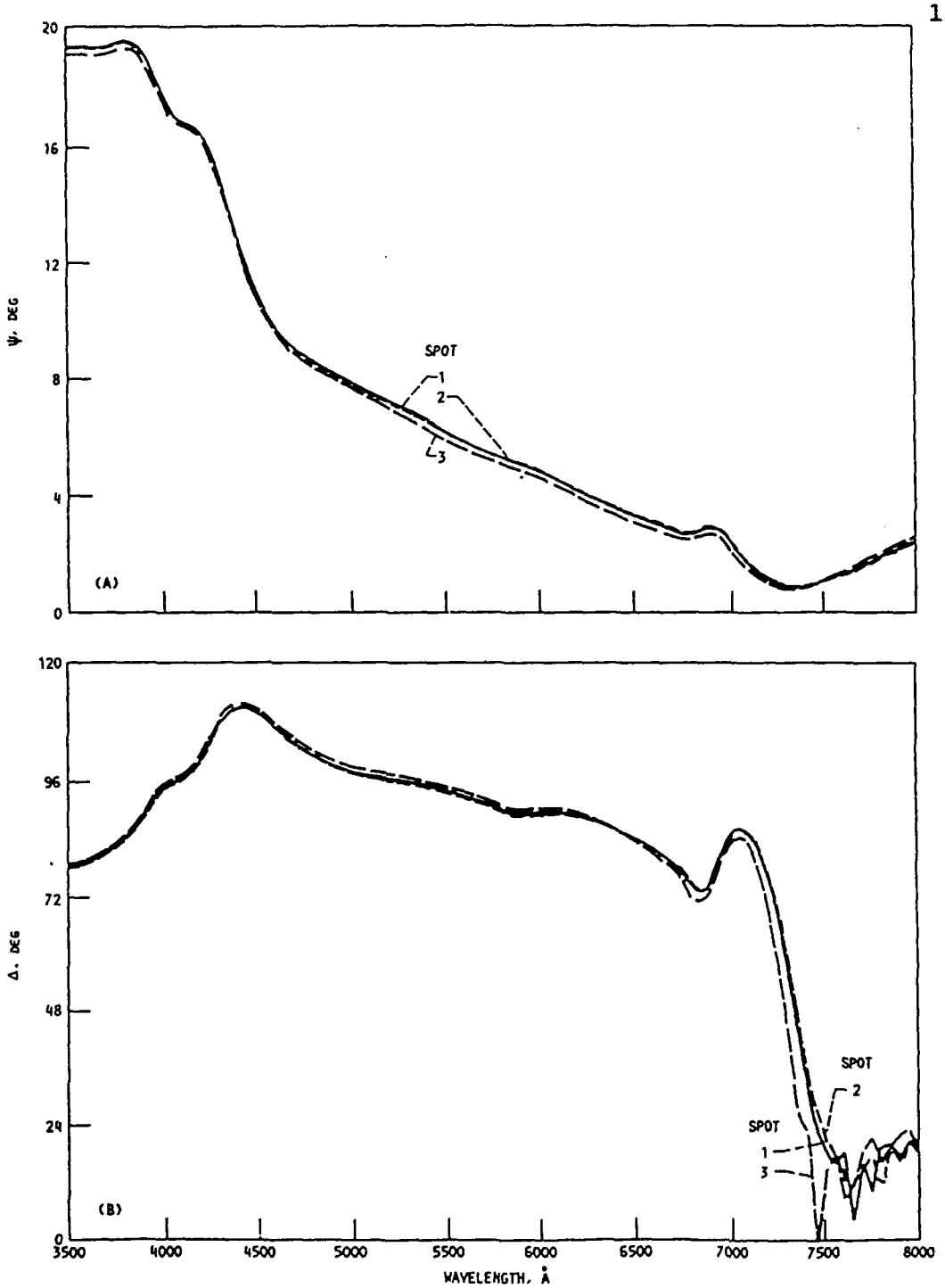

Figure 2. Experimental results of the ellipsometric parameters for the three spots measured. a) ψ results. b) Δ results.

parameters. As the experimental results for ψ and Δ above 7400 A (especially Δ), have a much higher error than the lower wavelength results, the ψ and Δ fits were restricted to the range 3500 to 7300 A. The results obtained by the inversion in this case are presented in the first three rows of Table I. Plots of the calculated and experimental ψ and Δ versus wavelength are shown in Fig. 3. The MSE is larger than the results published in a previous research effort using GaAs/AlGaAs heterostructures (3). The main reason is the difference in structures. Here we have a partially doped AlGaAs layer, while in (3) the AlGaAs was undoped. As a result, the Franz-Keldysh effect is more prominent in the present case and should be accounted for explicitly in the structure model in order to obtain the best possible MSE and data fits. For simplicity, these extra parameters were not included, as the main objective is the comparison of a couple of spots, not an absolute characterization of the material. As a result of the large MSE, the 90 % confidence limits are rather large. For example, the confidence limits for spot 2 are: +/- 83 A for t_1, +/- 51 A for t_2, +/- 11 A for t_3, and +/- 0.02 for x. Another factor contributing to the large confidence limits of t_1 and t_2 is the high correlation (~ 0.965) between the two layers which was determined during analysis. It should be noted that the bulk values of the dielectric constants $\epsilon_1(\lambda)$ and $\epsilon_2(\lambda)$ were used in the inversion

analysis.

The results for the thickness and the Al concentration x from Table I show remarkable consistency with the RHEED values (nominal values in Table I) obtained during MBE growth, especially for the AlGaAs thickness. Also observable is the excellent homogeneity obtained, with none of the estimated parameters changing by even 1 % of their value at the center of the sample. However, the large MSE values can give the appearance of an inaccurate comparison between the three spots. Therefore, another inversion was made using only the ψ experimental results. As the ψ parameter is less affected by the Franz-Keldysh effect than Δ, the entire experimental range 3500 to 8000 A was used. The results of this inversion are given in rows four to six of Table I. A comparison of the experimental and calculated ψ results for the central spot is illustrated in Fig. 4a. For completeness, Δ versus wavelength was was calculated using the parameters of Table I (row five) and the result is displayed in Fig. 4b. There is a negative Δ range in Fig. 4b (above 7600 A), shown as Δ near 360°. The major conclusion from Figs. 4a and 4b is that the discrepancy between the calculated and experimental values of both ψ and Δ is rather large at the AlGaAs bandgap, i.e. where the Franz-Keldysh effect is very important. This ψ-only inversion reinforces the correctness of the thickness and composition values obtained from the data

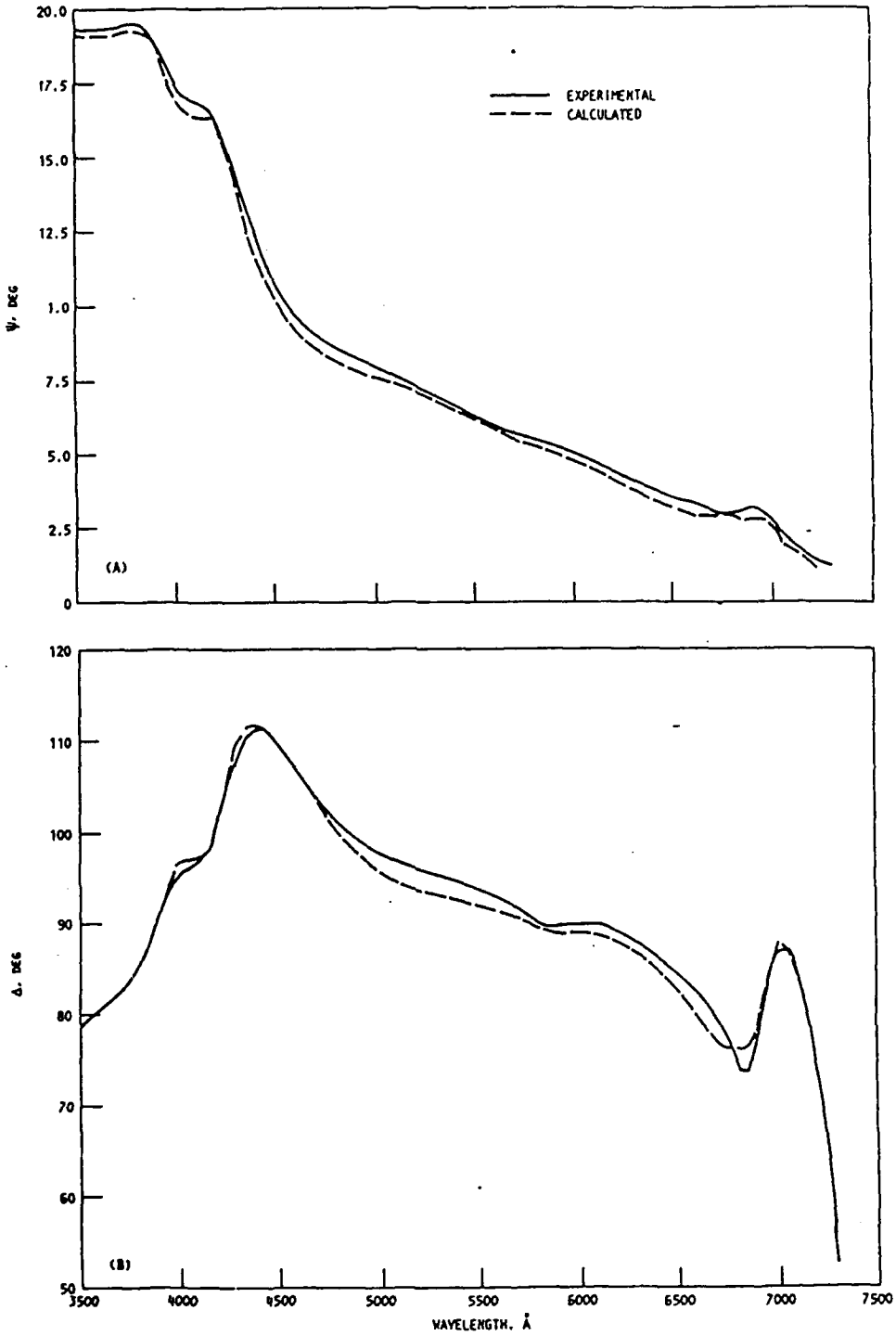

Figure 3. Experimental and theoretical fits using the ellipsometric parameters measured at spot 2. a) ψ results. b) Δ results.

Table I. Results of the Inversion Analysis for Sample #1723 (all wavelengths and thicknesses are in A).

Spot #	MSE Type	λ Range	X	t_1	t_2	t_3	MSE
1	ψ,Δ	3500-7300	0.280	504	328	32.9	1.089
2	ψ,Δ	3500-7300	0.279	507	328	33.0	0.988
3	ψ,Δ	3500-7300	0.277	499	325	31.4	1.282
1	ψ	3500-8000	0.265	506	320	36.9	.0155
2	ψ	3500-8000	0.264	509	321	36.8	.0156
3	ψ	3500-8000	0.265	502	317	34.4	.0156
Nominal	****	*****	0.3	500	300	25.0	****

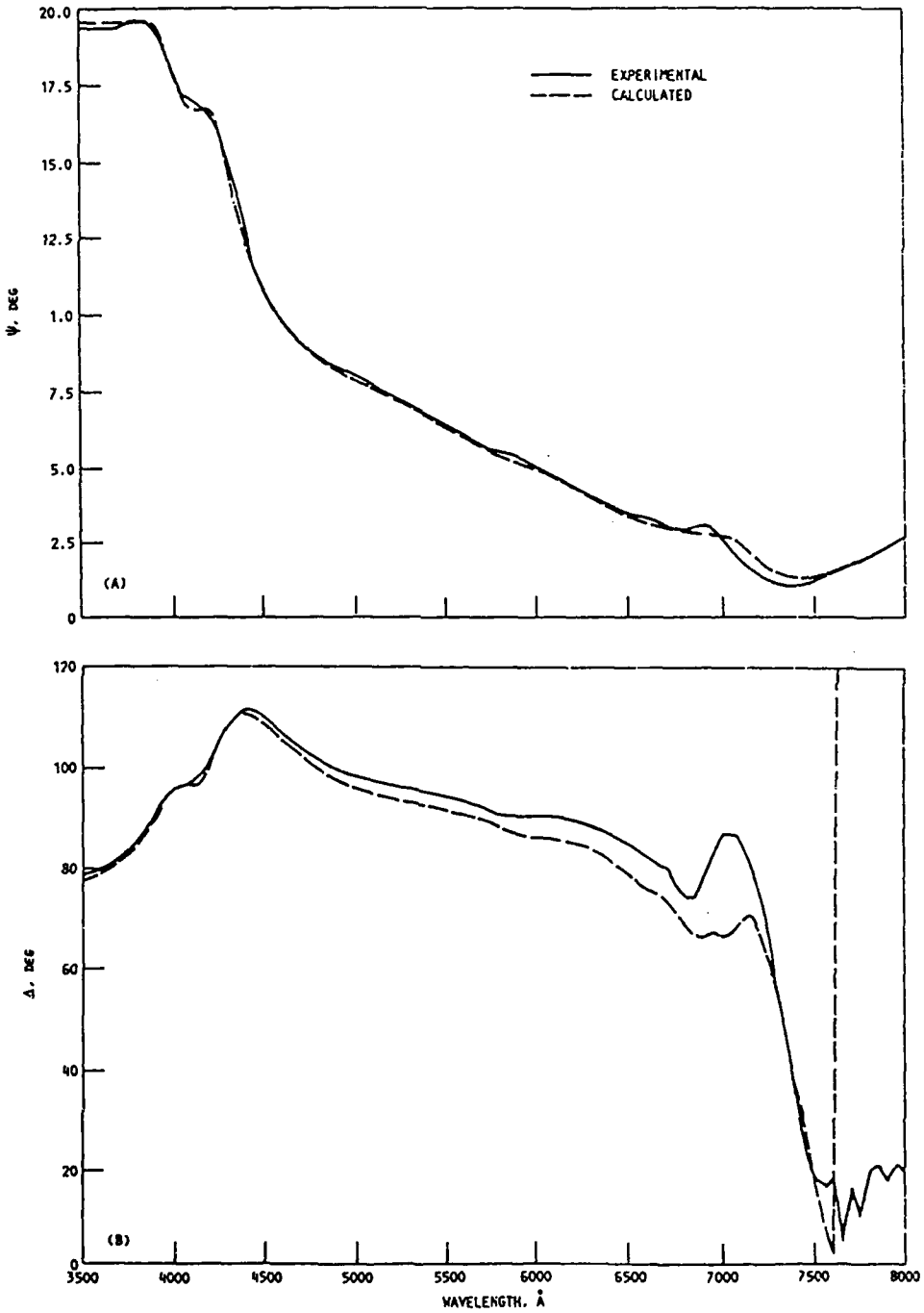

Figure 4. Experimental and theoretical results using only the ψ parameter at spot 2. a) ψ results. b) Δ results.

fits where ψ and Δ were used simultaneously. The correlation between the various parameters is now negligible, as it does not exceed 0.9. The new 90% confidence limits for the central spot are: +/- 59 A for t_1, +/- 27 A for t_2, +/- 8 A for t_3, and +/- 0.046 for x. The absolute value of the parameters is now different, but the comparison among the three spots show exactly the same features as the ψ and Δ inversions: x is constant, the AlGaAs thickness in the center is highest, and the Gaas thickness at spot 3 is 1 % below the other two spots. It can be concluded that the comparison of thicknesses and Al concentrations among the spots can be made on a scale that is one order of magnitude better than the 90% confidence limits, provided the structures are almost identical. This result is crucial for any future three-dimensional plots of thicknesses and Al concentrations at various spots on the same wafer.

References

1. P.G. Snyder, J.E. Oh, and J.A. Woollam, Materials Research Society Symposium Proc. 77, 761, (1987).

2. P.G. Snyder, K.G. Merkel, and J.A. Woollam, accepted for publication in SPIE vol. 946 "Advances in Semiconductors and Superconductors: Physics and Device Applications, (1988).

3. P.G. Snyder, M.C. Rost, G.H. Bu-Abbud, J.A. Woollam, and S.A. Alterovitz, J. Appl. Phys. **60**, 3293, (1986).

C. Characterization of GaAs/AlGaAs Superlattices

INTRODUCTION

The main purpose of this study was to determine the ability of VASE to measure the physical and optical properties of GaAs/AlGaAs superlattices. These superlattice samples were grown by Cornell University for later formation of MODFET integrated circuits. Along with the determination of layer thicknesses and composition the resolution of excitonic transitions was a primary consideration.

The observation of excitonic effects in superlattices at room temperature greatly enhances the suitability of their use with other opto-electronic devices (1). VASE provides important information about these devices, specifically the index of refraction and extinction coefficient at excitonic transition energies in superlattices (2). VASE is advantageous in that both the real and imaginary parts of the dielectric function and the refractive index are readily measured without the use of a Kramers-Kronig analysis.

For the two samples used in this study, measurements were made at $\phi = 75.5^\circ$ and 76.5° (for sample #2207), and at $\phi = 76^\circ$ (for sample #2352) which are very near the principal angles over most of the spectral range. The data for these experiments were taken in the 3500 to 8000 A spectral range in increments of 25 A.

The nominal structure of the two measured samples is

400, 300 Å GaAs	
325Å $Al_{0.3}Ga_{0.7}As$	
SI Planar Layer 6E12 cm^{-2}	
75Å $Al_{0.3}Ga_{0.7}As$	
150Å GaAs	
200Å $Al_{0.3}Ga_{0.7}As$	25/24 Periods
20, 30 Å GaAs	
GaAs Substrate	

Figure 1. Superlattice structure for samples #2352, #2207.

25 Å Oxide
400 Å GaAs
400 Å $Al_{0.3}Ga_{0.7}As$
150 Å GaAs
5500 Å $Al_{0.3}Ga_{0.7}As$
GaAs Substrate

Figure 2a. VASE model for sample #2352.

shown in Fig. 1. The layers were grown by molecular beam epitaxy in a Varian II machine on an undoped liquid encapsulated Czochralski (LEC) GaAs substrate (3). The substrate was rotated at 7 rpm during deposition with the deposition rates and the Al to Ga ratio calibrated using RHEED intensity oscillations (4). The superlattice buffer provides a high quality barrier at the quantum well/superlattice interface. The superlattice GaAs wells are nominally 20 A thick for sample #2207 and 30 A thick for sample #2352. The 75 A AlGaAs section is an undoped spacer layer which separates mobile carriers within the 150 A GaAs well from ionized impurities in the 325 A doped AlGaAs layer. A single atomic plane of Si provides "delta" doping for the quantum well, and the 400 A GaAs layer at the top is used as a surface cap.

MODELING

The model used to analyze the VASE data is shown in Fig. 2a. The optical constants of bulk materials are normally used for the modeling procedure. However, in superlattices the energy subbands, along with the added complexity of wave function overlap, nullifies the use of bulk material properties (5). Because the optical constants of real superlattices are not independently known, the superlattice was modeled as a single $Al_xGa_{1-x}As$ layer of unknown thickness and composition. A native oxide layer was also incorporated into the model on top of the

GaAs cap.

RESULTS

In order to obtain the best possible fits to the experimental data, a number of modeling approaches were utilized. The results of the modeling sequence for both samples are shown in Table I. The initial best fit was over the entire (3500-8000 A) spectral range where the MSE was minimized for both ψ and Δ. The MSE was extremely high (> 500) in the first runs because of handedness changes in the polarization ellipse which are not detected in the data acquisition program. Once corrections for the handedness were incorporated into the experimental data (between 7450 and 8000 A for #2352, and between 7000 and 7450 A for #2207), the MSE values dropped to approximately 25 for both samples. Due to the shorter wavelength light being absorbed closer to the surface, the analysis range was decreased to 3500-6800 A in order to focus on the layers above the superlattice. Results from the 3500-6800 A analysis were used as input parameters for the ψ only data analysis over the full spectral range. This ensured that the fitting procedure would be more sensitive to the superlattice parameters.

The final model for sample #2352 with corresponding layer thicknesses, composition and MSE is shown in Fig. 2b. These values are from the ψ-only type of data fits shown in Table I. Although the confidence limits are

smaller when minimizing the MSE with respect to both ψ and Δ, the MSE was reduced by approximately three orders of magnitude by going with a ψ-only matching.

Plots of the experimental and calculated VASE data for sample #2352 are shown in Figs. 3a and 3b, and for sample #2207 in Figs 4a and 4b. These plots show the best fits obtained between the calculated data and the experimental data for the different regression analyses. The data are matched particularly well considering that there are seven variables with varying degrees of correlation between them. The good data fits are evidence that replacing the superlattice with an "effective" $Al_xGa_{1-x}As$ layer is a valid approach for this specific case, where the AlGaAs barriers are thick when compared to the GaAs quantum well thicknesses. The handedness changes are evidenced in the Δ plots by transitions passing through 180 and are not real structure.

The broad peaks in the ψ data at 5800, 6500, 7200 and 7900 A for #2352, and 6000, 6800 and 7500 A for #2207 are mainly the result of optical interference effects from the superlattice region. Spectral features at the shorter wavelengths are dominated by the top layer of GaAs. However, the spectral details at all wavelengths are influenced to some degree by each of the layers; in particular the surface oxide. This is shown by Figs. 5 through 8 which are discussed below.

Table I. Results of Experimental VASE Data Analysis (all thicknesses and wavelengths in A).

Sample: #2352

Fit Type	λ Range	t_1	t_2	t_3	x_3	t_4	t_5	x_5	MSE
ψ,Δ	3500-8000	33.2	418	405	0.37	141	5,529	0.36	24.9
ψ,Δ	3500-6800	26.3	429	415	0.35	157	5,417	0.34	5.71
ψ	3500-8000	25.9	437	405	0.37	141	5,464	0.32	.067
Nominal Values		25.0	400	400	0.30	150	5,500	0.30	****
90% Confidence Limits (+/-)		13.0	89	204	.068	104	259	.072	****

Sample: #2207

Fit Type	λ Range	t_1	t_2	t_3	x_3	t_4	t_5	x_5	MSE
ψ,Δ	3500-8000	15.4	329	239	0.34	151	5,134	0.22	21.1
ψ,Δ	3500-6800	25.1	276	303	0.32	139	5,089	0.17	1.37
ψ	3500-8000	24.7	286	275	0.35	153	5,115	0.21	.076
Nominal Values		25.0	300	400	0.30	150	5,520	0.30	****
90% Confidence Limits (+/-)		20.9	134	318	.135	240	489	.191	****

25.88 Å Oxide
437 Å GaAs
405 Å $Al_{0.37}Ga_{0.63}As$
141 Å GaAs
5115 Å $Al_{0.32}Ga_{0.68}As$
GaAs Substrate

Figure 2b. Final model for sample #2352.

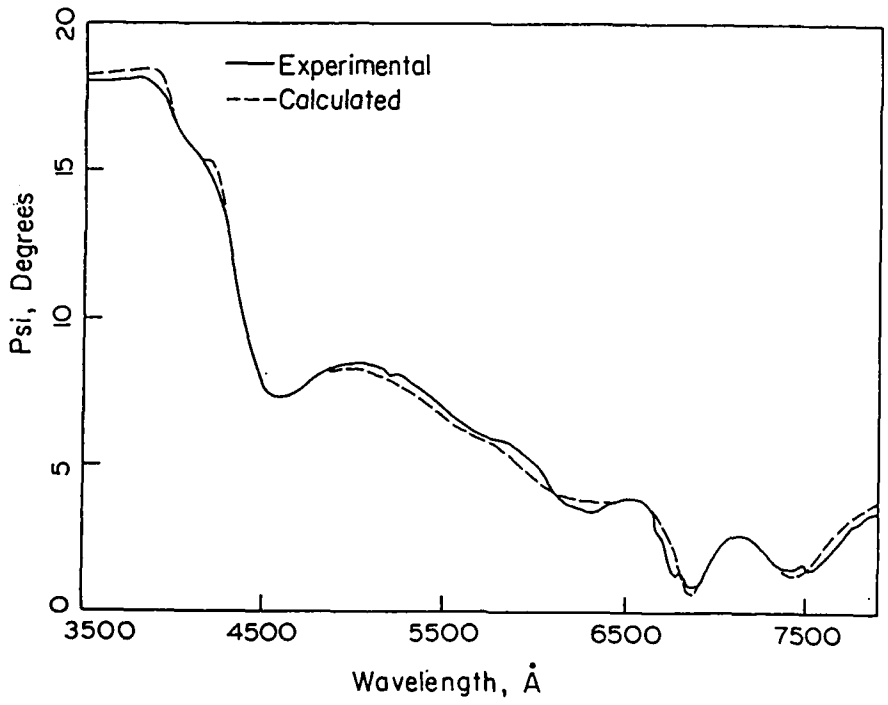

Figure 3a. Psi vs wavelength for sample #2352.

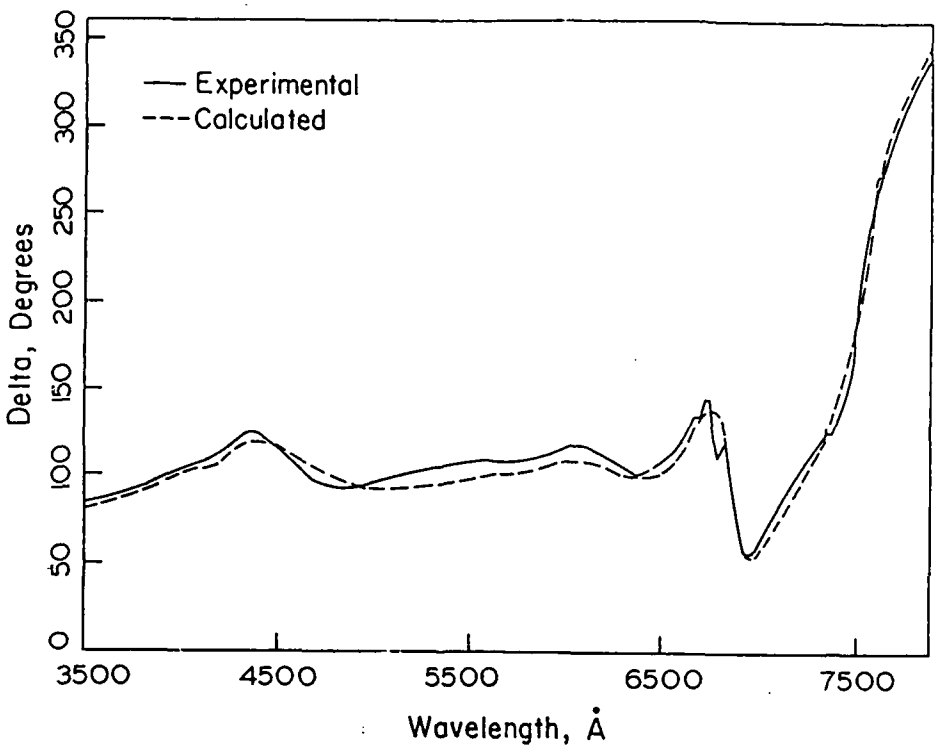

Figure 3b. Delta vs wavelength for sample #2352.

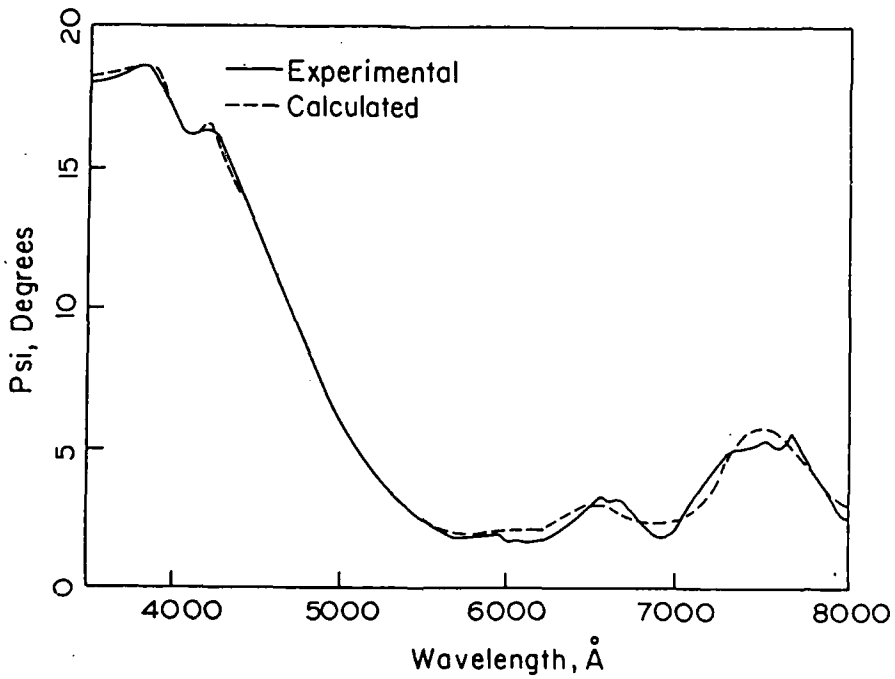

Figure 4a. Psi vs wavelength for sample #2207.

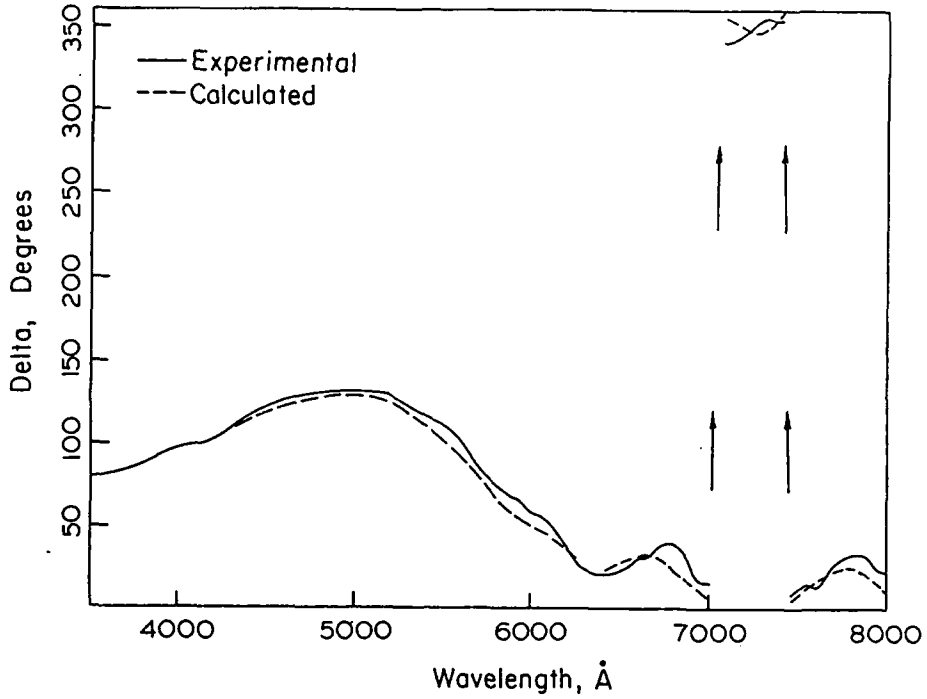

Figure 4b. Delta vs wavelength for sample #2207.

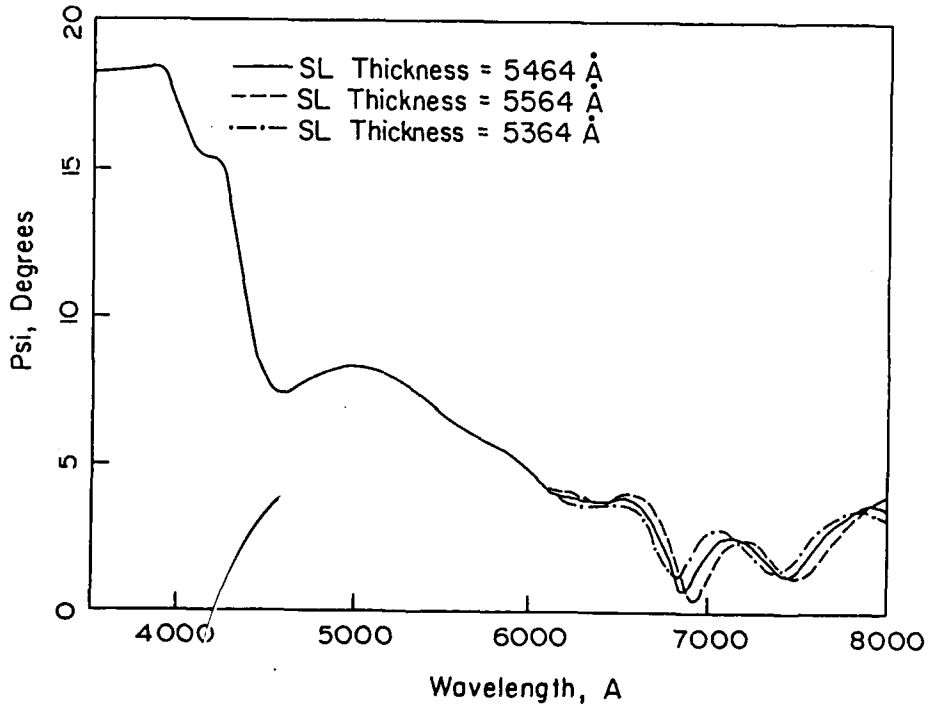

Figure 5. Generated psi vs wavelength for sample #2352 with varying superlattice thickness.

Figures 5 through 8 were made by fixing the thickness and composition values found from the analysis of sample #2352 and sequentially varying one parameter at a time for a single ϕ. Figs. 5 and 6 exhibit how the superlattice affects spectra in the 6000 to 8000 A range. It is apparent from Fig. 5. that increasing the superlattice thickness causes a corresponding increase in the amplitude and a shift to higher wavelengths of the ψ spectra. However, an increase in the value of superlattice composition is seen to cause an increase in amplitude and decrease in the wavelength shift (Fig. 6.). Variation of the thickness of the upper layer of GaAs has a pronounced effect on ψ between 4400 and 5200 A (Fig. 7.), and also causes reduction in the peak heights of maxima and minima at higher wavelengths. Changing the oxide thickness uniformly shifts the amplitude of ψ at all wavelengths below 7200 A (Fig. 8.).

The growth quality of the superlattice was determined by studying interfacial smoothness between layers. In order to evaluate roughness, a Bruggeman effective medium approximation was performed on sample #2352 with a 20 A mixture of GaAs and $Al_{0.3}Ga_{0.7}As$ in the model between the 150 A GaAs layer and the superlattice. The solution showed no appreciable change in values for layer thickness or composition. This resulted in an increase in the MSE of 0.3%, suggesting that physically there is not a mixture

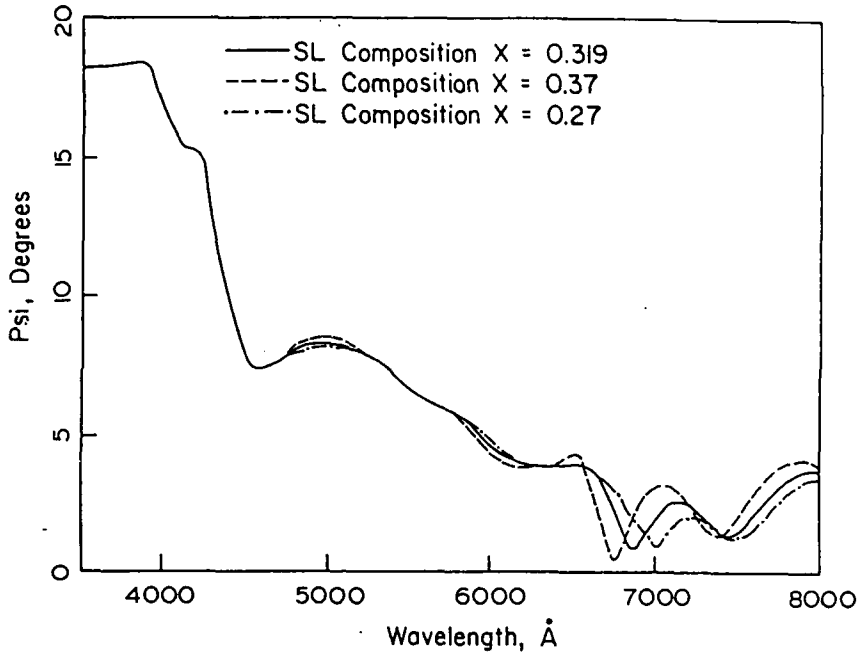

Figure 6. Generated psi vs wavelength for sample #2352

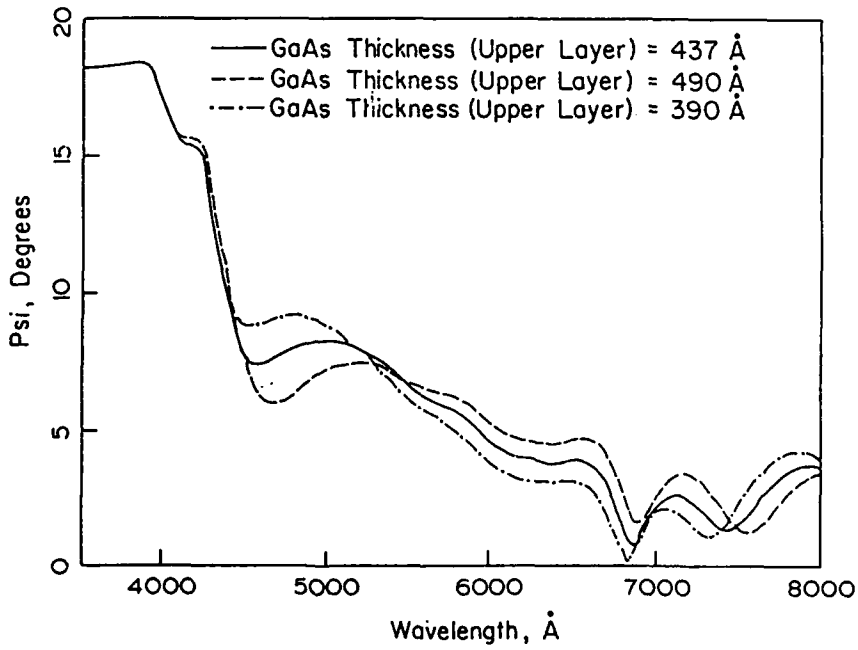

Figure 7. Generated psi vs wavelength for sample #2352 with varying thickness of upper GaAs layer.

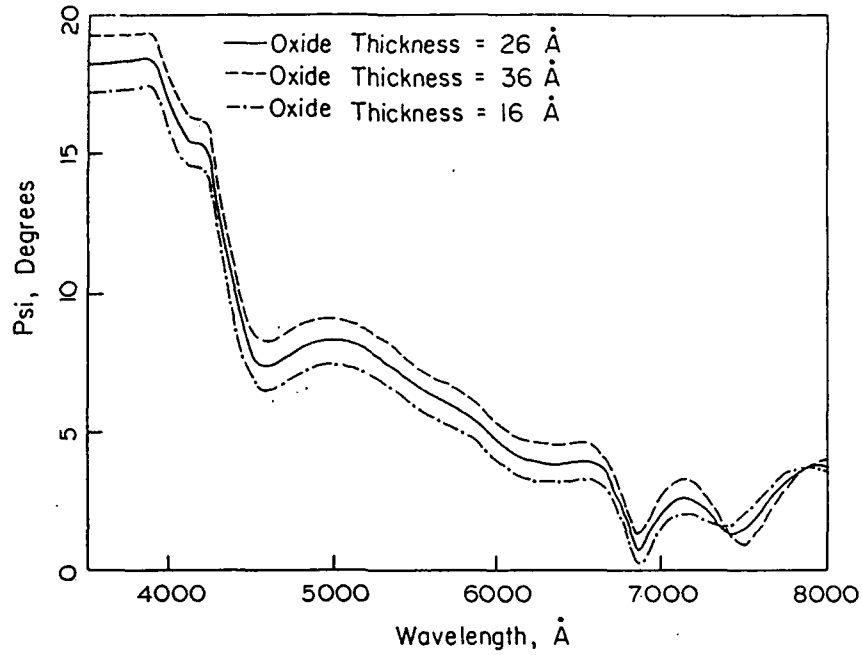

Figure 8. Generated psi vs wavelength for sample #2352 with varying surface oxide thickness.

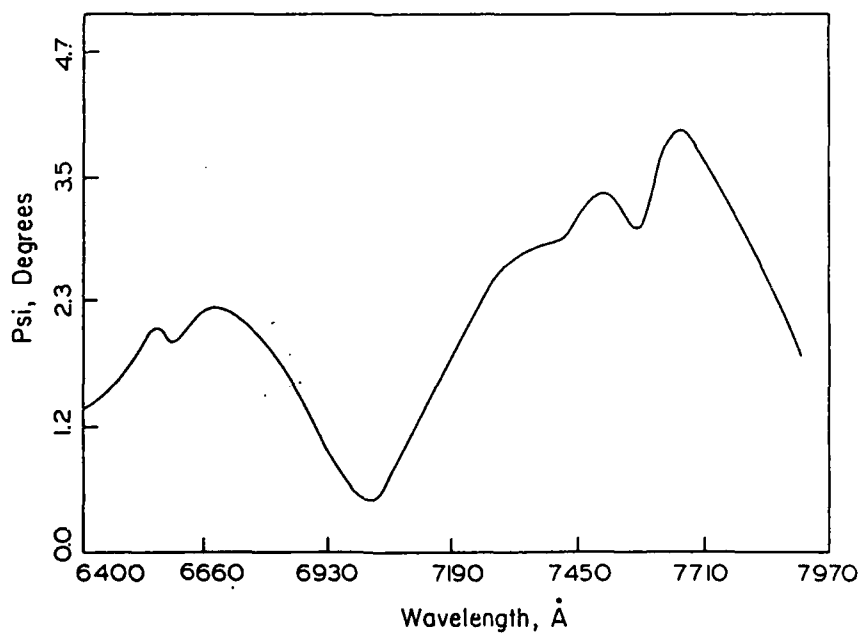

Figure 9. Excitonic spectra for sample #2207.

layer present. Another modeling trial incorporated an Al_2O_3 layer between the same layers. This analysis was done to determine if roughness existed due to the burial of oxygen impurities (which are Al composition dependent) in the GaAs portion of the GaAs/AlGaAs interface (6). The solution gave the same oxide layer thickness to within 2 A with no change in MSE. Thus the superlattice growth quality is considered to be uniform and interfacially abrupt since incorporation of a GaAs/AlGaAs mixture or oxide into the regression analysis worsened the fits.

The exciton peaks are shown in Fig. 9 for sample #2207 measured at 10 A intervals. The narrow excitonic structures seen at 6530 A,7500 A and 7700 A, are respectively the second electron to heavy hole, e-hh(2), first electron to light hole, e-lh(1), and first electron to heavy hole, e-hh(1), transitions in the superlattice quantum wells. The exciton energies are in qualitative agreement with values predicted by subtracting the exciton binding energy (9.1 meV in single 30 A GaAs quantum well) from the e-hh(1) transition energy of a quantum well with a 30 A well width and a wide $Al_{0.3}Ga_{0.7}As$ barrier (7,8). This analysis yields: $E_{e\text{-}hh(1)}$ = 1.582 eV (7,840 A) versus 7,700 A in Fig. 9. This approximation is reasonable since the barrier width is large in comparison to the well width. It follows that the e-lh (1) and e-hh(2) transitions are the next sharp structures that appear at higher

energies.

The presence of the excitonic structure in both samples suggests that the superlattice interfaces are of good quality. Non-planar and/or non-uniform layers would quench the exciton peaks due to "spreading" of the subband levels caused by variations in the well width. The broadness of the excitonic structure can most likely be attributed to slight energy changes in the quantum levels associated with slight layer thickness variations in the GaAs layers of the superlattice. The exciton lines from levels in the 150 A quantum well are outside of the spectral range shown.

In order to verify the accuracy of the VASE analysis, a complementary characterization technique, cross-sectional transmission electron microscopy (XTEM), was performed on sample #2352. XTEM produces a photographic display of the quality and thickness of semiconductor layers with a resolution limit of approximately 10 A. The XTEM photographs showed the layers in the sample to be abrupt and uniform with no viewable interfacial roughness. Particularly interesting is the fact that the XTEM pictures showed a superlattice of only 22 periods (with 220 A AlGaAs barriers and 20 A GaAs wells) as opposed to the 25 periods noted by the MBE growth facility.

Another VASE analysis (3000 to 8000 A wavelength range, ψ only fit) was done on sample #2352 using the XTEM

layer thickness values. The XTEM and VASE results are contained in Table II. The XTEM values compare closely to the VASE values obtained in the ψ only data fit (Table I), particularly in terms of the overall superlattice thickness (+/- 40 A). XTEM was unable to directly differentiate between the native oxide layer (t_1) and the GaAs cap layer (t_2). Therefore, the layer thicknesses for the oxide and cap layer are entered in Table II as a single value (460 A). The VASE analysis used the XTEM layer thicknesses as model input values. The alloy compositions of the AlGaAs and effective superlattice layers were variable since XTEM doesn't determine these parameters. The superlattice thickness was made variable in order to determine the accuracy of the solution for the two compositions. As evidenced in Table II, the 90% confidence limits on all three variables are improved when the XTEM values are held fixed. Also, the superlattice thickness and the two compositions are essentially constant with only a small increase in MSE (from 0.067 to 0.083). Thus, in going from a seven to a three variable solution, the accuracy of the VASE analysis is further verified.

CONCLUSION

Superlattices in MODFET/superlattice structures can be effectively incorporated in the VASE modeling sequence by representing the superlattice as a bulk AlGaAs layer of unknown alloy composition. Analysis of five layers and

two alloy fractions is possible if data are taken near the wavelength-dependent pseudo-Brewster angle. Room temperature excitonic effects are observed and growth quality determination is realized using the VASE measurement process. Thus the analysis of these structures through VASE can provide accurate and nondestructive assistance in the production of semiconductor structures for optoelectronic and microwave communication devices.

Table II. Comparison of XTEM and VASE Results for sample #2352 (all thicknesses are in A).

Analysis

Type	t_1	t_2	t_3	x_3	t_4	t_5	x_5	MSE
XTEM	460		420	***	160	5420	***	**
VASE:								
Model	26	434	420	0.37	160	5420	0.32	**
Result	***	***	***	0.36	***	5430	0.32	.083
90% lim.								
(+/-)	***	***	***	0.048	***	164	0.008	**

References

1. P. G. Snyder, B.N. De, K.G. Merkel, J.A. Woollam, D.W. Langer, C.E. Stutz, R.Jones, A.K. Rai and K. Evans,

To be published in Superlattices and Microstructures, August (1987).

2. S.A. Alterovitz, P.G. Snyder, K.G. Merkel, J.A. Woollam, D.C. Radulescu and L.F. Eastman, to be published in J. Appl. Physics, August 1987.

3. D.S. Chemla, Proc. of Basic Properties of Optical Materials , Edited by A. Feldman, NBS Publication **697**, 202, May (1985).

4. P.G. Snyder, M.C. Rost, G.H. Bu-Abbud, J.A. Woollam and S.A. Alterovitz, J. Appl. Physics **60** (9), 3293, (1986).

5. J.N. Schulman and Y.C. Chang, Physical Review B **31**, 2056, (1985).

6. T. Achtwhich, G. Burri, M.A. Py and M. Ileyems, Appl. Phys. Lett. **50**, 1730, (1987).

7. D.W. Langer, unpublished work performend at Wright Avionics Laboratory, WPAFB, Dayton, OH, February (1987).

8. R.L. Greene and K.K. Bajaj, Solid State Comm **45**, 831, (1983).

D. Interfacial Roughness Study

INTRODUCTION

The purpose of this VASE study was to determine the amount of interfacial roughness at an inverted interface where the GaAs layer is grown on top of an AlGaAs layer. The roughness problems inherent in GaAs/AlGaAs layered structures have been eluded to in the portion of this thesis concerning MBE growth.

The basis of the study was to show if a thicker AlGaAs layer increased the thickness of the interfacial roughness layer. The previous attempt at interfacial roughness determination, made during the superlattice characterization study, didn't indicate a roughness layer. The lack of roughness resolution in that study was potentially due to: 1) a low measurement sensitivity associated with the inverted interface being buried deep in the structure, and 2) the large amount of highly correlated variables in the regression analysis.

To overcome these previous difficulties, fairly simple structures were needed and fortunately obtainable from NASA Lewis. The sample NASA #1A had the following top to bottom nominal layer structure: 50 A GaAs cap layer/ 300 A $Al_{0.3}Ga_{0.7}As$/ 1 um GaAs buffer + GaAs substrate while NASA #2A had the identical structure except the AlGaAs thickness was 600 A. These two samples were thus seemingly ideal for our purpose since the inverted inter-

face was within 50 A of the surface, all layers were undoped (no Franz-Keldysh shifts with doping), and the number of measurement variables were low (one AlGaAs composition and four layer thicknesses including the roughness layer added during modeling).

EXPERIMENTAL

Before the actual VASE measurements were performed, it was important to determine if VASE could theoretically ascertain roughness on the order of a few monolayers (5 A - 20 A). It was felt that if VASE wasn't theoretically sensitive enough to measure interfacial roughness of this size, then empirical measurement wouldn't be justified. Therefore, 3-D generations using MAWEMA were performed. One of these was shown previously in Fig. 3 of this chapter (Preliminary Comments section). This plot of ψ versus Δ and λ was made using the nominal values of a sample obtained from NASA (NASA #1A). The sensitivity of at least +/- 2° in ψ for a 10 A roughness perturbation - although small - was considered substantial enough to measure with the VASE system.

Both samples were measured at 73.5 , 74.5 , and 76.5 at 20 A intervals from 3000 to 6000 A and 10 A intervals from 6010 to 8500 A. The 10 and 20 A wavelength increments were used to obtain the best data fits during analysis and to observe any fine spectral structure that might be present.

MODELING and RESULTS

The data fitting analysis was first performed with no interfacial roughness layer inserted in the model between the GaAs top layer and the AlGaAs layer. A disturbing aspect of the NASA #1A analysis was that the solution for the 50 A GaAs cap layer gave a near zero value (0.107 A) during a ψ only fit over the 3000-8500 A range with a corresponding 0.0288 MSE. In the next data fit for #1A, the GaAs layer thickness was removed from the model. The same MSE, AlGaAs composition, and other layer thicknesses were obtained. The experimental ψ and Δ data were then compared qualitatively with that of other samples containg GaAs layers. The spectrum of sample #1A failed to contain structure associated with the E_1 and $E_1+\Delta_1$ fundamental GaAs optical transitions. It was therefore concluded that NASA #1A had no GaAs cap layer. Another sample from the #1A wafer was obtained from NASA and remeasured to preclude the possibility of the thin 50 A GaAs layer having been etched off during surface cleaning prior to the initial VASE measurements. The GaAs layer again was analyzed as being nonexistent. At this point it was concluded that the GaAs layer had been omitted during MBE growth. The lack of the GaAs layer meant that an inverted interface didn't exist and that a comparative study between the two samples could not be performed.

Despite the lack of success with sample #1A, sample

#2A was still analyzed to ascertain if a roughness existed. Modeling of #2A was done with and without a roughness layer over a 3000 to 8000 A range (the 8000 - 8500 range was dropped since it was noisy and structurally uninteresting). A GaAs layer was found in #2A which gave a 31 A thickness in a ψ only modeling sequence . A 10 A variable thickness containing a 50%/50% mixture of GaAs and $Al_{0.3}Ga_{0.7}As$ was inserted as a Bruggeman EMA roughness layer. A zero value for the roughness layer was produced by the regression analysis.

CONCLUSIONS

From this experiment it can be concluded that the following are possible: 1) VASE isn't sensitive enough to measure sub-monolayer aggregate layer thicknesses, 2) surface effects (i.e Fermi level pinning) could dominate interfacial effects when the interface is quite close to the surface, or 3) there is no roughness layer present in the samples investigated.

END
DATE
FILMED
11-88
DTIC